

Advanced Techniques for High-Throughput Cellular Communications

Yingming (Allan) Tsai

Submitted in partial fulfillment of the
requirements for the degree
of Doctor of Philosophy
in the Graduate School of Arts and Sciences

COLUMBIA UNIVERSITY

2018

© 2018

Yingming (Allan) Tsai

All Rights Reserved

ABSTRACT

Advanced Techniques for High-Throughput Cellular Communications

Yingming (Allan) Tsai

The next generation wireless communication systems require ubiquitous high-throughput mobile connectivity under a range of challenging network settings (urban versus rural, high device density, mobility, etc). To improve the performance of the system, the physical layer design is of great importance. The previous research on improving the physical layer properties includes: a) highly directional transmissions that can enhance the throughput and spatial reuse; b) enhanced MIMO that can eliminate contention, enabling linear increase of capacity with number of antennas; c) mmWave technologies which operate on GHz bandwidth to offer substantially higher throughput; d) better cooperative spectrum sharing with cognitive radios; e) better multiple access method which can mitigate multiuser interference and allow more multi-users.

This dissertation addresses several techniques in the physical layer design of the next generation wireless communication systems. In chapter two, an orthogonal frequency division with code division multiple access (OFDM-CDMA) systems is proposed and a polyphase code is used to improve multiple access performance and make the OFDM signal satisfy the peak to average ratio (PAPR) constraint. Chapter three studies the I/Q imbalance for direct down converter. For wideband transmitter and receiver that use direct conversion for I/Q sampling, the I/Q imbalance becomes a critical issue. With higher I/Q imbalance, there will be higher degradation in quadra-

ture amplitude modulation, which degrades the throughput tremendously. Chapter four investigate a problem of spectrum sharing for cognitive wideband communication. An energy-efficient sub-Nyquist sampling algorithm is developed for optimal sampling and spectrum sensing. In chapter five, we study the channel estimation of millimeter wave full-dimensional MIMO communication. The problem is formulated as an atomic-norm minimization problem and algorithms are derived for the channel estimation in different situations.

In this thesis, mathematical optimization is applied as the main approach to analyze and solve the problems in the physical layer of wireless communication so that the high-throughput is achieved. The algorithms are derived along with the theoretical analysis, which are validated with numerical results.

Table of Contents

List of Figures	v
List of Tables	viii
1 Introduction	1
1.1 High Throughput for Wireless Systems	1
1.2 Research Motivation and Objectives	2
1.3 Thesis Contributions	4
1.3.1 Uplink Orthogonal Multiple Access	4
1.3.2 I/Q Imbalance	4
1.3.3 Wideband Spectrum Sensing	5
1.3.4 Millimeter Wave Full-dimensional MIMO Channel Estimation	6
1.4 Thesis Organization	6
2 Polyphase Codes for Uplink OFDM-CDMA Systems	9
2.1 Introduction	9
2.2 System Descriptions	12
2.2.1 Polyphase Sequences	12
2.2.2 OFDM-CDMA System Using Polyphase Codes	15
2.3 Performance Analysis	20
2.3.1 PAPR Analysis	20
2.3.2 MAI Analysis	22

2.4	Simulation results	26
2.4.1	PAPR Performance	26
2.4.2	Uncoded BER Performance	28
2.5	Conclusions	32
2.5.1	Medium to high spreading factor case: $2^{\lceil n/2 \rceil} \leq 2^m \leq 2^n$	33
2.5.2	Low spreading factor case: $1 < 2^m < 2^{\lceil n/2 \rceil}$	35
3	Blind Frequency-dependent I/Q Imbalance Compensation for Direct-conversion Receivers	37
3.1	Introduction	37
3.2	System Descriptions	39
3.2.1	I/Q Imbalance Signal Model	39
3.2.2	Second-order Signal Statistics	42
3.3	Time-domain I/Q Imbalance Compensation	43
3.3.1	Identifiability	43
3.3.2	Blind I/Q Imbalance Compensation Algorithm	46
3.4	I/Q Imbalance Compensation for OFDM Systems	49
3.5	Simulation Results	51
3.5.1	Simulation Setup	51
3.5.2	Performance of Time-domain Blind Compensation Algorithm .	52
3.5.3	Performance of Frequency-domain Blind Compensation Algorithm	55
3.6	Conclusions	58
4	Wideband Spectrum Sensing Based on Sub-Nyquist Sampling	63
4.1	Introduction	63
4.2	Signal Model and Problem Statement	66
4.3	Power Spectrum Estimation under Multicoset Sampling	69
4.3.1	Multicoset Sampling	69

4.3.2	Power Spectrum Estimation	72
4.3.3	A Lower Bound on the Number of Cosets	76
4.3.4	Digital Implementation	78
4.4	Spectral Detection	81
4.4.1	Analysis of Spectrum Estimation Error	81
4.4.2	A Simple Error Covariance Estimator	82
4.4.3	Constant-False-Alarm Frequency-bin Energy Detector	84
4.5	Simulation Results	85
4.5.1	Simulation Setup	85
4.5.2	Multiband Spectrum Sensing Performance	86
4.6	Conclusions	91
5	Beamformed Millimeter-Wave Full-dimensional MIMO Channel Es- timation Based on Atomic Norm Minimization	98
5.1	Introduction	98
5.2	System Descriptions and Background	101
5.2.1	System and Channel Models	101
5.2.2	Existing mmWave Channel Estimation Methods	103
5.3	Channel Estimation via Atomic Norm Minimization	105
5.3.1	Background on Multi-dimensional Atomic Norm	105
5.3.2	Atomic Norm Minimization Formulation	107
5.4	Efficient Algorithm for Channel Estimation under UPA	109
5.4.1	A Formulation Based on 2D MMV Atomic Norm	109
5.4.2	An Approximation to 4D Atomic Norm Minimization	110
5.4.3	ADMM for Approximate 4D Atomic Norm Minimization	114
5.5	The General Planar Array Case	116
5.6	Simulation Results	120
5.6.1	Simulation Setup	120
5.6.2	Performance Evaluation	121

5.7	Conclusions	129
.0.1	Derivation for (5.71) and (5.72)	129
.0.2	Derivation for (5.73)	130
Bibliography		131

List of Figures

2.1	Proposed OFDM-CDMA system diagram.	18
2.2	Polyphase sequence code tree for $N=16$	21
2.3	PAPR of OFDM-CDMA systems using polyphase codes and Hadamard codes with (a) SF=8 and 16, $N=256$ subcarriers (b) SF=16 and 32, $N=1024$ subcarriers.	27
2.4	BER performance of OFDM-CDMA system using polyphase codes and Hadamard codes with $N = 256$ subcarriers and SF=32, 64.	30
2.5	BER performance of OFDM-CDMA system using polyphase and Hadamard codes with SF=16, $N = 1024$ subcarriers (for Hadamard codes with 3 dB clipping and without clipping).	32
3.1	(a) The direct-conversion receiver with I/Q imbalance compensation. (b) The effective model of a direct-conversion receiver with I/Q imbalance.	40
3.2	Convergence of the proposed time-domain blind I/Q imbalance compensation method. (a) Case 1 . (b) Case 2	53
3.3	The IRR and SER performance of the proposed time-domain blind I/Q imbalance compensation method for Case 1 . (a) IRR performance. (b) SER performance.	56
3.4	The IRR and SER performance of the proposed time-domain blind I/Q imbalance compensation method for Case 2 . (a) IRR performance. (b) SER performance.	57

3.5	The SER performance of the proposed frequency-domain blind I/Q imbalance compensation method for OFDM systems for Case 1	58
3.6	The SER performance of the proposed frequency-domain blind I/Q imbalance compensation method for OFDM systems for Case 2	59
4.1	(a) Multiband signals with different central carrier frequencies. (b) The vector $\mathbf{X}(f)$ is constructed by dividing \mathcal{F} into $L = 4$ (down-sampling factor) intervals. (c) The folded spectrum $\mathbf{Y}(f)$	68
4.2	The diagram of the proposed multiband spectrum sensing method based on multicoset sampling.	73
4.3	(a) The power spectrum for experiment 1 with five subbands. (b) The power spectrum for experiment 2 with eight subbands. (c) The power spectrum for experiment 3 with six subbands.	87
4.4	(a) The estimated power spectrum for experiment 1. $L = 20, P = 12$. (b) The detection results for the frequency bins using the constant-false alarm detector. (c) The subbands obtained after applying the refinement step on the detection results of (b).	88
4.5	The probability of false alarm performance of the frequency bin detector for experiments 1, 2 and 3.	89
4.6	The multiband spectrum sensing performance as a function of SNR. Sensing times $\tau = 160$ and $\tau = 80 \mu s$ are considered. (a) experiment 1: $L=20, P=12$. (b) experiment 2: $L=12, P=7$. (c) experiment 3: $L=15, P=8$	92
4.7	The multiband spectrum sensing performance for experiment 2 with different $P = 8, 12, 16, 20, 24$ cosets which are corresponding to the compression ratio from 6.25, 4.167, 3.125, 2.5, 2.08, when $L = 50$, $\tau = 160 \mu s$	93
4.8	The multiband spectrum sensing performance for experiment 3 with different sampling patterns with $L = 15$ and $L = 25$, $\tau = 160 \mu s$. . .	94

5.1	The approximation errors $ \ \mathbf{H}\ _{\mathcal{A}_M} - \text{SDP}(\mathbf{H}) $ and $ \ \mathbf{H}\ _{\mathcal{A}_M} - \ \mathbf{H}\ _{\mathcal{A}_{\text{MMV}}} $ when the separations satisfy $\Delta_{\min, f_i} \geq \delta(M_i - 1)$, $\Delta_{\min, g_i} \geq \delta/(N_i - 1)$, $N_i = M_i = 16$, for $i = 1, 2$. The simulations are run 100 times for each δ .	113
5.2	Convergence of proposed ADMM channel estimator with different SNR	
	(a) SNR= 4dB.	122
5.3	Convergence of proposed ADMM channel estimator with different SNR	
	(b) SNR= 10dB.	123
5.10	UPA NMSE	128
5.11	UPA NMSE	128

List of Tables

2.1	SIMULATION PARAMETERS	36
-----	---------------------------------	----

Acknowledgments

First and foremost, I would like to gratefully thank my research supervisor, Professor Xiaodong Wang for giving me the opportunity of pursuing my doctoral program under his supervision at Columbia University, for his inspiration, consistent guidance, and generous support throughout my doctoral studies. I have learned greatly from his remarkable knowledge and research enthusiasm. He has also helped me in critically reviewing this thesis and vastly enriching it with his very helpful comments.

I am grateful to my thesis committee members and examiners: Professor Javad Ghaderi (EE Department, Columbia University), Professor John Paisley (EE Department, Columbia University), Dr. Chong Li (Qualcomm Research and Development and adjunct assistant professor at Columbia University), and Dr. Gordon Zhang (Principal Engineer, InterDigital communication. inc), for their time of reading and reviewing my Ph.D. work, for their very valuable and constructive comments for the thesis.

I am grateful for the time spent with my friend Dr. Le Zheng at Columbia University, Dr. Chia-Pang Yen and Dr. Gordon Zhang for supporting my PhD thesis developing. Lastly, I want to thank my mom and dad, my wife Kate and my son William, for their constant love, encouragement and support in all my pursuits. Without their support and encouragement, the accomplishment of this thesis would not have been possible.

To my parents, my wife Kate and my son William who have constantly loved and supported me.

Chapter 1

Introduction

1.1 High Throughput for Wireless Systems

In recent years, the demand of high-speed data service of mobile users increases exponentially. However, the spectrum for cellular networks is limited, so the licensed frequency bands become scarce and expensive. In practice, the bands are limited within spectrum typically from several hundred megahertz (MHz) to few gigahertz (GHz) [Dahlman *et al.*, 2011]. Hence, advanced technologies and mobile communication systems have to be developed. The next generation wireless communication systems investigate to improve the physical layer (PHY) transmission mechanisms to increase bit rate and reduce interference. These approaches include: new multiple access scheme, multi-user interference mitigation, enhanced wide-band transceiver, spectrum sensing with sharing, new high-bandwidth and full-dimensional MIMO technologies. In this paper, we study the multiple access, enhanced, spectrum sensing, mmWave full-dimensional MIMO to achieve the high throughput in wireless communication.

1.2 Research Motivation and Objectives

The existing LTE/LTE-A systems can provide a data rate of 100 Mbps in downlink and 50Mbps in uplink [Thr, 2008], [Dahlman *et al.*, 2011]. However, the modulation scheme in LTE/LTE-A has high PAPR, which causes signal distortion in communication. To solve such problem, we propose an OFDM-CDMA system that employs polyphase codes to support variable spreading factors with constant envelope. In addition, we propose to use polyphase sequences as an orthogonal multiple access scheme for improving uplink multiple access scheme.

Another problem for the exiting communication systems is the I-Q channel imbalance. In the analog domain of a direct down-conversion system, a demodulated complex signal inherently includes amplitude-phase imbalance between In-phase (I) and Quadrature-phase (Q) signal paths. This imbalance exists because these signals are not perfectly matched to each other. The I/Q amplitude and phase imbalance produces a sideband image that severely degrades the error vector magnitude (EVM) of the received signal. The higher the IQ imbalanced, the higher the distortion will be in the QAM constellation. For frequency selective I/Q imbalance, i.e., band-dependent I/Q imbalance increases the difficulty of I/Q compensation. These facts motivate us to study frequency selective I/Q imbalance compensation methods.

Radio frequency (RF) spectrum is a valuable but tightly regulated resource due to its unique and important role in wireless communications. With the growing of wireless services, the demands for the RF spectrum increases as well, leading to scarce spectrum resources. Moreover, it has been reported that the localized temporal and geographic spectrum utilization is extremely low. The current spectrum policy allocating a fixed-frequency band to individual wireless services, is known to be inefficient. Recently, the Federal Communications Commission (FCC) is developing new spectrum policies, which allow secondary users to access a licensed band when the primary user is absent. Many narrowband spectrum sensing algorithms have been studied in the literature, including matched filtering, energy detection, and cyclo-

CHAPTER 1. INTRODUCTION

stationary feature detection [Yucek and Arslan, 2009]. While present narrowband spectrum sensing algorithms have focused on exploiting spectral opportunities over narrow frequency range, cognitive radio networks will eventually be required to exploit spectral opportunities over a wide frequency range from hundreds of megahertz to several gigahertz for higher throughput. Driven by Shannon's famous formula that, under certain conditions, the maximum theoretically achievable bit rate is proportional to the spectral bandwidth. Hence, different from narrowband spectrum sensing, wideband spectrum sensing aims to find more spectral opportunities over a wide frequency range and achieve higher opportunistic aggregate throughput in cognitive radio networks. However, conventional wideband spectrum sensing techniques based on standard analog-to-digital converters (ADCs) could lead to unaffordably high sampling rate or implementation complexity. Hence, revolutionary wideband spectrum sensing techniques become increasingly important. In addition, sampling in wide spectrum is challenging because it consumes more power. In this thesis, we study the spectrum sensing with sub-Nyquist sampling such that the user terminals can efficiently sense ultra wideband spectrum and consumes less power.

Although mmWave technology has been known for many decades [Rappaport *et al.*, 2014], the mmWave systems have mainly been deployed for military applications. With the development of signal processing, mmWave technology has gained great interest. We study the mmWave full-dimensional MIMO system. With the support from large number of antennas, massive MIMO is showing an increasing spectral efficiency. In 3GPP [Thr, 2008], a full-dimensional MIMO (FD-MIMO) technology has been introduced for massive MIMO in cellular system. An FD-MIMO system can also deliver a large improvement to the high-order multi-user MIMO (MU-MIMO) [Jindal, 2006]. Compared to the existing LTE systems, it improves the capacity by 2-4 times according to the simulation. FD-MIMO is considered as one of the key 5G mmWave MIMO technologies and provides better SNR and system dimension by making use of active antenna array and three-dimensional channels.

This thesis aims to develop new physical layer techniques to achieve high throughputs in wireless communications. We explore new signal processing techniques in these systems and channel models. We also provide theoretical results of the sufficient conditions of successful estimation. We also study various methods to improve the efficiency of the algorithms. The performance of the results are verified by the numerical results.

1.3 Thesis Contributions

The technical contributions of the thesis are summarized as follows.

1.3.1 Uplink Orthogonal Multiple Access

We propose a OFDM-CDMA system that employs polyphase codes to support variable spreading factors. A systematic approach for constructing the polyphase code sequences of variable spreading factors is developed. Polyphase codes exhibit better auto- and cross-correlation properties than Hadamard codes. When employed in OFDM-CDMA systems, polyphase codes result in certain structured multiple-access interference (MAI) caused by multipath. Analytical and numerical results show that OFDM-CDMA systems employing polyphase codes have better PAPR performance than those using Hadamard codes. The BER performance of the OFDM-CDMA system using polyphase codes is evaluated by numerical results and compared to that of the OFDM-CDMA system using Hadamard codes with and without clipping.

1.3.2 I/Q Imbalance

Frequency-dependent I/Q imbalance is one of the major impairments in the direct-conversion receivers (DCR) for high-speed wideband wireless systems. We propose two new blind methods for compensating frequency-dependent I/Q imbalance. The first one is a time-domain approach. Specifically we develop a blind identifiability

condition based on which a cost function and a gradient descent search algorithm are proposed for blind I/Q imbalance compensation. The second blind method is a frequency-domain approach for OFDM systems. Here we provide blind estimators for the frequency-selective I/Q imbalance parameters, which once obtained, the I/Q imbalance can then be compensated by a simple single-tap matrix filter inversion. We provide extensive simulation results to demonstrate the performance of the proposed algorithms.

1.3.3 Wideband Spectrum Sensing

In this topic, we consider the problem of locating multiple active spectrum subbands in a wide range of frequency bands. A major challenge associated with such wideband spectrum sensing is that it is either infeasible or too expensive to perform Nyquist sampling on the wideband signal. In this chapter, we propose a sensing scheme based on a sub-Nyquist sampling method called multicoset sampling, which is similar to the polyphase implementation of the Nyquist sampling, but requires less A/D converters. In contrast to the traditional sub-Nyquist approaches where the wideband signal is first reconstructed from the sub-Nyquist samples, we develop a method that directly estimates the power spectrum of the wideband signal of interest using the sub-Nyquist samples, by exploiting its statistical properties. We also characterize the statistical distribution of the proposed power spectrum estimator, based on which we obtain a constant-false-alarm energy detector for the frequency bins. Simulation results are provided to demonstrate the effectiveness of the proposed multiband spectrum sensing method based on sub-Nyquist sampling.

1.3.4 Millimeter Wave Full-dimensional MIMO Channel Estimation

The millimeter-wave (mmWave) full-dimensional (FD) MIMO system employs planar arrays at both the base station and user equipment and can simultaneously support both azimuth and elevation beamforming. In this chapter, we propose atomic-norm-based methods for mmWave FD-MIMO channel estimation under both uniform planar arrays (UPA) and non-uniform planar arrays (NUPA). Unlike existing algorithms such as compressive sensing (CS) or subspace methods, the atomic-norm-based algorithms do not require to discretize the angle spaces of the angle of arrival (AoA) and angle of departure (AoD) into grids, thus provide much better accuracy in estimation. In the UPA case, to reduce the computational complexity, the original large-scale 4D atomic norm minimization problem is approximately reformulated as a semi-definite program (SDP) containing two decoupled two-level Toeplitz matrices. The SDP is then solved via the alternating direction method of multipliers (ADMM) where each iteration involves only closed-form computations. In the NUPA case, the atomic-norm-based formulation for channel estimation becomes nonconvex and a gradient-decent-based algorithm is proposed to solve the problem. Simulation results show that the proposed algorithms achieve better performance than the CS-based and subspace-based algorithms.

1.4 Thesis Organization

The rest of the thesis is organized as follows.

Chapter 2 propose to use polyphase codes for uplink OFDM-CDMA systems to address the peak-to-average power ratio (PAPR) problem. Analytical and numerical results show that OFDM-CDMA systems employing the proposed polyphase codes have remarkably better PAPR performance than that using Hadamard codes. BER performance of OFDM-CDMA systems employing polyphase codes is close to that of

CHAPTER 1. INTRODUCTION

system using Hadamard codes without clipping. The low PAPR property with better BER performance makes the proposed OFDM-CDMA systems using the polyphase codes a promising solution to uplink multicarrier and multiple access systems.

Chapter 3 studies the problem of I/Q imbalance. In this chapter, We have proposed two blind approaches to compensate the frequency-dependent I/Q imbalance for wideband direct-conversion receivers. One is a time-domain method for general systems and the other is a frequency-domain method that is specifically designed for OFDM systems. For the time-domain method, a blind identifiability condition is given based on which a cost function for compensating the I/Q imbalance is proposed; and a gradient-descent algorithm is derived to obtain the compensating filter. For the frequency-domain method, we have developed estimators for the frequency-dependent I/Q imbalance parameters based on the second-order statistics of the received signal; the compensation filter can then be obtained in closed-form given these estimated parameters.

Chapter 4 is concerned with the problem of multiband spectrum sensing. We have proposed a new technique for multiband spectrum sensing using sub-Nyquist sampling. The basic procedure of the proposed method involves multicorset sampling of the signal, followed by power spectrum estimation and energy detection on the frequency bins. The only prior knowledge needed is an upper bound on the number of active subbands in the frequency range of interest. And the proposed multiband sensing algorithm outputs the number of active subbands and the location of each active subband. The key ingredients of the proposed wideband sensing algorithm, including a power spectrum estimator based on multicorset sampling, and a constant-false-alarm frequency-bin energy detector, are developed theoretically; and their effectiveness is demonstrated by simulations.

Chapter 5 studies the problem of atomic-norm-based channel estimation for millimeter wave full-dimensional MIMO systems. In this chapter, a new approach based on atomic-norm minimization problem for the channel matrix estimation problem for

CHAPTER 1. INTRODUCTION

mmWave full-dimensional MIMO systems is proposed. The system model includes a base station (BS) equipped with a very large number of antennas communicating simultaneously with a large number of autonomous single-antenna user terminals (UT)s, over a realistic physical channel with finite scattering model. Based on the idea that the degrees of freedom of the channel matrix are smaller than its large number of free parameters, a low-rank matrix approximation based on CS is proposed and solved via a SDP. Our analysis and experimental results suggest that the proposed method outperforms the existing ones in terms of estimation error performance without requiring any knowledge about the statistical distribution or physical parameters of the propagation channel.

Chapter 2

Polyphase Codes for Uplink OFDM-CDMA Systems

2.1 Introduction

Future wireless communication networks need to provide broadband services such as wireless Internet access to subscribers. Such broadband services require reliable and high-rate communications over time- and frequency-dispersive channels with limited spectrum and intersymbol interference (ISI) caused by multipath fading. The direct-sequence code-division multiple-access (DS-CDMA) technique is adopted by the third-generation (3G) wireless communication systems due to its advantages over conventional time-division multiple-access (TDMA) and frequency-division multiple-access (FDMA) systems. However, its capacity is limited by multiple-access interference (MAI). On the other hand, orthogonal frequency-division multiplexing (OFDM) is one of the most promising solutions to the next-generation wireless systems. OFDM has high spectral efficiency and adaptive coding and modulation can be employed across subcarriers. With cyclic prefix (CP), OFDM offers excellent robustness to time-dispersion (multipath fading). Implementation is simplified because the base-band modulator and demodulator involve simply IFFT/FFT. Simple receiver struc-

ture (since only one tap equalizer is required) is another advantage of OFDM systems. OFDM has been chosen for European digital audio and video broadcasting, WLAN standards (802.11), WiMax (802.16), and is being considered for the long term evolution of 3GPP.

Recently, there has been significant interest in combining CDMA and OFDM [Hara and Prasad, 1997], [Yee *et al.*, 1993], such as MC-CDMA and MC-DS-CDMA. These systems keep the advantages of both CDMA and OFDM systems. Despite all the attractive advantages, OFDM and OFDM-CDMA as well as multi-carrier systems in general have their disadvantages. One major disadvantage of the multi-carrier system in the uplink is its inherent high peak-to-average power ratio (PAPR). The PAPR of multi-carrier signals increases as the number of subcarriers increases. When high PAPR signals are transmitted through the nonlinear power amplifier, severe signal distortion will occur. Clipping will cause inter-subcarrier modulation, out-of-band radiation and performance degradation. Therefore, highly linear power amplifier with power backoff is required for multi-carrier systems. This results in the low power efficiency and shortened battery life of the mobile device. Techniques for reducing PAPR in OFDM systems have been studied extensively [Han and Lee, 2005], [Tarokh and Jafarkhani, 2000], including non-linear block coding, partial transmission sequences, selective mapping, tone injection, clipping, filtering, etc. The effectiveness of these methods varies and each has its own inherent trade-off in terms of complexity, performance and spectral efficiency.

It is desirable to keep the advantages of CDMA and OFDM, and in the meanwhile to mitigate the PAPR problem. In this paper, we propose to use polyphase codes for OFDM-CDMA systems to address this issue. Although polyphase codes have been considered for multi-carrier CDMA (MC-CDMA) systems in a few works, [Popović, 1998], [Tan and Stüber, 2005], none of these works can support variable spreading factors. Our contribution is that we extend the works in [Popović, 1998], [Tan and Stüber, 2005] by proposing a method enabling polyphase codes to support variable

spreading factors in OFDM-CDMA systems. A systematic approach for constructing the polyphase code sequences of variable spreading factors for OFDM-CDMA system is developed. The resulting polyphase code set can support large number of users and variable spreading factors just like Hadamard codes, which are usually used in conventional OFDM-CDMA systems. The resulting polyphase code sequences not only have better auto- and cross-correlation properties in both time- and frequency-domains than Hadamard codes, but also have constant envelopes (for medium and large spreading factors) or low PAPR's (for small spreading factors) which is preferred for uplink/reverse link transmission. Another interesting property of the OFDM-CDMA systems employing the polyphase codes is that the MAI between any two codes can be avoided if their cyclic shift distance is larger than their maximum multipath channel delay spread. Performance of the proposed systems is analyzed and compared with OFDM-CDMA systems using Hadamard codes. Numerical results show that OFDM-CDMA systems using proposed polyphase codes have better PAPR performance than those using Hadamard codes. With a receiver of the same complexity, OFDM-CDMA systems using polyphase codes can achieve bit error rate (BER) performance no worse than those using Hadamard codes without clipping, and better than those with clipping.

The remainder of the chapter is organized as follows. The system descriptions are given in Section 2.2. Analyses of the PAPR property and the MAI structure of the OFDM-CDMA system using polyphase codes are performed in Section 2.2.2. Section 2.4 presents the numerical results for PAPR and uncoded BER performance. Section 2.5 concludes the paper.

2.2 System Descriptions

2.2.1 Polyphase Sequences

Polyphase sequence has been found to have some important properties: such as periodic orthogonality and the constant amplitude zero auto-correlation (CAZAC) property [Chu, 1972], [Frank and Zadoff, 1962]. Polyphase sequence has been proposed to be employed as spreading codes with a fixed spreading factor in OFDM-CDMA systems [Popović, 1998], [Tan and Stüber, 2005]. However, in previous works polyphase sequence cannot support variable spreading factors in OFDM-CDMA systems, which made it not suitable for practical systems. To address this issue, we propose a new scheme to construct variable spreading factors polyphase codes and replace the Hadamard codes that are usually used in conventional OFDM-CDMA systems. Suppose that the maximum spreading factor that the polyphase codes support in the system is $N = 2^n$.

A typical polyphase sequence, Zadoff-Chu sequence [Chu, 1972], is used in the paper. The Zadoff-Chu polyphase sequence with length N , is given by [Chu, 1972]

$$g_N[k] = e^{-j\frac{\pi k^2}{N}}, \quad k = 0, \dots, N-1. \quad (2.1)$$

We call the polyphase sequence given in (2.1) as the primitive polyphase sequence. In order to use polyphase sequence for the purpose of multiple access, more orthogonal polyphase sequences need to be created. This can be achieved by shifting the primitive polyphase sequence in phase. The ℓ th phase-shifted version of the generic orthogonal polyphase sequence, $\mathbf{g}_N^\ell = \{g_N^\ell[k]; k = 0, \dots, N-1\}$, is given by

$$g_N^\ell[k] = e^{-j\frac{\pi k^2}{N}} \cdot e^{-j\frac{2\pi k\ell}{N}} = e^{-j\frac{\pi(k^2+2k\ell)}{N}}, \quad \ell = 0, \dots, N-1. \quad (2.2)$$

The polyphase sequence in (2.2) is a special case of generalized chirp like (GCL) sequence [Popović, 1992]. When $N = 2^{2m}$, the GCL sequences have minimum alphabet size of \sqrt{N} [Popović, 1994b]. For example, for GCL sequence with length $N = 256$,

the alphabet size is 16. That is, phase-shifted GCL sequences with length 256 can be constructed using 16-PSK symbols. An alternative way is to use Frank sequence [Frank and Zadoff, 1962], which is a special case of GCL sequence with minimum alphabet size. In general, using Frank sequence or GCL sequence with minimum alphabet size results in reduced implementation complexity [Popović, 1994a].

The polyphase sequence has the following properties:

2.2.1.1 Periodic cross-correlation

Consider two phase-shifted polyphase sequences $\mathbf{g}_N^{\ell_p}$ and $\mathbf{g}_N^{\ell_q}$. Without loss of generality, we assume that $\ell_p \geq \ell_q$. Their periodic cross-correlation function $R_{g_N^{\ell_p}, g_N^{\ell_q}}[\tau]$ (as defined in [Sarate, 1979]) can be expressed as

$$\begin{aligned}
 R_{g_N^{\ell_p}, g_N^{\ell_q}}[\tau] &= \frac{1}{N} \sum_{k=0}^{N-1} g_N^{\ell_p}[k] (g_N^{\ell_q}[(\tau + k)_N])^* \\
 &= \frac{1}{N} \sum_{k=0}^{N-\tau-1} g_N^{\ell_p}[k] (g_N^{\ell_q}[k + \tau])^* + \frac{1}{N} \sum_{k=N-\tau}^{N-1} g_N^{\ell_p}[k] (g_N^{\ell_q}[k + \tau - N])^* \\
 &= \frac{1}{N} \sum_{k=0}^{N-1} e^{-j \frac{\pi(k^2 + 2k\ell_p)}{N}} e^{j \frac{\pi((k+\tau)^2 + 2(k+\tau)\ell_q)}{N}} \\
 &= \frac{1}{N} e^{j \frac{\pi(\tau^2 + 2\tau\ell_q)}{N}} \sum_{k=0}^{N-1} e^{j \frac{2\pi k(\tau + \ell_q - \ell_p)}{N}} = e^{j \frac{\pi(\tau^2 + 2\tau\ell_q)}{N}} \delta[\tau + \ell_q - \ell_p], \quad (2.3)
 \end{aligned}$$

where $\delta[\cdot]$ is the Kronecker delta function. It is obvious that the absolute value of periodic cross-correlation in (2.3) equals to 1 only when $\tau = \ell_p - \ell_q$. Hence, the phase-shifted polyphase sequences $\mathbf{g}_N^{\ell_p}$ and $\mathbf{g}_N^{\ell_q}$ have periodic zero cross-correlation property within a zone and the length of the zero cross-correlation zone (ZCZ) equals to their phase shift difference (i.e., $ZCZ = \ell_p - \ell_q$). This property is called Z-orthogonal property. Two sequences $\mathbf{g}_N^{\ell_p}$ and $\mathbf{g}_N^{\ell_q}$ are Z-orthogonal if their cross-correlation satisfies

the following conditions [H. Torii and Suehiro, 2004], [Welch, 1974]

$$R_{g_N^{\ell_p}, g_N^{\ell_q}}[\tau] = \begin{cases} 1, & \tau = 0, \ell_p = \ell_q \\ 0, & 0 \leq |\tau| < ZCZ, \ell_p \neq \ell_q \end{cases}. \quad (2.4)$$

It is obvious that the periodic auto-correlation ($\ell_p = \ell_q$) equals to 1 only when $\tau = 0$.

2.2.1.2 Time reversal property

The time reversal sequence of \mathbf{g}_N equals to itself, that is

$$g_N[N - k] = e^{-j\frac{\pi((N-k)^2)}{N}} = e^{-j\frac{\pi k^2}{N}} e^{j2\pi k} e^{-j\pi N} = g_N[k]. \quad (2.5)$$

2.2.1.3 Constant envelope property after IDFT

The root cause of the high PAPR problem in OFDM-CDMA systems using Hadamard codes is that the constant envelope of the Hadamard code is destroyed after IDFT (or IFFT) operation. Clearly both polyphase sequence \mathbf{g}_N and its phase-shifted version \mathbf{g}_N^ℓ have constant envelope (i.e., $|g_N[k]| = 1$ and $|g_N^\ell[k]| = 1$). Moreover, the IDFT output of these sequences also has constant amplitude property. We let $\mathbf{e}_N = \text{IDFT}\{\mathbf{g}_N\}$. The DFT of the product of two sequences \mathbf{e}_N and \mathbf{e}_N^* equals to the circular convolution of the frequency domain sequences \mathbf{g}_N and its frequency reversal $\{(g_N[N - k])^*\}$ [Proakis, 1996a]. By (2.5), we have $\{(g_N[N - k])^*\} = \mathbf{g}_N^*$. Therefore, the circular convolution of \mathbf{g}_N and \mathbf{g}_N^* equals to the circular (periodic) auto-correlation. Using (2.3), the DFT of $\{e_N[q]e_N^*[q]\}$ can be expressed as

$$\text{DFT}\{e_N[q]e_N^*[q]\} = \sqrt{N}R_{g_N, g_N}[\tau = 0] |_{\ell_p = \ell_q} = \sqrt{N}\delta[q], \quad q = 0, \dots, N - 1. \quad (2.6)$$

Taking IDFT of both sides of (2.6), we have

$$\{e_N[q]e_N^*[q]\} = \frac{1}{\sqrt{N}} \sum_{p=0}^{N-1} \left(\sqrt{N}\delta[p] \right) e^{j\frac{2\pi qp}{N}} = 1, \quad q = 0, \dots, N - 1. \quad (2.7)$$

Therefore, IDFT output of \mathbf{g}_N has constant amplitude. Since \mathbf{g}_N^ℓ is the phase-shifted version of \mathbf{g}_N , IDFT output of \mathbf{g}_N^ℓ has constant amplitude as well. However, for Hadamard codes their circular convolution in frequency domain does not equal to $\delta[\tau]$, therefore their time-domain signal amplitudes do not have constant envelopes. This unique and interesting property of polyphase sequences motivates us to investigate the feasibility of using the polyphase sequence with variable spreading factors in OFDM-CDMA systems to mitigate the high PAPR problem.

2.2.2 OFDM-CDMA System Using Polyphase Codes

2.2.2.1 Spreading code construction

In this section, we propose an approach to construct polyphase codes with variable spreading factors which have not been addressed in previous works [Popović, 1998], [Tan and Stüber, 2005]. Suppose that there are $N = 2^n$ subcarriers in the OFDM-CDMA system. The variable spreading factor polyphase code set with maximum spreading factor N is built based on the primitive polyphase sequences of the length N . With a specific spreading factor $M = 2^m$ ($m \leq n$), each of the $N_s = \frac{N}{M} = 2^{n-m}$ data symbols is spread and mapped to M equal spaced subcarriers. The spreading code used to spread the i th ($i \in \{0, \dots, N_s - 1\}$) symbol on subcarriers $k = pN_s + i$, ($p = 0, \dots, M - 1$) is generated by the polyphase decomposition of the original sequence \mathbf{g}_N^ℓ with factor N_s . The resulted code sequence, which consists of M polyphase components of the original sequence \mathbf{g}_N^ℓ , is denoted as $\mathbf{c}_{M,i}^\ell$. Then, the p th element of the sequence $\mathbf{c}_{M,i}^\ell$ is given by

$$c_{M,i}^\ell[p] = g_N^\ell[p \cdot N_s + i] = e^{-j\frac{\pi(i^2+2i\ell)}{N}} e^{-j\frac{\pi(N_s p^2+2p(\ell+i))}{M}}. \quad (2.8)$$

Note that the term $e^{-j\frac{\pi(N_s p^2+2p(\ell+i))}{M}}$ in (2.8) is not a CAZAC sequence since N_s is not relatively prime to M . Therefore, $\mathbf{c}_{M,i}^\ell$ is not a CAZAC sequence either. In other words, although the primitive polyphase sequence is Zadoff-Chu sequence, the spreading sequence derived in (2.8) is not.

CHAPTER 2. POLYPHASE CODES FOR UPLINK OFDM-CDMA SYSTEMS

Consider two sequences $\mathbf{c}_{M_p, i_p}^{\ell_p}$ and $\mathbf{c}_{M_q, i_q}^{\ell_q}$ for spreading sequences. For a sequence $\mathbf{c}_{M, i}^{\ell}$ used as spreading sequence in OFDM-CDMA systems, the subscript i is the starting index of subcarriers that the sequence is mapped to. Let $N_p = \frac{N}{M_p}$, and $N_q = \frac{N}{M_q}$ stands for number of transmit modulation symbols. That is, sequence $\mathbf{c}_{M_p, i_p}^{\ell_p}$ is spread to subcarriers $pN_p + i_p$, and sequence $\mathbf{c}_{M_q, i_q}^{\ell_q}$ is spread to subcarriers $qN_q + i_q$. Without loss of generality, we assume that $M_p \geq M_q$. Let $(\cdot)_N$ denotes the modulo-by- N operation. If the two sequences are not mapped to overlapping subcarriers (i.e., $(i_q - i_p)_N \neq 0$), their periodic cross-correlation is always zero since they are orthogonal in the frequency domain. Therefore, we only examine the periodic cross-correlation between $\mathbf{c}_{M_q, i_q}^{\ell_q}$ and $\mathbf{c}_{M_p, i_p}^{\ell_p}$ when they are mapped to the same subcarriers. Since the elements of $\mathbf{c}_{M_p, i_p}^{\ell_p}$ are mapped to the same subcarriers as $\mathbf{c}_{M_q, i_q}^{\ell_q}$ only on subcarriers $i_q, N_q + i_q, \dots, (M_q - 1)N_q + i_q$. Hence, the periodic cross-correlation of the two sequences $\mathbf{c}_{M_p, i_p}^{\ell_p}$ and $\mathbf{c}_{M_q, i_q}^{\ell_q}$ becomes equivalent as the periodic cross-correlation of $\mathbf{c}_{M_q, i_q}^{\ell_p}$ and $\mathbf{c}_{M_q, i_q}^{\ell_q}$. That is

$$\begin{aligned}
 R_{\mathbf{c}_{M_p, i_p}^{\ell_p}, \mathbf{c}_{M_q, i_q}^{\ell_q}}[\tau] &= R_{\mathbf{c}_{M_q, i_q}^{\ell_p}, \mathbf{c}_{M_q, i_q}^{\ell_q}}[\tau] \\
 &= \frac{1}{M_q} e^{j \frac{2\pi i_q (\ell_q - \ell_p)}{N}} \sum_{k=0}^{M_q-1} e^{-j \frac{\pi (N_q k^2 + 2k\ell_p)}{M_q}} e^{j \frac{\pi (N_q (k+\tau)^2 + 2(k+\tau)\ell_q)}{M_q}} \\
 &= \frac{1}{M_q} e^{j \frac{2\pi i_q (\ell_q - \ell_p)}{N}} e^{j \frac{\pi N_q (\tau^2 + 2\tau\ell_q)}{M_q}} \sum_{k=0}^{M_q-1} e^{j \frac{2\pi k (N_q \tau + \ell_q - \ell_p)}{M_q}} \\
 &= \frac{1}{M_q} e^{j \frac{2\pi i_q (\ell_q - \ell_p)}{N}} e^{j \frac{\pi N_q (\tau^2 + 2\tau\ell_q)}{M_q}} \delta[(N_q \tau + \ell_q - \ell_p)_{M_q}] \\
 &= \frac{1}{M_q} e^{j \frac{2\pi i_q (\ell_q - \ell_p)}{N}} e^{j \frac{\pi N_q (\tau^2 + 2\tau\ell_q)}{M_q}} \delta[(\tau + \frac{(\ell_q - \ell_p)}{N_q})_{M_q}]. \tag{2.9}
 \end{aligned}$$

Then, it is obvious that if $(\ell_q - \ell_p)/N_q$ is an integer the zero cross-correlation zone has the length of $|\ell_q - \ell_p|/N_q$. On the other hand, if $(\ell_q - \ell_p)/N_q$ is not an integer, $\delta[(N_q \tau + \ell_q - \ell_p)_{M_q}]$ always equals to zero.

2.2.2.2 OFDM-CDMA system using polyphase codes

Now consider the OFDM-CDMA system using polyphase codes given in (2.9) as spreading codes. According to (2.8), the p th chip of the i th data symbol d_i^u of user u with spreading factor $M = 2^m$ is transmitted on subcarrier $k = pN_s + i$. The transmitted signal on subcarrier k , denoted by $X_i^u[pN_s + i]$, can be expressed as

$$X_i^u[pN_s + i] = d_i^u c_{M,i}^{\ell_u}[p], \quad p = 0, \dots, M - 1. \quad (2.10)$$

Hence, the vectors \mathbf{X}_i^u , $i \in \{0, \dots, N_s - 1\}$, are interlaced in the frequency domain. Therefore, the frequency domain transmitted vector is given by $\mathbf{X}^u = \sum_{i=0}^{N_s-1} \mathbf{X}_i^u$. The major benefit for equal-space spreading is to ensure the IDFT outputs have either constant envelope or low PAPR. Equal-space spreading also provides the benefit of better frequency diversity for transmitted data. The discrete-time transmitted signal, denoted by $x^u[q]$, is given by

$$x^u[q] = \frac{1}{\sqrt{N}} \sum_{k=0}^{N-1} X^u[k] e^{j \frac{2\pi q k}{N}}, \quad q = 0, \dots, N - 1. \quad (2.11)$$

A cyclic prefix (CP) with an appropriate length L_{cp} is then appended to the OFDM symbol \mathbf{x}^u for transmission. Suppose that the sample duration in the OFDM-CDMA system is T_c . The maximum channel delay length of a user is defined as its maximum channel delay spread (in time) normalized by the sample duration T_c . Assume that there are totally U users in the system and the maximum multipath channel length of user u is L^u . In order to avoid inter-symbol interference (ISI), the CP length L_{cp} needs to cover the maximum channel delay spread plus the propagation delay of an individual user τ^u . That is $\tau^u/T_c + L^u \leq L_{cp} + 1$, for all u [Verde, 2004]. This requirement is called quasi-synchronization. In practical systems, the timing advance technique can be used to align uplink timing between users by the amount of propagation delay. Then, the CP length only needs to cover the maximum channel delay spread.

During one OFDM symbol duration, the multipath channel impulse response of

user u is given by $\mathbf{h}^u = [h^u[0], h^u[1], \dots, h^u[L^u - 1]]^T$. We assume that the uplink timing of all users is synchronized. At the receiver, after discarding the CP the received signal is demodulated by an N -point DFT, and the k th subcarrier output during the one OFDM symbol interval can be expressed as

$$Y[k] = \sum_{u=0}^{U-1} H^u[k] X^u[k] + W[k], \quad k = 0, \dots, N - 1, \quad (2.12)$$

where $H^u[k] = \frac{1}{\sqrt{N}} \sum_{q=0}^{L^u-1} h^u[q] e^{-j \frac{2\pi k q}{N}}$ is the channel impulse response of the k th subcarrier in frequency domain and $W[k] = \sum_{q=0}^{N-1} n_0[q] e^{-j \frac{2\pi k q}{N}}$, $n_0[q]$ is the complex-valued and also circularly symmetric Gaussian noise with power spectral density $\frac{N_0}{2}$. The system diagram of the OFDM-CDMA system using polyphase codes is shown in Fig. 2.1.

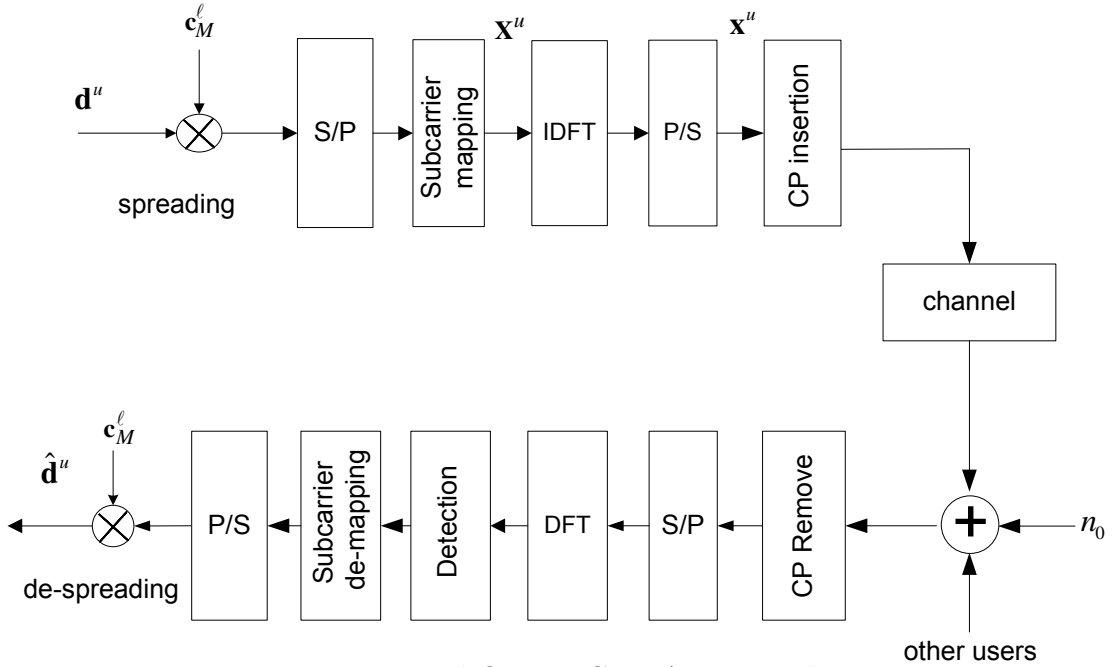


Figure 2.1: Proposed OFDM-CDMA system diagram.

The spreading (or despreading) of one data symbol by polyphase code with a spreading factor M requires M complex multiplications while spreading (or despread-

ing) by Hadamard code requires M complex additions (or sign reversions). For one OFDM symbol where N/M data symbols are transmitted, it takes a total of N (i.e., $N/M \times M$) complex multiplications. Hence, the overall complexity of OFDM-CDMA system using polyphase codes (including DFT operation) equals to $N + N \log N$ complex multiplications. For Hadamard codes, the overall complexity including DFT operation equals to $N \log N$ complex multiplications and N complex additions. Therefore, the implementation complexity difference between the two systems is trivial.

2.2.2.3 Z-orthogonal code tree

Since spreading codes used by different users on non-overlapping subcarrier sets are always orthogonal to each other in the frequency domain, it is only necessary to discuss code orthogonality between spreading sequences using the same (or overlapping) subcarrier sets. For example, for the case $N=16$, spreading sequences $\mathbf{c}_{8,1}^\ell$ and $\mathbf{c}_{4,2}^\ell$ are applied on non-overlapping subcarriers and are therefore orthogonal to each other in frequency domain. For notational brevity, we omit the index i of $\mathbf{c}_{M,i}^{\ell_p}$ here.

In conventional spread-spectrum communication systems, orthogonal variable spreading factor (OVSF) codes are arranged in a tree structure based on their orthogonality. In this paper, we define a Z-orthogonal variable spreading factor (ZO-VSF) code tree similar to the conventional code tree for Hadamard codes. Each channelization code in the new ZO-VSF code tree has a unique description of \mathbf{c}_M^ℓ where M is the spreading factor of the code and ℓ is the code index, $0 \leq \ell \leq M - 1$. Each level M in the code tree defines channelization codes corresponding to spreading factor M . The ZO-VSF code tree is constructed based on Z-orthogonality, as given in (2.9), between polyphase codes and has following properties:

P1) The ZO-VSF code tree offers the same code set size as conventional OVSF Hadamard code tree.

P2) Any two polyphase codes $\mathbf{c}_M^{\ell_p}$ and $\mathbf{c}_M^{\ell_q}$ at the M th level of code tree are Z-orthogonal.

P3) A polyphase code \mathbf{c}_M^ℓ is Z-orthogonal to all codes at the code tree level $2M$ except for its two children codes \mathbf{c}_{2M}^ℓ and $\mathbf{c}_{2M}^{M+\ell}$.

Proof of P3):

Using (2.3), (2.8) and (2.9), the cross-correlation between any two polyphase spreading sequences $\mathbf{c}_{M_p}^{\ell_p}$ and $\mathbf{c}_{M_q}^{\ell_q}$ equals to $\frac{1}{M_q} e^{\frac{j\pi N_q(\tau^2 + 2\tau\ell_q)}{M_q}} \delta[(N_s\tau + \ell_q - \ell_p)_M]$ with $M = \min\{M_q, M_p\}$. When $\Delta\ell = kM$, we have

$$R_{\mathbf{c}_M^{\ell_p}, \mathbf{c}_M^{\ell_q}}[0] \neq 0, \Delta\ell = \ell_q - \ell_p = kM. \quad (2.13)$$

According to the second criterion in (2.4), $\mathbf{c}_{M_p}^{\ell_p}$ and $\mathbf{c}_{M_q}^{\ell_q}$ are not Z-orthogonal. \square

The ZO-VSF code tree of polyphase codes can be built according to (2.9) and (2.13) as follows. Starting with $M = 1$, and $\ell_p = 0$ for a node in the code tree, say spreading code $\mathbf{c}_M^{\ell_p}$, obtain its children code as $\mathbf{c}_{2M}^{\ell_p}$ and $\mathbf{c}_{2M}^{M+\ell_p}$. Similarly, the children codes of $\mathbf{c}_{2M}^{\ell_p}$ are $\mathbf{c}_{4M}^{\ell_p}$ and $\mathbf{c}_{4M}^{2M+\ell_p}$, and the children codes of $\mathbf{c}_{2M}^{M+\ell_p}$ are $\mathbf{c}_{4M}^{M+\ell_p}$ and $\mathbf{c}_{4M}^{3M+\ell_p}$. Repeat these steps until it reaches the maximum spreading factor N .

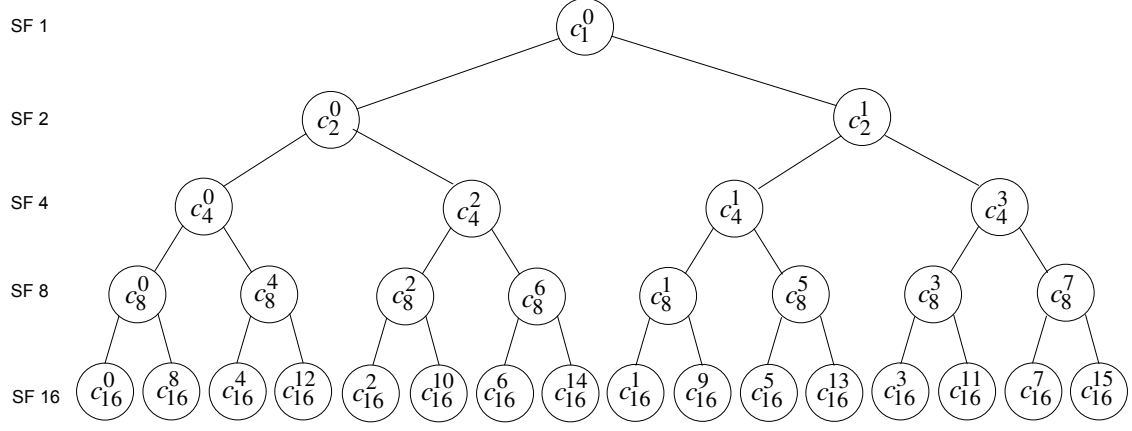
Consider one example of $N=16$ (that is, $n = 4$). The code set of spreading factor 4 ($m = 2$) are generated from the original polyphase sequences of length 16 using (2.8). Code sets of spreading factors other than 4 are generated similarly. If code \mathbf{c}_4^0 is used, then all other codes that are not Z-orthogonal to it, i.e., codes \mathbf{c}_1^0 , \mathbf{c}_2^0 , \mathbf{c}_8^0 , \mathbf{c}_8^4 , \mathbf{c}_{16}^0 , \mathbf{c}_{16}^4 , \mathbf{c}_{16}^8 , and \mathbf{c}_{16}^{12} are blocked according to (2.13). In this way, a ZO-VSF code tree is built as shown in Fig. 2.2.

2.3 Performance Analysis

In this section, we analyze the PAPR and the MAI of the OFDM-CDMA system using polyphase codes.

2.3.1 PAPR Analysis

PAPR is the metric that describes the degree of the transmitted signal amplitude fluctuation, and is an important metric in transmitter design. A general definition of


 Figure 2.2: Polyphase sequence code tree for $N=16$.

discrete-time PAPR is given by

$$\text{PAPR} \equiv \frac{\max\{|x^u[q]|^2\}}{E[|x^u[q]|^2]}. \quad (2.14)$$

where $x^u[q]$ is the transmitted signal given by (2.11). In (2.14), the term of $E[|x^u[q]|^2]$ is the average power of an OFDM symbol. When the data symbols $X^u[k]$ in (2.11) are of unitary power, the OFDM symbols $x^u[q]$ are also of unitary power. The term $\max\{|x^u[q]|^2\}$ is the largest power of output signals within one OFDM symbol. Note that a system with constant envelope has $\max\{|x^u[q]|^2\}$ being unitary power.

The PAPR performance of the OFDM-CDMA system using the proposed orthogonal polyphase codes is analyzed next. Assume there are $N = 2^n$ subcarriers in the system and the spreading factor $M = 2^m$ is used by a user. Assume M-PSK modulation is employed. The user can transmit up to $N_s = \frac{N}{M}$ data symbols during one OFDM symbol interval. After data spreading and subcarrier mapping given by (2.10), the chips vector \mathbf{X}_i^u is fed into IDFT. Here, \mathbf{X}_i^u is defined as the frequency domain chips sequence $\{d_i^u c_{M,i}^\ell[p]\}$ upsampled by factor M and multiplied by a circulant operator matrix \mathbf{C}_i as defined in the Appendix. Recall that the frequency domain

transmitted vector is given by $\mathbf{X}^u = \sum_{i=0}^{N_s-1} \mathbf{X}_i^u$. Due to the linearity of IDFT, we have

$$\text{IDFT}\{\mathbf{X}^u\} = \sum_{i=0}^{N_s-1} \text{IDFT}\{\mathbf{X}_i^u\}. \quad (2.15)$$

This property provides a different angle for us to investigate the PAPR of the system. OFDM-CDMA systems using polyphase codes will have different PAPR performance depending on the used spreading factors. We have the following proposition for PAPR of OFDM-CDMA systems using polyphase codes. The detailed proof is given in the Appendix.

Proposition 1: *For the medium to high spreading factor case ($2^m \geq 2^{\lceil n/2 \rceil}$), the OFDM-CDMA system using the proposed polyphase codes has constant envelope (before pulse shape filtering). In this case, the IDFT output of each data symbol sequence is still unitary power and does not overlap with other data symbols' IDFT output. In this way, the constant power property of output signals after IDFT operation is kept. For the low spreading factor case ($1 < 2^m < 2^{\lceil n/2 \rceil}$), the OFDM-CDMA system using the proposed polyphase codes has low PAPR. In this case, the theoretical peak of output signals of IDFT operation is bounded by $10 \cdot \log_{10} 2^{n-2m}$.*

In practical OFDM-CDMA systems, usually small spreading factors will not be used because they do not provide enough frequency spreading gain [Cai *et al.*, 2004]. Therefore, the spreading factors of polyphase codes will be reasonably large in practical OFDM-CDMA system. Then, the PAPR of an OFDM-CDMA system using the polyphase codes will be dramatically lower than that of an OFDM-CDMA system using Hadamard codes, as illustrated in Section IV by simulation results.

2.3.2 MAI Analysis

In this paper, MAI analysis is performed based on the following assumptions:

A1) The maximum channel delay spread for all users is L_{\max} and the minimum spreading factor used in the system is greater than maximum channel delay spread,

i.e. $M > L_{\max}$, to ensure the maximum frequency diversity [Cai *et al.*, 2004].

A2) The uplink timing of all users is synchronized. That is, the CP covers all the timing difference caused between users caused by channel delay spread and propagation delay.

A3) There is no phase error generated in the modulation and demodulation processes.

In an OFDM-CDMA system using polyphase codes, users with different spreading factors experience difference MAI. The user with the smallest spreading factors among all users suffer from the highest MAI. In this section, the MAI of the user with the smallest spreading factor will be analyzed and regarded as the performance lower bound.

We assume that a particular user u has the smallest spreading factor M_u . Then, user u can transmit up to $N_u = N/M_u$ data symbols per OFDM symbol. For the i_u th data symbol of user u spread on subcarrier $k = pN_u + i_u$, the i_v th data symbol of another user v spread on the same subcarrier $k = qN_v + i_v$ could cause interference. Therefore, we have $pN_u + i_u = qN_v + i_v$ and $i_v = (i_u)_{N_v}$. Using (2.8), (2.9) and A2), the received frequency domain chip signal of user u at the k th subcarrier can be written as

$$Y_{i_u}^u[k] = H^u[k]d_{i_u}^u c_{M_u, i_u}^{\ell_u}[p] + I[k] + W[k], \quad (2.16)$$

where $I[k] = \sum_{v=1, v \neq u}^U H^v[k]d_{i_v}^v c_{M_v, i_v}^{\ell_v}[q]$ represents the MAI term on the k th subcarrier.

We assume that perfect channel information of user u is known at the receiver. After the matched filtering is applied, the MAI term of the i_u th data symbol of user u can be expressed as

$$\begin{aligned} \text{MAI} &= \sum_{p=0}^{M_u-1} I[k](H^u[pN_u + i_u]c_{M_u, i_u}^{\ell_u}[p])^* \\ &= \sum_{p=0}^{M_u-1} \sum_{v=1, v \neq u}^U H^v[qN_v + i_v]d_{i_v}^v c_{M_v, i_v}^{\ell_v}[q](H^u[pN_u + i_u]c_{M_u, i_u}^{\ell_u}[p])^*. \end{aligned} \quad (2.17)$$

Similar to the analysis of periodic cross-correlation of two sequences in Section II.B,

(2.17) can be rewritten as

$$\begin{aligned}
 \text{MAI} &= \sum_{v=1, v \neq u}^U \sum_{p=0}^{M_u-1} H^v[pN_u + i_u] d_{i_v}^v c_{M_u, i_u}^{\ell_v}[p] (H^u[pN_u + i_u] c_{M_u, i_u}^{\ell_u}[p])^* \\
 &= \sum_{v=1, v \neq u}^U d_{i_v}^v e^{j \frac{2\pi i_u (\ell_u - \ell_v)}{N}} \sum_{p=0}^{M_u-1} H^v[p \cdot N_u + i_u] (H^u[p \cdot N_u + i_u])^* e^{j \frac{2\pi p (\ell_u - \ell_v)}{M_u}} \quad (2.18)
 \end{aligned}$$

Denote $\Phi_{\ell_u, \ell_v}(i_u) = \sum_{p=0}^{M_u-1} H^v[p \cdot N_u + i_u] (H^u[p \cdot N_u + i_u])^*$ as the channel cross-correlation term without frequency shift. Then, we need to examine the term $\Phi_{\ell_u, \ell_v}(i_u)$ in order to explore the structure of MAI. Note that for any $i_u \neq 0$, $\Phi_{\ell_u, \ell_v}(i_u)$ is a frequency-shifted version of $\Phi_{\ell_u, \ell_v}(0)$. Then, we study the channel cross-correlation term $\Phi_{\ell_u, \ell_v}(0)$ first. Note that $H^u[pN_u]$ is the down-sampled version (with factor N_u) of $H^u[k]$. After dropping the constant N_u , $\tilde{H}^u[p]$ becomes the down-sampled version of $H^u[k]$. Then, we have

$$\tilde{H}^u[p] = H^u[pN_u] = \frac{1}{\sqrt{N}} \sum_{k=0}^{N-1} h^u[k] e^{-j \frac{2\pi p N_u k}{N}} = \frac{1}{\sqrt{N}} \sum_{k=0}^{N-1} h^u[k] e^{-j \frac{2\pi p k}{M_u}}. \quad (2.19)$$

The IDFT of $\tilde{H}^u[p]$ is given by

$$\begin{aligned}
 \tilde{h}^u[p] &= \frac{1}{\sqrt{M_u}} \sum_{q=0}^{M_u-1} \left(\frac{1}{\sqrt{N}} \sum_{k=0}^{N-1} h^u[k] e^{-j \frac{2\pi q k}{M_u}} \right) e^{j \frac{2\pi p q}{M_u}} = \frac{1}{\sqrt{N M_u}} \sum_{k=0}^{N-1} h^u[k] \sum_{q=0}^{M_u-1} e^{j \frac{2\pi (k-p) q}{M_u}} \\
 &= \frac{M_u}{\sqrt{N M_u}} \sum_{q=0}^{N_u-1} h^u[p + q M_u] = \frac{1}{\sqrt{N_u}} \sum_{q=0}^{N_u-1} h^u[p + q M_u]. \quad (2.20)
 \end{aligned}$$

Combining (2.18-2.20) and applying Plancherel theorem [Proakis, 1996a], we have

$$\Phi_{\ell_u, \ell_v}(0) = \sum_{p=0}^{M_u-1} H^v[p \cdot N_u] H^u[p \cdot N_u]^* = \sum_{p=0}^{M_u-1} \tilde{h}^u[p] \tilde{h}^v[p]^*. \quad (2.21)$$

Using (2.21) and applying the circular time and frequency shift property, then (2.18) can be expressed as

$$\text{MAI} = \sum_{v=1, v \neq u}^U d_{i_v}^v e^{j \frac{2\pi i_u \Delta \ell}{N}} \sum_{p=0}^{M_u-1} \tilde{h}^u[p] \tilde{h}_{\Delta \ell}^v[p]^* = \sum_{v \neq u} d_{i_v}^v e^{j \frac{2\pi i_u \Delta \ell}{N}} R_{\tilde{h}_u \tilde{h}_v}((\Delta \ell)_{M_u}), \quad (2.22)$$

CHAPTER 2. POLYPHASE CODES FOR UPLINK OFDM-CDMA SYSTEMS

where $\Delta\ell = (\ell_u - \ell_v)$ is the cyclic shift distance between codes used by the two users, $\tilde{\mathbf{h}}_{\Delta\ell}^v = \mathbf{C}_{\Delta\ell}\tilde{\mathbf{h}}^v$ is actually $\tilde{\mathbf{h}}^v$ being circularly shifted by $(\Delta\ell)_{M_u}$, and $R_{\tilde{\mathbf{h}}_u\tilde{\mathbf{h}}_v}$ is the time-domain channel delay spread circular cross-correlation of $\tilde{\mathbf{h}}^u$ and $\tilde{\mathbf{h}}^v$.

Recall that the length of the time-domain channel impulse response of the user u is L^u . Assume that two users u and v have $\max\{L^u, L^v\} \leq L_{\max} < M = \min\{M_u, M_v\}$. Then, we have $\{\tilde{h}^u[p]\} = 0$, for $p = L^u, \dots, M-1$. When the cyclic shift distance between codes used by users u and v satisfies following condition

$$L^u \leq (\Delta\ell)_M \leq M - L^v, \quad (2.23)$$

there is no MAI between them. This is because user v 's channel impulse response $\tilde{\mathbf{h}}^v$ is circularly shifted by $(\Delta\ell)_M$ and $L^v \leq M - (\Delta\ell)_M$, i.e., each element of $\{\tilde{h}_{\Delta\ell}^v[p]\} = 0$, $p = 0, \dots, L^u - 1$. Furthermore, each element of $\{\tilde{h}^u[p]\} = 0$, for $p = L^u, \dots, M-1$. Therefore, the circular cross-correlation of two users' channel impulse responses, i.e., $\sum_{p=0}^{M-1} \tilde{h}^u[p](\tilde{h}_{\Delta\ell}^v[p])^*$, equals to 0 in (2.22). As indicated in (2.23), the minimum spreading factor M should be no less than $L^u + L^v$. When $L^u = L^v = L_{\max}$, we have

$$M \geq 2L_{\max} \quad (2.24)$$

Therefore, the minimum ZCZ equals to L_{\max} .

Suppose that there are U users in the system, the spreading factor of user u is M_u . For the primitive polyphase sequence with length N , there are N unique cyclic shifts. Since the minimum ZCZ $\geq L_{\max}$, those cyclic shifts are divided into zones with length of L_{\max} . Therefore, the maximum number of ZCZs obtained in this way is $\lfloor N/L_{\max} \rfloor$. As the code tree structure indicates, a code with spreading factor M_u ($M_u \leq N$) blocks N/M_u codes with the maximum spreading factor N in the code tree. The N/M_u blocked codes correspond to N/M_u equal-distant (distance is M_u) cyclic shifts of the primitive polyphase sequence with length N . From the code assignment perspective, assignment of a code with spreading factor M_u is equivalent as assignment of N/M_u equal-distant (distance is M_u) cyclic shifts of the primitive polyphase sequence of length N .

The equivalent number of the cyclic shifts used by users in the primitive polyphase sequence of length N , denoted by U_e , is given by

$$U_e = \sum_{u=1}^U \frac{N}{M_u} \quad (2.25)$$

If $U_e \leq \lfloor N/L_{\max} \rfloor$, proper code assignment can be performed to ensure that there is no MAI among codes. The codes are assigned in the order of ascending spreading factor. Subsequent codes are assigned in such a way that their corresponding cyclic shifts are at least L_{\max} away from previously assigned cyclic shifts. In this way, there is no mutual interference between any two users. When the condition $U_e \leq \lfloor N/L_{\max} \rfloor$ is not met, there exist at least two users u and v whose cyclic shift difference $|\ell_u - \ell_v|$ is less than L_{\max} . Hence, MAI exists among users.

2.4 Simulation results

This section presents simulation results of PAPR and BER performance of OFDM-CDMA systems using polyphase codes and Hadamard codes respectively. Table 1 summarizes the system parameters used in the simulation.

2.4.1 PAPR Performance

Root raised cosine (RRC) filtering is necessary for reducing out-of-band emissions and meeting transmission spectrum mask requirement. RRC filtering (with typical roll-off factor 0.22) will increase PAPR of any system with constant envelope by more than 4 dB. In practical systems, only PAPR results after RRC filtering will be considered. Therefore, instead of presenting the PAPR results after IDFT, we present the PAPR results after RRC filtering.

PAPR of OFDM-CDMA systems with 256 subcarriers using orthogonal polyphase codes is compared to PAPR yielded by Hadamard codes in Fig. 2.3 (a). Two spreading factors 8 and 16 are used for comparison. PAPR of orthogonal polyphase codes

of spreading factor 16 corresponds to the case of medium to high spreading factor in **Proposition 1**, where the OFDM-CDMA system using orthogonal polyphase codes has constant envelope before RRC filtering. As we can see, the 99.9% percentile PAPR of OFDM-CDMA system using orthogonal polyphase codes of spreading factor 16 is about 6.6 dB lower than that of OFDM-CDMA system using Hadamard codes. PAPR of orthogonal polyphase codes of spreading factor 8 corresponds to the case of low spreading factor in **Proposition 1**, where the system has low PAPR before RRC filtering. As we can see, the PAPR yielded by orthogonal polyphase codes is about 2.6 dB lower than that yielded by Hadamard codes. Similar trends are observed for OFDM-CDMA system with higher subcarriers. PAPR performance of OFDM-CDMA systems with 1024 subcarriers using orthogonal polyphase codes is compared to that yielded by Hadamard codes in Fig. 2.3 (b). Orthogonal polyphase codes provided about 8.2 dB and 3.7 dB PAPR improvement at spreading factors 32 and 16, respectively.

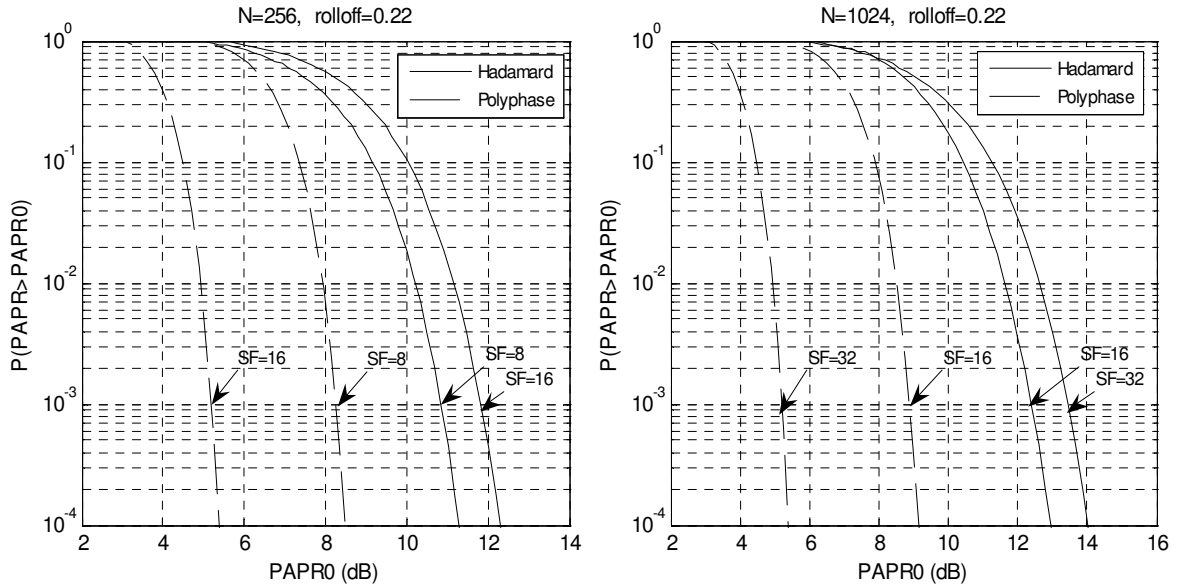


Figure 2.3: PAPR of OFDM-CDMA systems using polyphase codes and Hadamard codes with (a) SF=8 and 16, $N=256$ subcarriers (b) SF=16 and 32, $N=1024$ subcarriers.

2.4.2 Uncoded BER Performance

As forementioned, OFDM-CDMA system using polyphase codes suffers MAI when cyclic shift difference between codes, $\Delta\ell$, is smaller than L_{\max} . Assume that the channel is linearly time-invariant within one OFDM symbol duration and channel information is known at the receiver by using training sequence (or pilots). In the following discussion, it is assumed that each user only uses a single spreading code for uplink transmission. This is a fair assumption. For uplink transmission, (for example, in UMTS 3GPP [Thr, 2003]), supporting variable data rate is achieved by using variable spreading, adaptive modulation and coding instead of multiple codes. This is because multiple code transmission increase PAPR remarkably. Then, the terms "code" and "user" are exchangeable.

The multiuser detection should be performed based on the minimum spreading factor M used in the system. Soft outputs for multi-user detector are needed because partial estimates are employed for the detection of users with spreading factors larger than M [Boariu and Ziemer, 2001]. Without loss of generality, we assume that user u has the minimum spreading factor M in the system. Recall that $H_k^{(u)}$ is the frequency domain channel response of the k th subcarrier of the u th code and c_k^u is the k th element of the u th code. Denote $\mathbf{A}_i^{(u)} = [c_0^u H_i^u, c_1^u H_{i+N_s-1}^u, \dots, c_{M-1}^u H_{MN_s+i-1}^u]^T$, $i = 0, \dots, N_s - 1$, where $\mathbf{A}_i^{(u)}$ contains the code elements and the corresponding channel responses. The vector $\mathbf{A}_i^{(u)}$ of each individual code(user) is concatenated to form a system transmission matrix of the all the codes in the system, which can be expressed as

$$\mathbf{A}_i = \begin{bmatrix} \mathbf{A}_i^{(1)} & \mathbf{A}_i^{(2)} & \dots & \mathbf{A}_i^{(u)} & \dots & \mathbf{A}_i^{(U)} \end{bmatrix}.$$

The linear MMSE MUD solution [Verde, 2004], [Verdu, 1998] in frequency domain can be expressed in matrix form as

$$\mathbf{Z}_i = \mathbf{A}_i^H (\mathbf{A}_i \mathbf{A}_i^H + \sigma^2 \mathbf{I})^{-1}. \quad (2.26)$$

Then, the despread and detected signal vector $\hat{\mathbf{d}} = \mathbf{Z}_i \mathbf{Y}_i$, where \mathbf{Y}_i is the received

signal in frequency domain, and \mathbf{Z}_i is the receiver processing matrix in (2.26). The detected signal vector $\hat{\mathbf{d}}$ contains the data symbols of all the codes in a concatenated form such that $\hat{\mathbf{d}}_i = \begin{bmatrix} \hat{d}_i^{(1)} & \hat{d}_i^{(2)} & \dots & \hat{d}_i^{(u)} & \dots & \hat{d}_i^{(U)} \end{bmatrix}^T$. The $\hat{d}_i^{(u)}$ is either the detected data of user u if its spreading factor equals to M or the i th estimate of user u when its spreading factor is greater than M .

Consider typical urban deployment scenario, where the maximum channel delay spread is $4 \mu s$ (corresponds to $\sim 8T_c$). First, we compare the uncoded BER performance of the two systems when the system using polyphase codes does not have MAI. We consider a OFDM-CDMA system using $N = 256$ subcarriers. According to (2.24), the minimum spreading factor M equals to $2 \times 8 = 16$. BER performance when there are 2 codes of spreading factor 32 and 2 codes of spreading factor 64 in a OFDM-CDMA system using polyphase codes is shown in Fig. 2.4. Codes $\{\mathbf{c}_{32}^1, \mathbf{c}_{32}^{17}\}$ are assigned for the 2 codes using spreading factor 32, codes $\{\mathbf{c}_{64}^{17}, \mathbf{c}_{64}^{33}\}$ are assigned for the 2 codes using spreading factor 64. According to (2.23) and (2.25), there is no MAI among these 4 codes. As observed in Fig. 2.4, BER performance of the OFDM-CDMA system using multiple polyphase codes is the same as single code performance since there is no mutual interference between codes. BER performance yielded by multiple of Hadamard codes is about $1 - 1.5$ dB worse than (at BER of 0.1%) that yielded by single code. That is because of the mutual interference between the two Hadamard codes. Since there is only two codes interfering each other in OFDM-CDMA system using Hadamard codes, performance degradation caused by MAI is not significant. The performance difference between the two systems will increase as the number of interferers increases in the OFDM-CDMA system using Hadamard codes.

Then, we compare the uncoded BER performance of the two systems when both have MAI. We consider OFDM-CDMA systems using polyphase codes and Hadamard codes with different number of codes (8 and 12) of spreading factor 16, $N = 1024$ subcarriers, as shown in Fig. 2.5. When there are 8 polyphase codes used in the

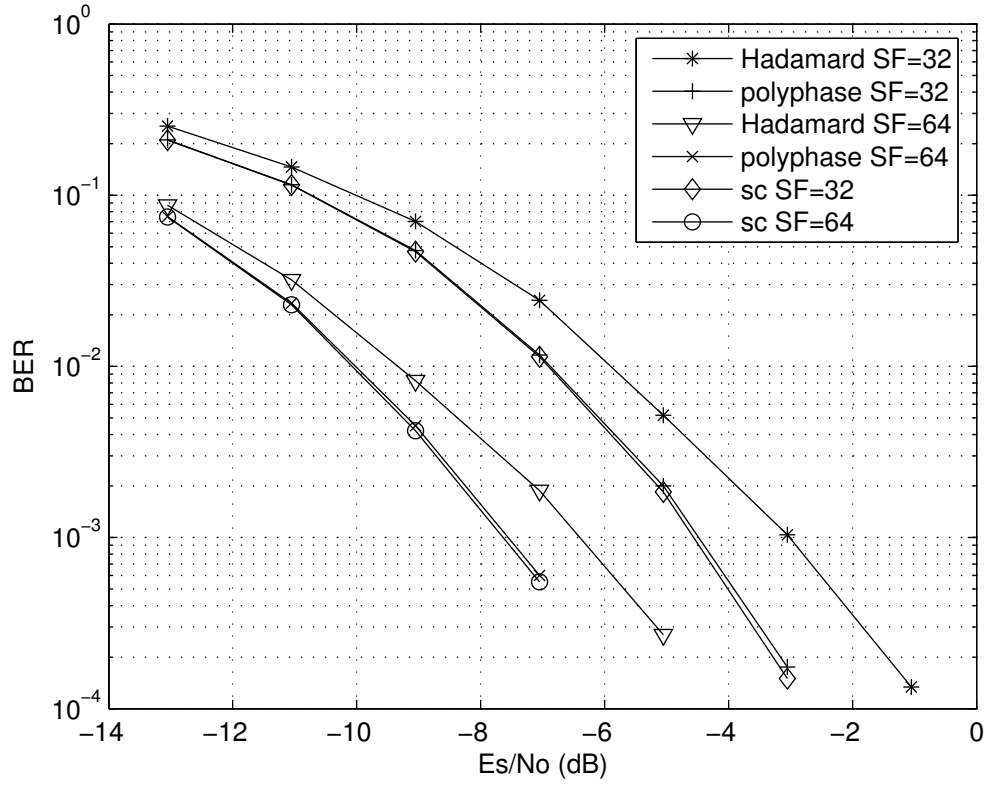


Figure 2.4: BER performance of OFDM-CDMA system using polyphase codes and Hadamard codes with $N = 256$ subcarriers and SF=32, 64.

CHAPTER 2. POLYPHASE CODES FOR UPLINK OFDM-CDMA SYSTEMS

system, $\{\mathbf{c}_{16}^1, \mathbf{c}_{16}^3, \mathbf{c}_{16}^5, \mathbf{c}_{16}^7, \mathbf{c}_{16}^9, \mathbf{c}_{16}^{11}, \mathbf{c}_{16}^{13}, \mathbf{c}_{16}^{15}\}$ are used. When there are 12 polyphase codes used in the system, $\{\mathbf{c}_{16}^1, \mathbf{c}_{16}^2, \mathbf{c}_{16}^3, \mathbf{c}_{16}^4, \mathbf{c}_{16}^5, \mathbf{c}_{16}^6, \mathbf{c}_{16}^7, \mathbf{c}_{16}^8, \mathbf{c}_{16}^9, \mathbf{c}_{16}^{11}, \mathbf{c}_{16}^{13}, \mathbf{c}_{16}^{15}\}$ are used. According to (2.23) and (2.25), there is MAI between any two polyphase codes. Therefore, this corresponding to the worst case for OFDM-CDMA system using polyphase codes.

For a transmit signal with high PAPR to be free from distortion, a large back-off will be used by the power amplifier to provide linear operation. However, large dynamics back-off decreases the power efficiency dramatically, which in turns decreases the battery life. In practical mobile applications, low power efficiency is not tolerable. Therefore, the transmit signal needs to be predistorted (or clipped) to preserve power efficiency. As the PAPR results in Fig. 2.3 (b) indicates, transmit signal in the OFDM-CDMA system using Hadamard codes with spreading factor 16 has a PAPR about 3 dB higher than that using polyphase codes. In order to have the clipped transmit signal in the OFDM-CDMA system using Hadamard codes to have the same PAPR as that using polyphase codes, a clipping of 3 dB is applied. For the OFDM-CDMA system using Hadamard codes, BER performance with and without clipping is evaluated.

As shown in Fig. 2.5, the OFDM-CDMA system using polyphase codes has very close (or the same) BER performance with that using Hadamard codes without clipping. As the number of used codes increases, BER performance yielded by both polyphase codes and Hadamard codes degrades by the same amount. Based on the numerical results, we conclude that the worst case BER of OFDM-CDMA system using polyphase code is approximately the same as that of OFDM-CDMA system using Hadamard codes. However, in practice the OFDM-CDMA system using Hadamard codes cannot achieve such good performance because transmitted signal has to be clipped. As shown in Fig. 2.5, BER performance of the OFDM-CDMA system using Hadamard codes with clipping degrades 2.5 - 3 dB compared to that without clipping and that using polyphase codes. Therefore, in practice the OFDM-CDMA system us-

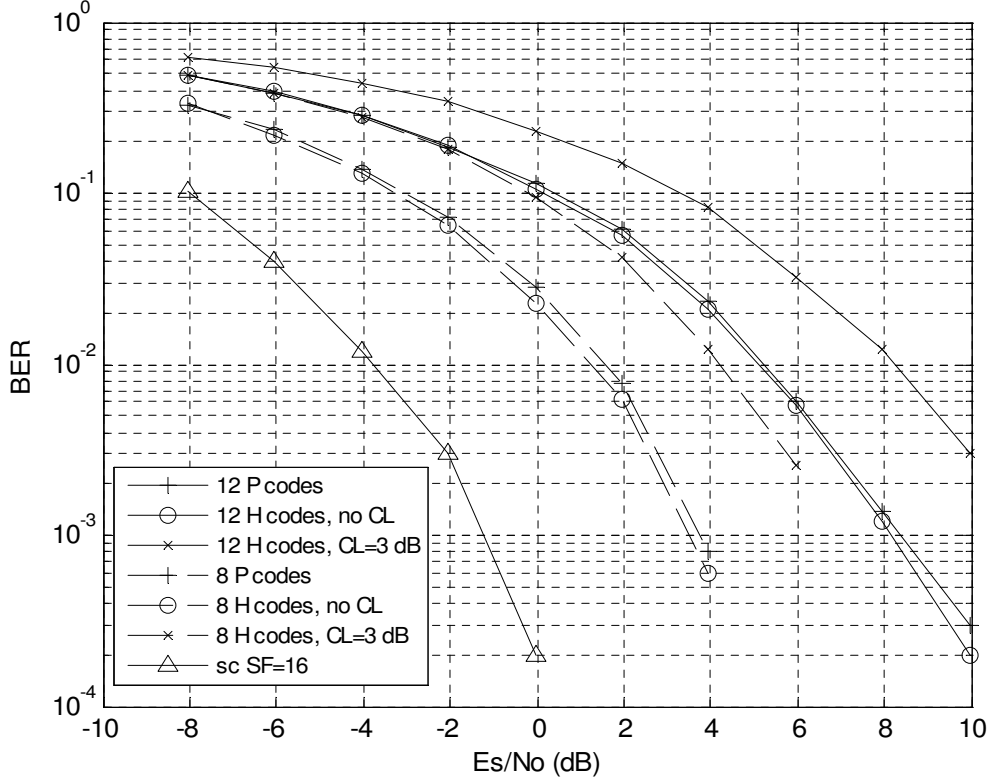


Figure 2.5: BER performance of OFDM-CDMA system using polyphase and Hadamard codes with SF=16, $N = 1024$ subcarriers (for Hadamard codes with 3 dB clipping and without clipping).

ing polyphase codes has better BER performance than that using Hadamard codes.

2.5 Conclusions

In the chapter we proposed to use polyphase codes for OFDM-CDMA systems to address the PAPR problem. Another interesting property of the proposed OFDM-CDMA systems employing the polyphase spreading code is that the MAI between any two codes can be avoided if their cyclic shift distance to their maximum multipath delay spread. Analytical and numerical results show that OFDM-CDMA systems

employing the proposed polyphase codes have remarkably better PAPR performance than that using Hadamard codes. BER performance of OFDM-CDMA systems employing polyphase codes is close to that of system using Hadamard codes without clipping, and better than that with clipping. The low PAPR property with better BER performance makes the proposed OFDM-CDMA systems using the polyphase codes a promising solution to uplink multicarrier systems.

Appendix: Proof of Proposition 1

2.5.1 Medium to high spreading factor case: $2^{\lceil n/2 \rceil} \leq 2^m \leq 2^n$

For notational brevity, we omit the user index u of data symbol d_i^u in the following analysis. After multiplied by the polyphase code sequence $\mathbf{c}_{M,i}^\ell$, the spread data sequence of the i th data symbol d_i after subcarrier mapping can be expressed as

$$\mathbf{X}_i = d_i \tilde{\mathbf{c}}_{M,i}^\ell, \quad (2.27)$$

where $\tilde{\mathbf{c}}_{M,i}^\ell$ is obtained by upsampling $\mathbf{c}_{M,i}^\ell$ by a factor of M followed by multiplying a circulant operator matrix \mathbf{C}_i . \mathbf{I}_N is a $N \times N$ identity matrix and its columns are denoted as $\{\mathbf{v}_1, \mathbf{v}_2, \dots, \mathbf{v}_N\}$. The circulant operator matrix \mathbf{C}_i equals to $\{\mathbf{v}_i, \mathbf{v}_{i+1}, \dots, \mathbf{v}_N, \mathbf{v}_1, \dots, \mathbf{v}_{i-1}\}$, which is a circulant permutation of columns of \mathbf{I}_N .

The IDFT operation of \mathbf{X}_i can be written as $\mathbf{F}_N \mathbf{X}_i$, where \mathbf{F}_N is the $N \times N$ IDFT matrix, whose element on the h th row and k th column, $F_N(h, k)$, is given by

$$F_N(h, k) = \frac{1}{\sqrt{N}} e^{j2\pi h k \frac{\pi}{N}}, \quad h, k = 0, \dots, N-1. \quad (2.28)$$

Denote \mathbf{x}_i as the IDFT of \mathbf{X}_i . For the convenience of analysis, \mathbf{x}_i can also be rewritten as

$$\mathbf{x}_i = \left[\sum_{k=0}^{N-1} F(0, k) X_i(k), \dots, \sum_{k=0}^{N-1} F(h, k) X_i(k), \dots, \sum_{k=0}^{N-1} F(N-1, k) X_i(k) \right]^T. \quad (2.29)$$

CHAPTER 2. POLYPHASE CODES FOR UPLINK OFDM-CDMA SYSTEMS

Suppose that the total number of subcarriers $N = 2^n$, spreading factor $M = 2^m$ and the number of data symbols before spreading $N_s = \frac{N}{M} = 2^{n-m}$. For the i th data symbol, there are data only on the subcarriers $N_s \cdot q + i$, $q = 0, 1, \dots, M-1$, $i = 0, 1, \dots, N_s-1$. In the IDFT operation, data on these subcarriers are multiplied by elements on the k th column of IDFT matrix \mathbf{F}_N , where $k = N_s q + i$. Let us define $x_i(h) = \sum_{k=0}^{N-1} F_N(h, k) X_i(k)$.

We first analyze the h th row of IDFT output, where $h = N_s p + i + s$, $p = 0, 1, \dots, M-1$, $i = 0, 1, \dots, N_s-1$, $i + s \in \{0, \dots, N_s-1\}$. Then $x_i(h)$ is given by

$$x_i(h) = \frac{d_i}{\sqrt{N}} \sum_{k=0}^{N-1} e^{j2hk \frac{\pi}{N}} e^{-j(k^2+2k\ell) \frac{\pi}{N}} = \frac{d_i}{\sqrt{N}} \sum_{k=0}^{N-1} e^{j(2(h-\ell)k-k^2) \frac{\pi}{N}}. \quad (2.30)$$

Plugging $k = N_s q + i$, $q = 0, 1, \dots, M-1$ and $h = N_s p + i + s$ into equation (2.30), we have

$$\begin{aligned} x_i(h) &= \frac{d_i}{\sqrt{N}} \sum_{q=0}^{M-1} e^{j(2(h-\ell)-k)k \frac{\pi}{N}} \\ &= \frac{d_i}{\sqrt{N}} \sum_{q=0}^{M-1} e^{j(N_s 2p+2i+2s-2\ell-N_s q-i)(N_s q+i) \frac{\pi}{N}} \\ &= \frac{d_i}{\sqrt{N}} \sum_{q=0}^{M-1} e^{j(N_s^2(2p-q)q+2N_s(s-\ell)q+2N_s(p-\ell)i+i^2) \frac{\pi}{N}} \\ &= \frac{d_i}{\sqrt{N}} e^{j(2(p-\ell)iN_s+i^2) \frac{\pi}{N}} \sum_{q=0}^{M-1} e^{j(2pq-q^2) \frac{\pi N_s^2}{N}} e^{j \frac{2\pi N_s(s-\ell)q}{N}} \\ &= \frac{d_i}{\sqrt{N}} e^{j(2(p-\ell)i \frac{N}{M}+i^2) \frac{\pi}{N}} \sum_{q=0}^{M-1} e^{j(2pq-q^2) \frac{\pi N}{M^2}} e^{j \frac{2\pi(s-\ell)q}{M}} \\ &= \frac{d_i}{\sqrt{N}} e^{j((p-\ell)i2^{n-m+1}+i^2) \frac{\pi}{N}} \sum_{q=0}^{2^m-1} e^{-j(-2pq+q^2) \frac{\pi}{2^{2m-n}}} e^{j \frac{2\pi(s-\ell)q}{2^m}}. \quad (2.31) \end{aligned}$$

For $(s-\ell)_M = 0$, the $e^{j \frac{2\pi(s-\ell)q}{2^m}} = 1$. Since $2^m/2^{2m-n} = 2^{n-m}$ is an integer and $\frac{1}{\sqrt{N}} \sum_{q=0}^{2^m-1} e^{-j(-2pq+q^2) \frac{\pi}{2^{2m-n}}} = e^{-j \frac{\pi}{4}} e^{j \frac{p^2}{2^{2m-n}} \pi}$ is a discrete Fourier transform pair [Conolly and Good, 1977], we have $x_i(h) = d_i e^{j(2(p-\ell)i2^{n-m}+i^2) \frac{\pi}{2^n}} e^{j \frac{p^2-2^{2m-n-2}}{2^{2m-n}} \pi}$. Therefore,

$|x_i(h)|$ has constant unit energy at the h th row, where $h = N_s p + i + s$, $p = 0 \dots, M - 1$, $(s - \ell)_M = 0$.

For any $(s - \ell)_M \neq 0$, for the convenience of discussion, we let

$$\gamma(q) = e^{-j(-2pq+q^2)\frac{\pi N}{M^2}} e^{j\frac{2\pi(s-\ell)q}{M}}.$$

We found that $\gamma(q) = -\gamma(q + M/2)$ for $N \geq 4$. Therefore, we have

$$\sum_{q=0}^{M-1} e^{-j(-2pq+q^2)\frac{\pi N}{M^2}} e^{j\frac{2\pi(s-\ell)q}{M}} = 0.$$

That is, we have $x_i(h) = 0$ for any h th row, where $h = N_s p + i + s$, $(s - \ell)_M \neq 0$. This means that for data symbol d_i there are non-zero IDFT outputs only at M rows ($h = N_s p + i + s$, $p = 0, 1, \dots, M - 1$, $i = 0, 1, \dots, N_s - 1$, $(s - \ell)_M = 0$). In this way, the IDFT output of each data symbol sequence d_i still has unit power and does not overlap with other data symbols' IDFT output.

2.5.2 Low spreading factor case: $1 < 2^m < 2^{\lceil n/2 \rceil}$

For a data symbol spread over M subcarriers using orthogonal polyphase code, there are non-zero IDFT outputs only at N_s equal-spaced places. If a user transmits N_s symbols on all N subcarriers, then each symbol's output overlaps with other $\frac{N}{M^2} - 1 = 2^{n-2m} - 1$ symbols' outputs. The 2^{n-2m} overlapping symbols are equal-spaced as well. Therefore, each output signal after IDFT operation is the sum of 2^{n-2m} input signals with constant energy. Therefore, the maximum magnitude of output signal is bounded by $10 \log_{10} 2^{n-2m}$. \square

Table 2.1: SIMULATION PARAMETERS

Bandwidth	4.096, 16.384 MHz
FFT size	256, 1024
Subcarrier spacing	16 KHz
OFDM symbol duration	67.38 μs
Useful symbol duration	62.50 μs
Guard period	4.88 μs
Modulation	QPSK
Multipath channel model	ITU Pedestrian PB3 [Thr, 2003]
Maximum channel delay spread	4 μs
Required BER	10^{-2} , 10^{-3}
Roll off factor of RRC filtering	0.22
Spreading sequence	Walsh-Hadamard and Polyphase codes
Length of spreading sequence	16, 32, 64, 128
System load	50% and 75%

Chapter 3

Blind Frequency-dependent I/Q Imbalance Compensation for Direct-conversion Receivers

3.1 Introduction

The evolution of wireless communication systems has been driving the design and implementation of modern radio transceivers. The next-generation wireless networks will support high data-rate applications, which require efficient and low-cost wideband radio design for the terminals. The direct conversion receiver (DCR) has become a major approach to achieving compact and low cost transceiver design in wideband radio [Abidi, 1995]. In DCR, the received signal is quadrature down-converted from RF directly to a baseband signal. One of the problems of DCR, is that downconverter circuits can easily result in a phase and amplitude imbalance between the in-phase (I) and quadrature-phase (Q) signals. Furthermore, to reject interference bands in wideband radio systems, the low-pass filter of I and Q signal branch in DCR require sharper cut-off frequency (imply higher-order design) Fig. 3.1(a). The low-pass filter has the non-ideal characteristics introduced during the manufacture. Those non-ideal

CHAPTER 3. BLIND FREQUENCY-DEPENDENT I/Q IMBALANCE COMPENSATION FOR DIRECT-CONVERSION RECEIVERS

characteristics will cause coefficient discrepancy in transfer function of a filter. Hence, I/Q imbalance parameters are frequency-dependent and thus further complicate the problem for DCR in wideband systems. Due to the inevitable mismatch between the in-phase and quadrature signal paths/components, cross-talk or interference will occur between the mirror-frequencies upon down conversion to baseband. Thus, the I/Q imbalance degrades the effective signal-to-interference power ratio and causes performance degradation. The impact of I/Q imbalance is more severe to systems employing high-order modulations and high coding rates. Therefore, effective I/Q imbalance compensation is essential for the design of high data-rate systems employing DCR.

Some existing I/Q imbalance estimation and compensation methods are based on making use of training signals, e.g., [Tarighat *et al.*, 2005; Schuchert *et al.*, 2001]. However, the transmission of training signals either costs radio resources or is not optimal design for I/Q imbalance compensation and thus blind compensation methods are of great interest. Several blind compensation methods for frequency-dependent I/Q imbalance have been developed. In particular, in [Anttila *et al.*, 2008], a method is developed that exploits a second-order statistic characteristic of the signal called the properness property; and an adaptive compensation based on the least-mean-square (LMS) algorithm is proposed. However, the convergence of the LMS algorithm is typically slow and the steady-state performance exhibits a high variance due to the stochastic nature of the LMS algorithm, which makes it less attractive for high-speed applications. In [Valkama *et al.*, 2001], a compensation method is proposed based on the multichannel blind deconvolution (MBD) algorithm [Haykin, 1996]. This scheme requires the probability density function (pdf) of the transmitted signal to be given. The methods proposed in this paper, however, do not require to know the pdf of the transmitted signal, but only assume that the transmitted signal is a proper and white process, which is a mild condition that is met by practical communication signals. Here we give a necessary and sufficient condition for perfect frequency-dependent I/Q

CHAPTER 3. BLIND FREQUENCY-DEPENDENT I/Q IMBALANCE COMPENSATION FOR DIRECT-CONVERSION RECEIVERS

imbalance compensation, and, based on this condition, we propose a time-domain compensation method.

The OFDM systems are commonly adopted by the next-generation cellular systems. Most of the existing frequency-dependent I/Q imbalance compensation algorithms for OFDM systems are based on special pilot patterns [Xing *et al.*, 2005; Narasimhan *et al.*, 2008]. In this paper, we also propose a blind I/Q imbalance compensation method for OFDM systems. The proposed method first estimates the I/Q imbalance parameters for each subcarrier based on the second-order statistics of the received signal on that subcarrier, and then applies the compensation filter that are calculated based on the estimated parameters.

The remainder of the paper is organized as follows. In Section 3.2, the frequency-dependent I/Q imbalance signal model is described and the compensation problem is formulated. In Section 3.3, we give a condition for perfect I/Q imbalance compensation and based on which we propose a new blind time-domain I/Q imbalance compensation method. In Section 3.4, we develop a blind frequency-domain I/Q imbalance compensation method for OFDM systems. Simulation results are provided in Section 3.5 and finally Section 3.6 concludes the paper.

3.2 System Descriptions

3.2.1 I/Q Imbalance Signal Model

A typical block diagram of the RF front-end for DCR is given in Fig. 3.1(a) and its equivalent mathematical model in Fig. 3.1(b). The received RF signal with a central frequency w_c is expressed as

$$r(t) = 2\mathcal{R}e \{s(t)e^{jw_c t}\} = s(t)e^{jw_c t} + s^*(t)e^{-jw_c t}, \quad (3.1)$$

CHAPTER 3. BLIND FREQUENCY-DEPENDENT I/Q IMBALANCE
COMPENSATION FOR DIRECT-CONVERSION RECEIVERS

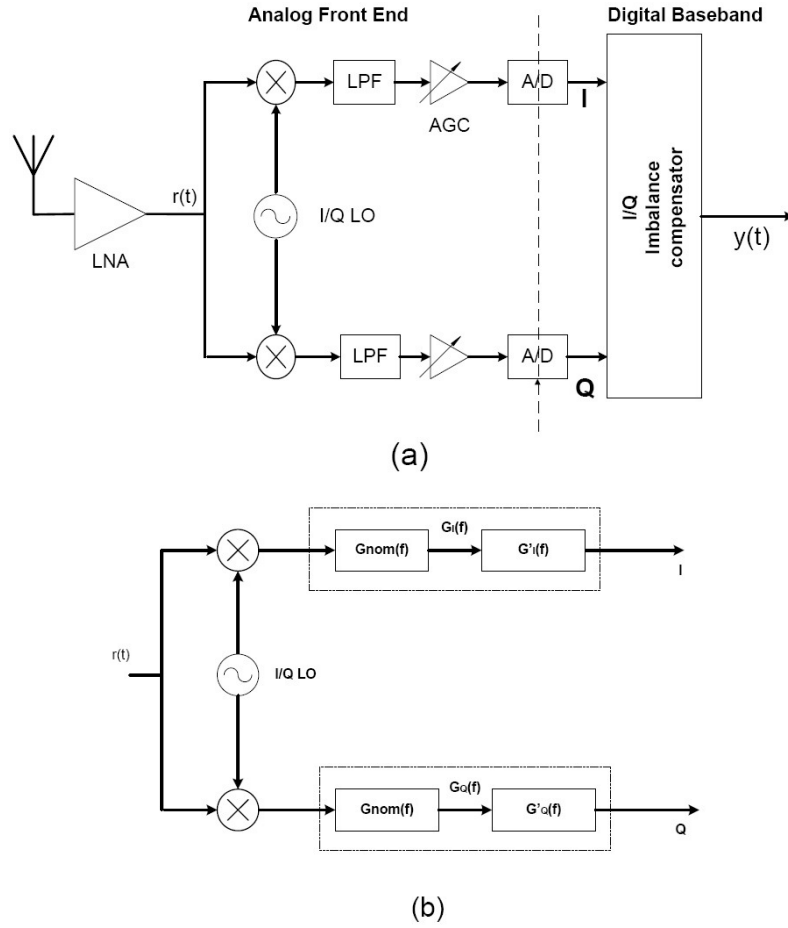


Figure 3.1: (a) The direct-conversion receiver with I/Q imbalance compensation. (b) The effective model of a direct-conversion receiver with I/Q imbalance.

*CHAPTER 3. BLIND FREQUENCY-DEPENDENT I/Q IMBALANCE
COMPENSATION FOR DIRECT-CONVERSION RECEIVERS*

where $s(t) = s_I(t) + js_Q(t)$ is the baseband received signal and $*$ denotes the complex conjugate. In general we have

$$s(t) = h(t, \tau) \otimes d(t)$$

where $d(t)$ is the transmitted data signal, $h(t, \tau)$ is the time-varying channel response and \otimes denotes the convolution. The received RF signal $r(t)$ is directly down-converted by a local oscillator signal $u_{LO}(t)$ with mismatched I and Q branches [Kiss and Prodanov, 2004]. Denote γ and ϕ as the mismatched amplitude and phase, respectively, then the local oscillator signal $u_{LO}(t)$ of an imbalanced quadrature demodulator is given by

$$u_{LO}(t) = \cos(w_c t) - j\gamma \sin(w_c t + \phi). \quad (3.2)$$

The down-converted signal $x(t) = x_I(t) + jx_Q(t)$ is then expressed as

$$\begin{aligned} x(t) &= \mathcal{LPF}_I \{r(t) \cos(w_c t)\} - j\mathcal{LPF}_Q \{\gamma r(t) \sin(w_c t + \phi)\} \\ &= \mathcal{LPF}_I \left\{ \frac{1}{2} [s(t) + s^*(t)] + \frac{1}{2} [s(t)e^{2jw_c t} + s^*(t)e^{-2jw_c t}] \right\} + \\ &\quad j\mathcal{LPF}_Q \left\{ \frac{\gamma}{2j} [s(t)e^{-j\phi} - s^*(t)e^{j\phi}] + \frac{\gamma}{2j} [s(t)e^{j(2w_c t + \phi)} - s^*(t)e^{-j(2w_c t + \phi)}] \right\} \end{aligned} \quad (3.3)$$

where \mathcal{LPF}_I and \mathcal{LPF}_Q denote the low-pass filters for I and Q branches, respectively. The frequency response of \mathcal{LPF}_I and \mathcal{LPF}_Q are denoted as $G_I(f)$ and $G_Q(f)$ respectively. From (3.3), the frequency-domain I- and Q-branch signals after low-pass filtering are given respectively as

$$\begin{aligned} X_I(f) &= \frac{1}{2} G_I(f) [S(f) + S^*(-f)], \\ \text{and } X_Q(f) &= \frac{\gamma}{2j} G_Q(f) [S(f)e^{-j\phi} - S^*(-f)e^{j\phi}]. \end{aligned} \quad (3.4)$$

Then the received baseband signals $X(f)$ is

$$X(f) = \underbrace{\frac{G_I(f) + \gamma G_Q(f)e^{-j\phi}}{2}}_{G_1(f)} S(f) + \underbrace{\frac{G_I(f) - \gamma G_Q(f)e^{j\phi}}{2}}_{G_2(f)} S^*(-f). \quad (3.5)$$

*CHAPTER 3. BLIND FREQUENCY-DEPENDENT I/Q IMBALANCE
COMPENSATION FOR DIRECT-CONVERSION RECEIVERS*

Hence the time-domain down-converted signal is given by

$$x(t) = g_1(t) \otimes s(t) + g_2(t) \otimes s^*(t), \quad (3.6)$$

$$\text{with } g_1(t) = \frac{g_I(t) + \gamma g_Q(t)e^{-j\phi}}{2}, \quad \text{and } g_2(t) = \frac{g_I(t) - \gamma g_Q(t)e^{j\phi}}{2}. \quad (3.7)$$

It is seen that the I/Q imbalance causes the received baseband signal $s(t)$ distorted by its image signal $s^*(t)$. To evaluate the signal distortion caused by the I/Q imbalance, we define the analog front-end image-reject ratio (IRR) [Kiss and Prodanov, 2004] measured in decibels (dB) as

$$\text{IRR}(f) = 10 \log_{10} \frac{|G_1(f)|^2}{|G_2(f)|^2}. \quad (3.8)$$

After sampling $x(t)$ with a sampling interval T_s , the received discrete-time down-converted baseband signal becomes

$$x[n] = x(nT_s) = g_1[n] \otimes s[n] + g_2[n] \otimes s^*[n]. \quad (3.9)$$

3.2.2 Second-order Signal Statistics

The autocorrelation function (ACF) of a discrete-time complex random signal $x[n]$ is defined as $R_x[m] = \mathbb{E} \{x[n]x^*[n-m]\}$, where $\mathbb{E}\{\cdot\}$ denotes expectation. Another second-order statistic, the complementary autocorrelation function (CACF) is defined as $C_x[m] = \mathbb{E} \{x[n]x[n-m]\}$. A complex random signal $x[n]$ is proper if its CACF is equal to zero for all lag m [Neesser and Massey, 1993a], i.e., $C_x[m] = 0, \forall m$. In this paper, we assume that the transmitted data signal $d[n]$ is a zero-mean proper white process, i.e.,

$$R_d[m] = \mathbb{E} \{d[n]d^*[n-m]\} = \sigma_d^2 \delta[m], \quad (3.10)$$

$$C_d[m] = \mathbb{E} \{d[n]d[n-m]\} = 0, \forall m, \quad (3.11)$$

where $\delta[m]$ is the Dirac delta function. Let $s[n]$ be the received signals after the time-varying channel, i.e.,

$$s[n] = h[n, l] \otimes d[l] = \sum_l h[n, l]d[n-l]. \quad (3.12)$$

*CHAPTER 3. BLIND FREQUENCY-DEPENDENT I/Q IMBALANCE
COMPENSATION FOR DIRECT-CONVERSION RECEIVERS*

In this paper, we assume that the time-varying channel $h[n, l]$ is wide-sense stationary uncorrelated scattering (WSSUS), i.e., its ACF is expressed as [Hoeher, 1992]

$$\mathbb{E}\{h[n_1, l_1]h^*[n_2, l_2]\} = \beta(l_1)J_0(2\pi f_D T_s(n_1 - n_2))\delta[l_1 - l_2], \quad (3.13)$$

where $\beta(l_1)$ is a function of l_1 , f_D is the maximum Doppler shift, and $J_0(\cdot)$ is the zero-order Bessel function of the first kind. We next show that the received signal $s[n]$ in (3.12) remains white and proper. First, its ACF can be evaluated as

$$\begin{aligned} R_s[m] &= \sum_{l_1} \sum_{l_2} \mathbb{E}\{h(n, l_1)h^*(n-m, l_2)\} \mathbb{E}\{d[n-l_1]d^*[n-m-l_2]\} \\ &= \sigma_d^2 \sum_l \mathbb{E}\{h(n, m+l)h^*(n-m, l)\} = \underbrace{\sigma_d^2 \sum_l \beta(l)J_0(2\pi f_D T_s m)\delta[m]}_{\sigma_s^2} \end{aligned} \quad (3.14)$$

Moreover, the CACF of $s[n]$ is given by

$$C_s[m] = \sum_{l_1} \sum_{l_2} \mathbb{E}\{h(n, l_1)h(n-m, l_2)\} \underbrace{\mathbb{E}\{d[n-l_1]d[n-m-l_2]\}}_{C_d[m+l_2-l_1]=0} = 0, \quad (3.15)$$

3.3 Time-domain I/Q Imbalance Compensation

Assume that the filters $g_1[n]$ and $g_2[n]$ in (3.9) are approximated by FIR filters of length P and define $\mathbf{G}[p] = \begin{bmatrix} g_1[p] & g_2[p] \\ g_2^*[p] & g_1^*[p] \end{bmatrix}$, $p = 0, \dots, P-1$. Denote further $\mathbf{x}[n] = \begin{bmatrix} x[n] & x^*[n] \end{bmatrix}^T$ and $\mathbf{s}[n] = \begin{bmatrix} s[n] & s^*[n] \end{bmatrix}^T$. Then (3.9) can be rewritten in the form of the following conjugate signal model

$$\mathbf{x}[n] = \sum_{p=0}^{P-1} \mathbf{G}[p]\mathbf{s}[n-p]. \quad (3.16)$$

3.3.1 Identifiability

The objective of the I/Q imbalance compensation is to filter the signal $x[n]$ such that the output is a scaled and delayed version of $s[n]$ or $s^*[n]$. Mathematically, the goal

CHAPTER 3. BLIND FREQUENCY-DEPENDENT I/Q IMBALANCE
COMPENSATION FOR DIRECT-CONVERSION RECEIVERS

is to find a separation filter of length L of the following form

$$\mathbf{W}[l] = \begin{bmatrix} w_{11}[l] & w_{12}[l] \\ w_{12}^*[l] & w_{11}^*[l] \end{bmatrix}, \quad l = 0, 1, \dots, L-1, \quad (3.17)$$

such that the filter output $\mathbf{y}[n] = [y[n] \ y^*[n]]^T$ is given by

$$\mathbf{y}[n] = \sum_{l=0}^{L-1} \mathbf{W}[l] \mathbf{x}(n-l) = \lambda \mathbf{P} \mathbf{s}[n-n_0], \quad (3.18)$$

where \mathbf{P} is a permutation matrix, λ is a scaling factor, and n_0 is a delay.

We further define the following stacked signal model. Denote

$$\begin{aligned} \underline{\mathbf{y}}[n] &= [\mathbf{y}^T[n], \mathbf{y}^T[n-1], \dots, \mathbf{y}^T[n-M+1]]^T, \\ \underline{\mathbf{x}}[n] &= [\mathbf{x}^T[n], \mathbf{x}^T[n-1], \dots, \mathbf{x}^T[n-(M+L)+1]]^T, \\ \underline{\mathbf{W}} &= \begin{bmatrix} \mathbf{W}[0] & \mathbf{W}[1] & \dots & \mathbf{W}[L-1] & 0 & \dots & 0 \\ 0 & \mathbf{W}[0] & \mathbf{W}[1] & \dots & \mathbf{W}[L-1] & 0 & \ddots \\ 0 & 0 & \ddots & \ddots & \ddots & \ddots & \ddots \\ 0 & 0 & \ddots & \mathbf{W}[0] & \mathbf{W}[1] & \dots & \mathbf{W}[L-1] \end{bmatrix}, \end{aligned}$$

where $M \geq L-1$. Then we have

$$\underline{\mathbf{y}}[n] = \underline{\mathbf{W}} \underline{\mathbf{x}}[n]. \quad (3.19)$$

We have the following result on the identifiability for the I/Q imbalance problem.

Proposition 1. *We have $\mathbf{y}[n] = \lambda \mathbf{P} \mathbf{s}[n-n_0]$ if and only if $\mathbb{E} \{ \underline{\mathbf{y}}[n] \underline{\mathbf{y}}^H[n] \} = \kappa \mathbf{I}$, for some constant κ .*

Proof: We first show the necessary condition. Note that

$$\mathbb{E} \{ \underline{\mathbf{y}}[n] \underline{\mathbf{y}}^H[n] \} = \begin{bmatrix} \mathbf{R}_{\mathbf{y}}[0] & \mathbf{R}_{\mathbf{y}}[1] & \dots & \mathbf{R}_{\mathbf{y}}[M-1] \\ \mathbf{R}_{\mathbf{y}}[-1] & \mathbf{R}_{\mathbf{y}}[0] & \dots & \mathbf{R}_{\mathbf{y}}[M-2] \\ \vdots & \vdots & \ddots & \ddots \\ \mathbf{R}_{\mathbf{y}}[-(M-1)] & \mathbf{R}_{\mathbf{y}}[-(M-2)] & \dots & \mathbf{R}_{\mathbf{y}}[0] \end{bmatrix} = \kappa \mathbf{I}. \quad (3.20)$$

*CHAPTER 3. BLIND FREQUENCY-DEPENDENT I/Q IMBALANCE
COMPENSATION FOR DIRECT-CONVERSION RECEIVERS*

Moreover, since $\mathbf{y}[n] = [y[n] \ y^*[n]]^T$, we have

$$\mathbf{R}_y[m] = \begin{bmatrix} R_y[m] & C_y[m] \\ C_y^*[m] & R_y^*[m] \end{bmatrix}.$$

Then (3.20) implies the following:

$$C_y[m] \triangleq \mathbb{E} \{y[n]y[n-m]\} = 0, \quad \forall m, \quad (3.21)$$

$$\text{and } R_y[m] \triangleq \mathbb{E} \{y[n]y^*[n-m]\} = \kappa\delta[m]. \quad (3.22)$$

We can now proceed to show that if $y[n]$ satisfies (3.21)-(3.22) then $\mathbf{y}[n] = \lambda \mathbf{P}\mathbf{s}[n-\tau]$.

From (3.16) and (3.18), we can write

$$y[n] = f_1[n] \otimes s[n] + f_2[n] \otimes s^*[n], \quad (3.23)$$

where $f_1[n]$ and $f_2[n]$ are composite filters derived from $\{\mathbf{W}[l]\}$ and $\{\mathbf{G}[l]\}$. Substituting (3.23) into (3.21), and by using (3.14)-(3.15), we have

$$\begin{aligned} C_y[m] &= \sigma_s^2 \left(f_1[-m] \otimes f_2[m] + f_1[m] \otimes f_2[-m] \right) \\ &= \sigma_s^2 \left(h[-m] + h[m] \right) = 0, \end{aligned} \quad (3.24)$$

where $h[n] \triangleq f_1[n] \otimes f_2[-n]$. Note that (3.24) holds only when $h[n] = 0, \forall n$ or $h[n]$ is anti-symmetric and thus non-causal. We can exclude the later case for non-casual filters do not exist in practice. Hence, we can conclude that either $f_1[n] = 0$ or $f_2[n] = 0$. Let us first assume $f_2[n] = 0$. Then $y[n]$ in (3.23) becomes

$$y[n] = f_1[n] \otimes s[n]. \quad (3.25)$$

Substituting (3.25) into (3.22), we obtain

$$R_y[m] = \sigma_s^2 (f_1^*[-m] \otimes f_1[m]) = \kappa\delta[m]. \quad (3.26)$$

Now taking the Fourier transform of $f_1^*[-m] \otimes f_1[m]$ we have $\|F_1(\omega)\|^2 = \frac{\kappa}{\sigma_s^2}$, which means $f_1[n]$ is an all-pass filter. Since $f_1[n]$ is an FIR filter, we must have $f_1[n] =$

*CHAPTER 3. BLIND FREQUENCY-DEPENDENT I/Q IMBALANCE
COMPENSATION FOR DIRECT-CONVERSION RECEIVERS*

$\lambda_1 \delta[n - n_1]$ for some delay n_1 and some scaling λ_1 . Hence $y[n] = \lambda_1 s[n - n_1]$ or equivalently $\mathbf{y}[n] = \lambda_1 \cdot \mathbf{I} \cdot \mathbf{s}[n - n_1]$.

Similarly, if $f_1[n] = 0$ then we will have $y[n] = \lambda_2 s^*[n - n_2]$ or equivalently $\mathbf{y}[n] = \lambda_2 \cdot \mathbf{J} \cdot \mathbf{s}[n - n_2]$, where $\mathbf{J} \triangleq \begin{bmatrix} 0 & 1 \\ 1 & 0 \end{bmatrix}$.

Now we proceed to prove the sufficiency. If $\mathbf{y}[n] = \lambda \mathbf{P} \mathbf{s}[n - n_0]$, then (3.20) becomes

$$\mathbb{E} \{ \underline{\mathbf{y}}[n] \underline{\mathbf{y}}[n]^H \} = \lambda^2 \begin{bmatrix} \mathbf{P} \mathbf{R}_s[0] \mathbf{P} & \mathbf{P} \mathbf{R}_s[1] \mathbf{P} & \cdots & \mathbf{P} \mathbf{R}_s[M-1] \mathbf{P} \\ \mathbf{P} \mathbf{R}_s[-1] \mathbf{P} & \mathbf{P} \mathbf{R}_s[0] \mathbf{P} & \cdots & \mathbf{P} \mathbf{R}_s[M-2] \mathbf{P} \\ \vdots & & \ddots & \\ \mathbf{P} \mathbf{R}_s[-M+1] \mathbf{P} & \cdots & \cdots & \mathbf{P} \mathbf{R}_s[0] \mathbf{P} \end{bmatrix} \quad (3.27)$$

Since $s[n]$ is white and proper, we have $\mathbf{R}_s[m] = \sigma_s^2 \delta[m] \mathbf{I}$. Therefore, (3.27) is a diagonal matrix. \square

Remark: The output of the blind I/Q imbalance compensation filter is a delayed and scaled version of $s[n]$ or $s^*[n]$, which can be resolved as follow. For the delay estimation, many synchronization techniques can be used [Negi and Cioffi, 2002]. The scale ambiguity can be lumped into the effective channel gain and can be removed by channel estimation. As for resolving the ambiguity of conjugation, cyclic redundancy check (CRC) which is common in modern commercial wireless communication systems can be used.

3.3.2 Blind I/Q Imbalance Compensation Algorithm

In order to obtain the I/Q imbalance compensation filter $\mathbf{W}[l]$, based on Proposition 1, we define the following cost function by setting $\kappa = 1$

$$c(\{\mathbf{W}[l]\}) \triangleq \left\| \mathbf{R}_y - \mathbf{I} \right\|_F^2. \quad (3.28)$$

We can then obtain $\{\mathbf{W}[l]\}$ by minimizing the above cost function, i.e.,

$$\{\mathbf{W}^{\text{opt}}[l]\} = \min_{\{\mathbf{W}[l]\}} c(\{\mathbf{W}[l]\}). \quad (3.29)$$

CHAPTER 3. BLIND FREQUENCY-DEPENDENT I/Q IMBALANCE
COMPENSATION FOR DIRECT-CONVERSION RECEIVERS

We will use the gradient descent search method [Haykin, 1996] to solve (3.29). In

what follows we denote the (i, j) -th 2×2 submatrix of a matrix \mathbf{A} as $[\mathbf{A}]_{ij} \triangleq \begin{bmatrix} a_{2(i-1)+1, 2(j-1)+1} & a_{2(i-1)+1, 2(j-1)+2} \\ a_{2(i-1)+2, 2(j-1)+1} & a_{2(i-1)+2, 2(j-1)+2} \end{bmatrix}$. Using the identity

$$\|\mathbf{A}\|_F^2 = \text{tr}(\mathbf{A}\mathbf{A}^H) = \sum_i \text{tr}([\mathbf{A}\mathbf{A}^H]_{ii}) = \sum_i \sum_l \text{tr}([\mathbf{A}]_{il}[\mathbf{A}^H]_{li}),$$

(3.28) can be expressed as

$$c(\{\mathbf{W}[l]\}) = \sum_{i=1}^L \sum_{j \neq i}^L \text{tr}([\mathbf{R}_{\mathbf{y}}]_{ij}[\mathbf{R}_{\mathbf{y}}]_{ij}^H) + \sum_{i=1}^L \text{tr}\left(\left([\mathbf{R}_{\mathbf{y}}]_{ii} - \mathbf{I}\right)\left([\mathbf{R}_{\mathbf{y}}]_{ii} - \mathbf{I}\right)^H\right), \quad (3.30)$$

$$\text{with } [\mathbf{R}_{\mathbf{y}}]_{ij} = [\mathbf{W}\mathbb{E}\{\mathbf{x}\mathbf{x}^H\}\mathbf{W}^H]_{ij}, \quad (3.31)$$

$$\text{and } \mathbb{E}\{\mathbf{x}\mathbf{x}^H\} = \begin{bmatrix} \mathbf{R}_{\mathbf{x}}[0] & \mathbf{R}_{\mathbf{x}}[1] & \dots & \mathbf{R}_{\mathbf{x}}[M+P-1] \\ \mathbf{R}_{\mathbf{x}}[-1] & \mathbf{R}_{\mathbf{x}}[0] & \dots & \mathbf{R}_{\mathbf{x}}[M+P-2] \\ \vdots & \vdots & \ddots & \ddots \\ \mathbf{R}_{\mathbf{x}}[-(M+P-1)] & \mathbf{R}_{\mathbf{x}}[-(M+P-2)] & \dots & \mathbf{R}_{\mathbf{x}}[0] \end{bmatrix}. \quad (3.32)$$

Using (3.31) the term $\text{tr}([\mathbf{R}_{\mathbf{y}}]_{ij}[\mathbf{R}_{\mathbf{y}}]_{ij}^H)$ in (3.30) is equal to

$$\begin{aligned} & \text{tr}([\mathbf{R}_{\mathbf{y}}]_{ij}[\mathbf{R}_{\mathbf{y}}]_{ij}^H) \\ &= \text{tr}([\mathbf{W}\mathbf{R}_{\mathbf{x}}\mathbf{W}^H\mathbf{W}\mathbf{R}_{\mathbf{x}}^H\mathbf{W}^H]_{ij}) \\ &= \text{tr}\left(\sum_{k_1=j}^{j+L-1} \sum_{k_2=j}^{j+L-1} \sum_{l_1=i}^{i+L-1} \sum_{l_2=i}^{i+L-1} [\mathbf{W}]_{il_1}[\mathbf{R}_{\mathbf{x}}]_{l_1k_1}[\mathbf{W}^H]_{k_1j}[\mathbf{W}]_{k_2j}[\mathbf{R}_{\mathbf{x}}^H]_{l_2k_2}[\mathbf{W}^H]_{il_2}\right) \end{aligned} \quad (3.33)$$

Similarly, the term $\text{tr}\left(\left([\mathbf{R}_{\mathbf{y}}]_{ii} - \mathbf{I}\right)\left([\mathbf{R}_{\mathbf{y}}]_{ii} - \mathbf{I}\right)^H\right)$ in (3.30) is expressed as

$$\begin{aligned} & \text{tr}\left(\left([\mathbf{R}_{\mathbf{y}}]_{ii} - \mathbf{I}\right)\left([\mathbf{R}_{\mathbf{y}}]_{ii} - \mathbf{I}\right)^H\right) \\ &= \text{tr}\left(\sum_{k_1=j}^{j+L-1} \sum_{k_2=j}^{j+L-1} \sum_{l_1=i}^{i+L-1} \sum_{l_2=i}^{i+L-1} [\mathbf{W}]_{il_1}[\mathbf{R}_{\mathbf{x}}]_{l_1k_1}[\mathbf{W}^H]_{k_1i}[\mathbf{W}]_{k_2i}[\mathbf{R}_{\mathbf{x}}^H]_{l_2k_2}[\mathbf{W}^H]_{il_2}\right) \\ & \quad - \text{tr}\left(\sum_{k=j}^{j+L-1} \sum_{l=i}^{i+L-1} [\mathbf{W}]_{il}[\mathbf{R}_{\mathbf{x}}]_{lk}[\mathbf{W}^H]_{ki}\right) \\ & \quad - \text{tr}\left(\sum_{k=j}^{j+L-1} \sum_{l=i}^{i+L-1} [\mathbf{W}]_{ki}[\mathbf{R}_{\mathbf{x}}]_{lk}[\mathbf{W}^H]_{il}\right) + \mathbf{I}. \end{aligned} \quad (3.34)$$

*CHAPTER 3. BLIND FREQUENCY-DEPENDENT I/Q IMBALANCE
COMPENSATION FOR DIRECT-CONVERSION RECEIVERS*

The following gradient descent iteration can be employed to solve (3.29) [Haykin, 1996; ?],

$$\mathbf{W}[m]^{(k+1)} = \mathbf{W}[m]^{(k)} - \mu \left(\frac{\partial c(\{\mathbf{W}[l]\})}{\partial \mathbf{W}^*[m]^{(k)}} \right) \quad (3.35)$$

where $\mathbf{W}[m]^{(k)}$ is the m -th tap matrix of the I/Q imbalance filter at the k -th iteration, and μ is the learning rate.

From (3.33)-(3.34), it is seen that the cost function (3.30) is composed of terms in the forms of $\mathbf{W}[i]\mathbf{A}\mathbf{W}^H[j]\mathbf{W}[k]\mathbf{B}\mathbf{W}^H[l]$ and $\mathbf{W}[i]\mathbf{A}\mathbf{W}^H[j]$, where \mathbf{A} and \mathbf{B} are 2×2 submatrices from $\mathbf{R}_{\mathbf{x}}$. For example, when $i = 2, j = 2, k_1 = k_2 = 2, l_1 = l_2 = 2$, one of the terms in (3.34) is $[\mathbf{W}]_{22} [\mathbf{R}_{\mathbf{x}}]_{22} [\mathbf{W}^H]_{22} [\mathbf{W}]_{22} [\mathbf{R}_{\mathbf{x}}^H]_{22} [\mathbf{W}^H]_{22} = \mathbf{W}[0]\mathbf{R}_{\mathbf{x}}[0]\mathbf{W}^H[1]\mathbf{W}[0]\mathbf{R}_{\mathbf{x}}^H[0]\mathbf{W}^H[1]$.

Define $\delta_{i,m} = 1$, if $i = m$ and 0 otherwise. Define further a matrix transformation operator $\mathfrak{T}(\mathbf{B}) = \mathfrak{T} \left(\begin{bmatrix} b_{11} & b_{12} \\ b_{21} & b_{22} \end{bmatrix} \right) \triangleq \begin{bmatrix} b_{22} & b_{12} \\ b_{21} & b_{11} \end{bmatrix}$. Then the gradient in (3.35) consists of the following terms (see Appendix A for derivations)

$$\begin{aligned} & \frac{\partial}{\partial \mathbf{W}^*[m]} \text{tr} (\mathbf{W}[i]\mathbf{A}\mathbf{W}^H[j]\mathbf{W}[k]\mathbf{B}\mathbf{W}^H[l]) \\ &= \delta_{i,m} \mathfrak{T} (\mathbf{A}\mathbf{W}^H[j]\mathbf{W}[k]\mathbf{B}\mathbf{W}^H[l]) + \delta_{j,m} \mathbf{W}[k]\mathbf{B}\mathbf{W}^H[l]\mathbf{W}[i]\mathbf{A} \\ &+ \delta_{k,m} \mathfrak{T} (\mathbf{B}\mathbf{W}^H[l]\mathbf{W}[i]\mathbf{A}\mathbf{W}^H[j]) + \delta_{l,m} \mathbf{W}[i]\mathbf{A}\mathbf{W}^H[j]\mathbf{W}[k]\mathbf{B}, \end{aligned} \quad (3.36)$$

$$\begin{aligned} \text{and } & \frac{\partial}{\partial \mathbf{W}^*[m]} \text{tr} (\mathbf{W}[i]\mathbf{A}\mathbf{W}^H[j]) \\ &= \delta_{i,m} \mathfrak{T} (\mathbf{A}\mathbf{W}^H[j]) + \delta_{j,m} \mathbf{W}[i]\mathbf{A}. \end{aligned} \quad (3.37)$$

Note that the matrices \mathbf{A} and \mathbf{B} in (3.36)-(3.37) correspond to the autocorrelation matrix of $\mathbf{x}[n]$, i.e., $\mathbf{R}_{\mathbf{x}}[m] = \mathbb{E}\{\mathbf{x}[n]\mathbf{x}^H[n-m]\}$, and they are estimated using the time-average of the signal samples $\mathbf{x}[n]$.

3.4 I/Q Imbalance Compensation for OFDM Systems

In this section, we consider blind I/Q imbalance compensation in OFDM systems. For an OFDM system with N subcarriers, (3.5) becomes

$$X[k] = G_1[k]S[k] + G_2[k]S^*[-k], \quad k = -N, \dots, 0 \dots N. \quad (3.38)$$

In (3.38) $S[k] = H[k]D[k]$ where $H[k]$ and $D[k]$ are the channel frequency response and the transmitted symbol at the k -th subcarrier, respectively. As before, we assume the channel satisfies the WSSUS property and the data symbols $D[k]$ are zero-mean and uncorrelated. Then the received signals satisfy $\mathbb{E}\{S[k]S^*[k]\} = \sigma_s^2$ and $\mathbb{E}\{S[k]S[-k]\} = 0$. It is seen that the I/Q imbalance causes the signal at k -th subcarrier corrupted by that at the $-k$ -th subcarrier. Using (3.5), we can write

$$G_1[k] = \frac{G_I[k]}{2} (1 + G_d[k]e^{-j\phi}), \quad (3.39)$$

$$\text{and } G_2[k] = \frac{G_I[k]}{2} (1 - G_d[k]e^{j\phi}), \quad (3.40)$$

where $G_d[k] \triangleq \gamma G_Q[k]/G_I[k]$. Then using (3.38) we have

$$\begin{aligned} \begin{bmatrix} X[k] \\ X^*[-k] \end{bmatrix} &= \underbrace{\begin{bmatrix} 1 + G_d[k]e^{-j\phi} & 1 - G_d[k]e^{j\phi} \\ 1 - G_d^*[-k]e^{-j\phi} & 1 + G_d^*[-k]e^{j\phi} \end{bmatrix}}_{\mathbf{G}[k]} \\ &\quad \begin{bmatrix} \frac{1}{2}G_I[k]H[k] \\ \frac{1}{2}G_I^*[-k]H^*[-k] \end{bmatrix} \begin{bmatrix} D[k] \\ D^*[-k] \end{bmatrix}. \end{aligned} \quad (3.41)$$

In (3.41) we have used the factor that since the low pass filter $g_I[n]$ has real impulse response, therefore, $G_I[k] = G_I^*[-k]$. It is seen from (3.41) that the common factor $G_I[k]$ in $G_1[k]$ and $G_2[k]$ can be absorbed into the channel. Hence the effect of the I/Q imbalance is equivalent to a one-tap (vector) channel model and if an estimate of the tap matrix $\mathbf{G}[k]$ is available, then the I/Q imbalance can be compensated for by simply inverting $\mathbf{G}[k]$.

CHAPTER 3. BLIND FREQUENCY-DEPENDENT I/Q IMBALANCE
COMPENSATION FOR DIRECT-CONVERSION RECEIVERS

In order to estimate $\mathbf{G}[k]$ in (3.41), we need to estimate $G_d[k]$ and ϕ . Writing $G_d[k]$ in the polar form, i.e., $G_d[k] = \alpha[k]e^{j\beta[k]}$, then we have the following estimators for $\alpha[k]$, $\beta[k]$, whose derivations are given in Appendix B.

$$\hat{\alpha}[k] = \sqrt{\frac{\mathbb{E}\{|X[k] - X^*[-k]|^2\}}{\mathbb{E}\{|X[k] + X^*[-k]|^2\}}}, \quad (3.42)$$

$$\text{and } \hat{\beta}[k] = \arctan \left\{ -\frac{\mathbb{E}\{|X[k]|^2 - |X[-k]|^2\}}{2\mathcal{Im}\{\mathbb{E}\{X[k]X[-k]\}\}} \right\}. \quad (3.43)$$

The phase mismatch ϕ can be estimated at each subcarrier by

$$\hat{\phi}[k] = \frac{\mathbb{E}\{|X[k] - X^*[-k]|^2\}}{\mathbb{E}\{|X[k] + X^*[-k]|^2\} \mathcal{Im}\{G_d[k]\}}. \quad (3.44)$$

The final estimate of ϕ is then given by the average over all subcarriers, i.e., $\hat{\phi} = \frac{1}{N} \sum_{k=-N}^N \hat{\phi}[k]$.

In practice, the expectation operator $\mathbb{E}\{\cdot\}$ in (3.42)-(3.44) is replaced by a time-average operation over OFDM symbols. For example, suppose we collect U OFDM symbols $\{X[k, t], k = -N, \dots, N; t = 1, \dots, U\}$. Then $\mathbb{E}\{|X[k]|^2\} \cong \frac{1}{U} \sum_{t=1}^U |X[k, t]|^2$. In practice, the frequency-selectivity is not severe. Therefore we assume the second-order statistics in (3.42)-(3.44) are approximately equal over some consecutive subcarriers. Hence we group K subcarriers when computing the average, i.e., $\mathbb{E}\{|X[k_0]|^2\} \cong \frac{1}{KT} \sum_{k=k_0-K/2}^{k_0+K/2-1} \sum_{t=1}^U |X[k, t]|^2$. By such grouping in the frequency domain, we can reduce the number of OFDM symbols used for averaging and thus reduce the estimation latency. In this way, we can estimate the parameters $\{\alpha[k], \beta[k], k = K, 2K, 3K, \dots\}$. Then the parameters corresponding to other subcarriers can be obtained using interpolations. In particular, in our implementations, a cubic spline interpolation [Press *et al.*, 1992] is used to estimate $\alpha[k]$, and a second-order polynomial interpolation is used to obtain smoother estimates of the phase terms $\beta[k]$.

3.5 Simulation Results

In this section we present simulation results to demonstrate the performance of the proposed time-domain and frequency-domain blind I/Q imbalance compensation algorithms

3.5.1 Simulation Setup

We have simulated an LTE OFDM system [Thr, 2008] with the following system parameters: $N = 1024$ subcarriers, guard interval $N_{cp} = 72$, subcarrier spacing $\Delta f = 15\text{kHz}$, sampling interval $T_s = 0.651\mu\text{s}$ and therefore the OFDM symbol duration is $T = NT_s = 0.67\text{ms}$. The time-varying channel is assumed to be WSSUS and is modeled as a tapped delay line model with exponential delay power profile [Bello, 1963]. The length of the mobile channel is $L_h = 32$ and the exponential decay parameter $\psi = 0.1$ is defined as the amplitude variance of the last path assuming the first path has unit variance. The channel is then normalized to have unit power. The Doppler spectrum is assumed to follow Jake's model [Jakes, 1974] and a normalized maximum Doppler shift $f_D T = 0.22$ is used in the simulations. Since our focus is on the performance of the proposed I/Q imbalance compensation algorithms, the channel is assumed to be perfectly known.

In the simulation, we consider two different sets of I/Q imbalance parameters. Each of the imbalance filters $g_I[n]$ and $g_Q[n]$ is split into two filters (Fig. 3.1 (b)), one is the desired low pass filters $g_{nom}[n]$ and the others are $g'_I[n]$ and $g'_Q[n]$, the filters that captures the non-ideal characteristics introduced during the manufacture [Kiss and Prodanov, 2004]. In practice, the non-ideal characteristics is not serve, therefore, the taps length of $g'_I[n]$ and $g'_Q[n]$ is short. Note that since what matters is the mismatched response $g_{mis}[n] = \text{IDFT}\{\frac{G_I(e^{jw})}{G_Q(e^{jw})}\} = \text{IDFT}\{\frac{G'_I(e^{jw})}{G'_Q(e^{jw})}\}$ [Xing *et al.*, 2005]. Therefore, in the simulation, we only model $g'_I[n]$ and $g'_Q[n]$. In the following, we omit $(')$ in $g'_I[n]$ and $g'_Q[n]$ for simplicity.

CHAPTER 3. BLIND FREQUENCY-DEPENDENT I/Q IMBALANCE COMPENSATION FOR DIRECT-CONVERSION RECEIVERS

Case 1: The gain mismatch and phase mismatch in (3.2) are $\gamma = 1.03$ and $\phi = 3^\circ$, respectively; and the I- and Q-branch LPFs are $g_I(z) = 0.01 + z^{-1} + 0.01z^{-2}$ and $g_Q(z) = 0.01 + z^{-1} + 0.2z^{-2}$, respectively [Valkama *et al.*, 2001]. In this case, the uncompensated $\text{IRR}(f) = 10 \log_{10} \frac{|G_1(f)|^2}{|G_2(f)|^2}$ is approximate 20dB (Fig. 3.3 (a)). Based on these parameters, the 3-taps convolutive mixture matrices in (3.16) are

$$\mathbf{G}[0] = \begin{bmatrix} 0.0101 - 0.0003i & -0.0001 - 0.0003i \\ -0.0001 + 0.0003i & 0.0101 + 0.0003i \end{bmatrix}, \mathbf{G}[1] = \begin{bmatrix} 1.0143 - 0.0270i & -0.0143 - 0.0270i \\ -0.0143 + 0.0270i & 1.0143 - 0.0270i \end{bmatrix},$$

$$\mathbf{G}[2] = \begin{bmatrix} 0.1079 - 0.0054i & -0.0979 - 0.0054i \\ -0.0979 + 0.0054i & 0.1079 - 0.0054i \end{bmatrix}.$$

Case 2: The gain mismatch and phase mismatch the same as before. But the I- and Q-branch LPFs are $g_I(z) = 0.98 + 0.03z^{-1}$ and $g_Q(z) = 1.0 - 0.005z^{-1}$, respectively [Anttila *et al.*, 2007]. The 2-taps convolutive mixture matrices in (3.16) are $\mathbf{G}[0] =$

$$\begin{bmatrix} 1.0043 - 0.0270i & -0.0243 - 0.0270i \\ -0.0243 + 0.0270i & 1.0043 + 0.0270i \end{bmatrix}, \mathbf{G}[1] = \begin{bmatrix} 0.0124 + 0.0001i & 0.0176 + 0.0001i \\ 0.0176 - 0.0001i & 0.0124 - 0.0001i \end{bmatrix}.$$

In both cases, the modulation is 64-QAM and the received SNR is 25dB.

3.5.2 Performance of Time-domain Blind Compensation Algorithm

The performance of the proposed time-domain blind I/Q imbalance compensation algorithm is presented in this subsection for the OFDM system described above. However, note that this method can be applied to other non-OFDM systems as well. We set $\mu = 0.001$ in (3.35). For **Case 1** the compensation filter length is $L = 3$ and the initial values are $\mathbf{w}_{[0]} = \begin{bmatrix} 1 & 0 \\ 0 & 1 \end{bmatrix}$, $\mathbf{w}_{[1]} = \begin{bmatrix} 0 & 0 \\ 0 & 0 \end{bmatrix}$ and $\mathbf{w}_{[2]} = \begin{bmatrix} 0 & 0 \\ 0 & 0 \end{bmatrix}$. For **Case 2** the compensation filter length is $L = 2$ and the initial values are $\mathbf{w}_{[0]} = \begin{bmatrix} 1 & 0 \\ 0 & 1 \end{bmatrix}$ and $\mathbf{w}_{[1]} = \begin{bmatrix} 0 & 0 \\ 0 & 0 \end{bmatrix}$. The above choices of the initial taps are justified by the fact that the LPFs on the I- and Q- branches are both close to ideal, i.e, their impulse responses are close to $\delta(z)$. In practice, the gradient descent procedure (3.35) is stopped when the norm of gradient is below a certain threshold or the number of iterations exceeds a certain value. Here the threshold is set to be 0.0005 and maximum number of iterations is 3000. In Fig. 3.2, the norm of the gradient, $\sum_m \|\Delta \mathbf{W}[m]^{(k)}\|_F$ is plotted against the number of iterations k . It is seen that the proposed time-domain algorithm takes about 1500

*CHAPTER 3. BLIND FREQUENCY-DEPENDENT I/Q IMBALANCE
COMPENSATION FOR DIRECT-CONVERSION RECEIVERS*

iterations to converge for **Case 1** and 1200 iterations for **Case 2**. This is because **Case 1** has more severe I/Q imbalance. We also compare our proposed time-domain algorithm with the following adaptive algorithm proposed in [Anttila *et al.*, 2008].

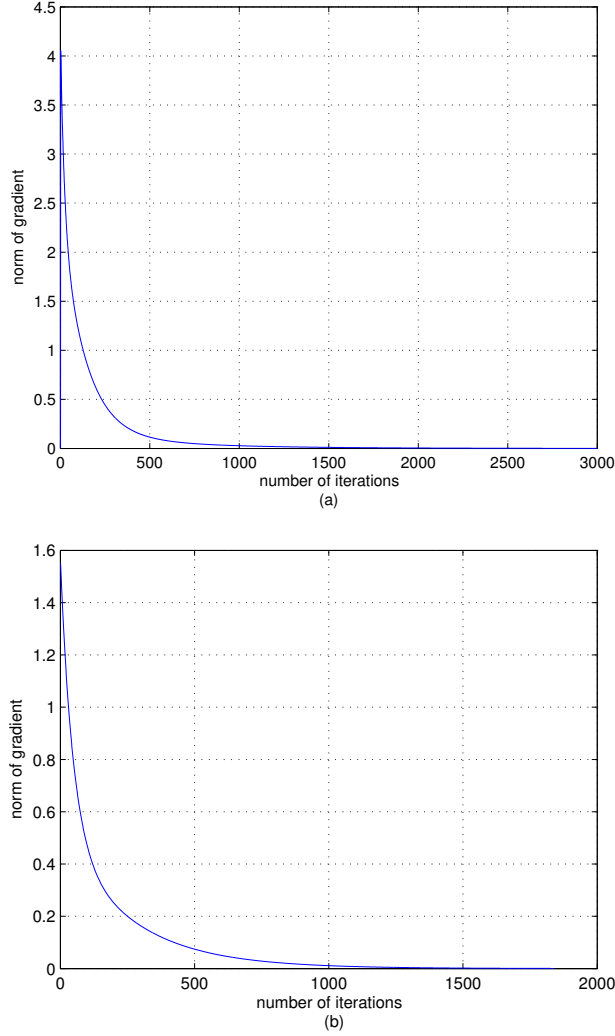


Figure 3.2: Convergence of the proposed time-domain blind I/Q imbalance compensation method. (a) **Case 1**. (b) **Case 2**.

$$\begin{aligned}
 y[n] &= x[n] + \tilde{\mathbf{w}}_n^T \mathbf{x}^*[n], \\
 \mathbf{w}_{n+1} &= \mathbf{w}_n - \lambda \odot \mathbf{y}[n]y[n], \\
 \tilde{\mathbf{w}}_{n+1} &= \alpha \tilde{\mathbf{w}}_n + (1 - \alpha) \mathbf{w}_{n+1},
 \end{aligned} \tag{3.45}$$

CHAPTER 3. BLIND FREQUENCY-DEPENDENT I/Q IMBALANCE
COMPENSATION FOR DIRECT-CONVERSION RECEIVERS

where $\mathbf{w}_n = [w_1[n], w_2[n], \dots, w_L[n]]^T$ denotes the L -tap compensator at time n ; $\mathbf{x}[n] = [x[n], x[n-1], \dots, x[n-L+1]]^T$ contains the received signal samples (3.9); $\mathbf{y}[n] = [y[n], y[n-1], \dots, y[n-L+1]]^T$; $\boldsymbol{\lambda}$ contains the step-sizes for all taps and \odot denotes the element-wise product; α is a smoothing factor. The length of compensated filter L is set to the same as our proposed method. As in [Anttila *et al.*, 2008], the step-sizes are set as $\boldsymbol{\lambda} = 10^{-4}[1, 0.5, 0.5]^T$ for **Case 1** and $\boldsymbol{\lambda} = 10^{-4}[1, 0.5]^T$ for **Case 2**; and the smoothing parameter $\alpha = 0.999$. Note that our method performs block processing and the algorithm in [Anttila *et al.*, 2008] is a sequential LMS-type approach. The algorithm in [Anttila *et al.*, 2008] is based on the second-order statistics obtained by only using one time sample and the cost function has larger variation. Hence, it is difficult to decide when to terminate the iteration. Although the optimal step size and smoothing parameter suggested in [Anttila *et al.*, 2008] are used in the simulation for performance evaluation, the convergence of the method [Anttila *et al.*, 2008] is still varying between 100 to 50000 samples. In order to compare, we used the same number of samples for both methods, i.e., 20000 time-domain samples (about 20 OFDM symbols) are used for **Case 1** and 10000 samples (about 10 OFDM symbols) for **Case 2** for each experiment. Thus the latency of both algorithms are identical. The reason that **Case 1** uses more samples is again due to its more severe I/Q imbalance. Fig. 3.3(a) and 3.4(a) show the IRR performance defined in (3.8) for both methods, obtained by averaging individual IRR of 100 experiments. For the proposed time-domain method, the IRR can be computed as follow. From (3.16) and (3.18), $y[n] = c_1[n] \otimes s[n] + c_2[n] \otimes s^*[n]$ where $c_1[n] = w_{11}[n] \otimes g_1[n] + w_{12}[n] \otimes g_2^*[n]$ and $c_2[n] = w_{11}[n] \otimes g_2[n] + w_{12}[n] \otimes g_1^*[n]$. Therefore, $\text{IRR}(f) = 10 \log_{10} \frac{|C_1(f)|^2}{|C_2(f)|^2}$ where $C_i(f)$ is the frequency response of $c_i[n]$. Similarly, the IRR of the method in [Anttila *et al.*, 2008] can be computed as $\text{IRR}(f) = 10 \log_{10} \frac{|Q_1(f)|^2}{|Q_2(f)|^2}$, where $q_1[n] = g_1[n] + g_2^*[n] \otimes w[n]$, and $q_2[n] = g_2[n] + g_1^*[n] \otimes w[n]$. It is seen that the IRR is improved by around 20-25dB by the proposed I/Q imbalance compensation method. Compared with the

*CHAPTER 3. BLIND FREQUENCY-DEPENDENT I/Q IMBALANCE
COMPENSATION FOR DIRECT-CONVERSION RECEIVERS*

method in [Anttila *et al.*, 2008], our proposed algorithm offers approximately 10dB gain for **Case 1** and a few dB gain for **Case 2**. Therefore, the proposed time-domain method is shown to have better and more stable performance at the cost of higher complexity. The computation complexity in (3.35) requires $(2L)^7$ of 2×2 matrix multiplication and L^4 of 2×2 matrix addition for each coefficient update, where L is the compensation filter length. Fig. 3.3(b) and 3.4(b) show the symbol error rate (SER) performance using 64-QAM modulation for both methods. Again it is seen that the proposed method can more effectively remove the impairment caused by the I/Q imbalance.

3.5.3 Performance of Frequency-domain Blind Compensation Algorithm

We now consider the performance of the frequency-domain blind I/Q imbalance compensation method for OFDM systems developed in Section 3.4. Recall that when computing the second-order moments that are needed for parameter estimation, we make use of a group of K consecutive subcarriers and U OFDM symbols. In the simulations, we fixed the total number samples for average, i.e., $KU = 30000$. Since in the frequency-domain approach, each subcarrier has its own one-tap compensation filter, and there is only one sample at each subcarrier in each OFDM symbol, the estimation latency is higher compared with the time-domain approach in terms of number of samples. However, the advantages of the frequency-domain method include 1) when only certain frequency bands are of interest, we can just compute the corresponding compensation filters; and 2) the compensation filters are in closed-form and involve no iterations. Note that $K = 1$ corresponds to no subcarrier grouping for which case interpolation is still applied to smooth the estimates. In Fig. 3.5 and 3.6, we show the SER performance comparisons among different choices of the subcarrier grouping parameter K . It is seen that for $K = 2, 4, 8$ the performance is the same. For $K = 16$, a performance loss is seen around $\text{SER} = 10^{-3}$. This is because the I/Q

*CHAPTER 3. BLIND FREQUENCY-DEPENDENT I/Q IMBALANCE
COMPENSATION FOR DIRECT-CONVERSION RECEIVERS*

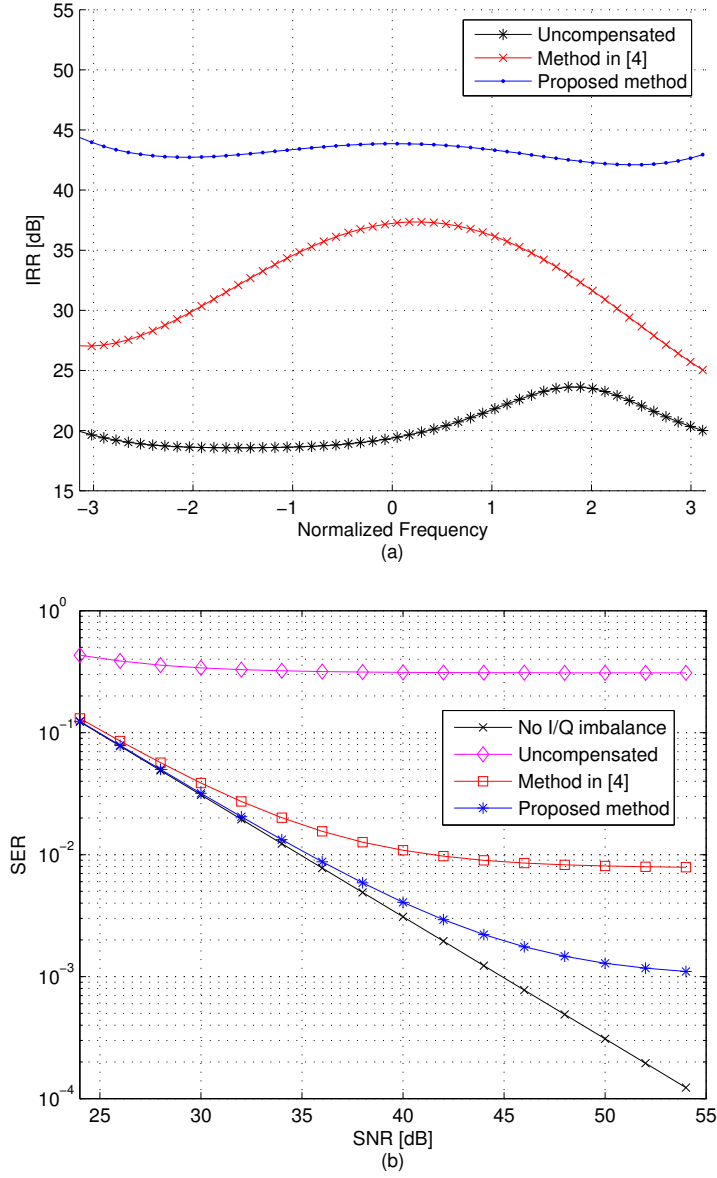


Figure 3.3: The IRR and SER performance of the proposed time-domain blind I/Q imbalance compensation method for Case 1. (a) IRR performance. (b) SER performance.

*CHAPTER 3. BLIND FREQUENCY-DEPENDENT I/Q IMBALANCE
COMPENSATION FOR DIRECT-CONVERSION RECEIVERS*

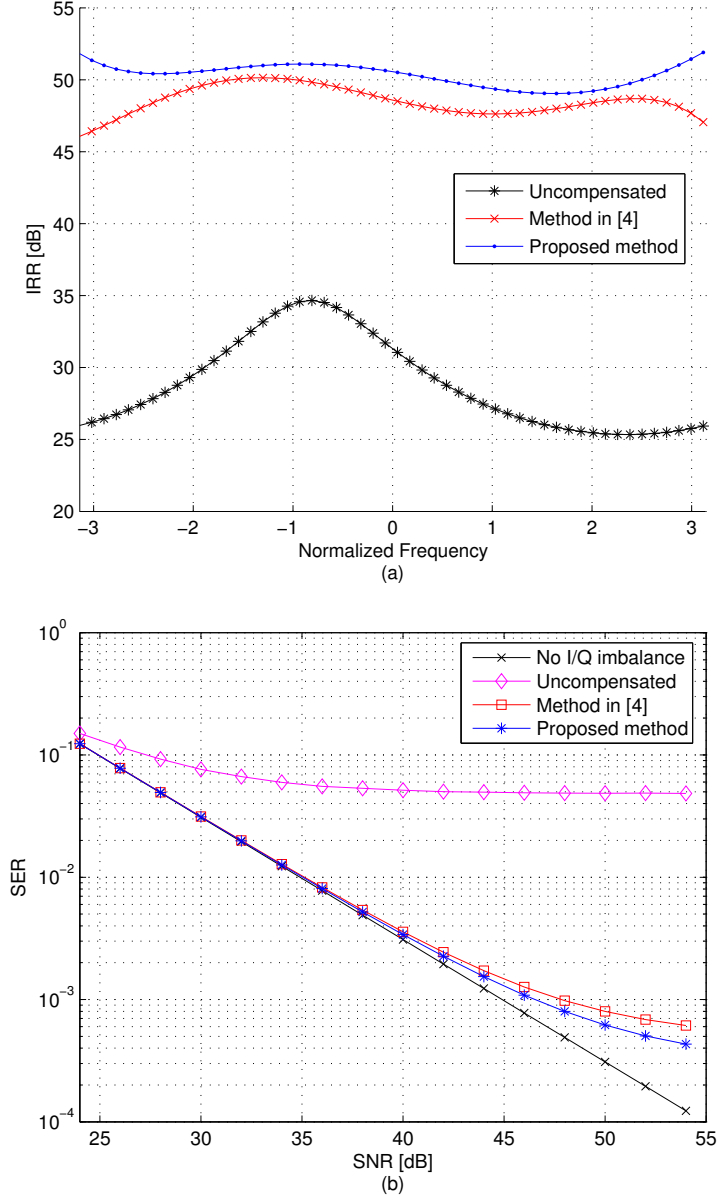


Figure 3.4: The IRR and SER performance of the proposed time-domain blind I/Q imbalance compensation method for Case 2. (a) IRR performance. (b) SER performance.

CHAPTER 3. BLIND FREQUENCY-DEPENDENT I/Q IMBALANCE COMPENSATION FOR DIRECT-CONVERSION RECEIVERS

imbalance parameters can no longer be considered constant when the group size K is too large. Therefore there is a trade-off between the system performance and the processing latency. For both cases, $K = 8$ is a good choice for reducing the latency while still maintaining the good performance.

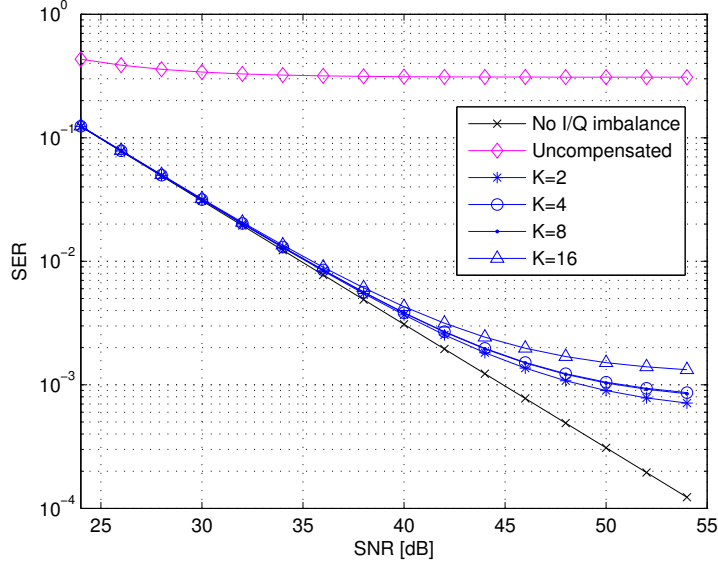


Figure 3.5: The SER performance of the proposed frequency-domain blind I/Q imbalance compensation method for OFDM systems for **Case 1**.

3.6 Conclusions

We have proposed two blind approaches to compensating the frequency-dependent I/Q imbalance for wideband direct-conversion receivers. One is a time-domain method for general systems and the other is a frequency-domain method that is specifically for OFDM systems. For the time-domain method, a blind identifiability condition is given based on which a cost function for compensating the I/Q imbalance is proposed; and a gradient-descent algorithm is derived to obtain the compensating filter. For the frequency-domain method, we have developed estimators for the frequency-dependent

*CHAPTER 3. BLIND FREQUENCY-DEPENDENT I/Q IMBALANCE
COMPENSATION FOR DIRECT-CONVERSION RECEIVERS*

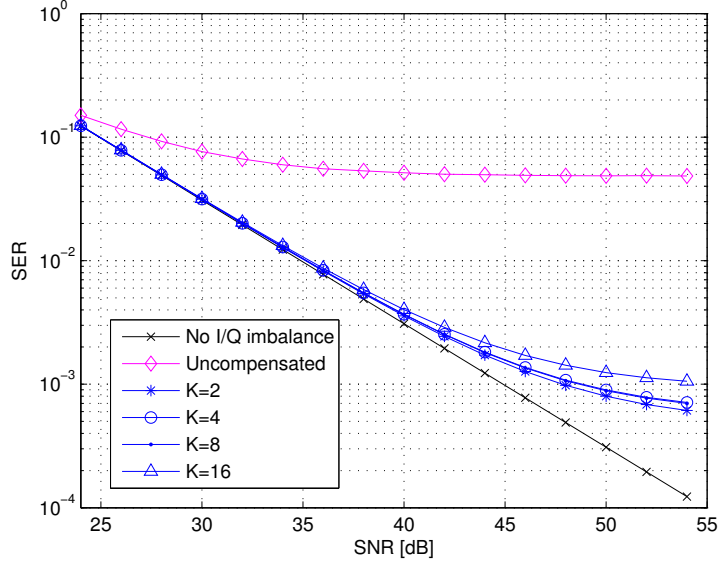


Figure 3.6: The SER performance of the proposed frequency-domain blind I/Q imbalance compensation method for OFDM systems for **Case 2**.

I/Q imbalance parameters based on the second-order statistics of the received signal; the compensation filter can then be obtained in closed-form given these estimated parameters. Simulation results show that the proposed approaches can effectively mitigate the I/Q imbalance and maintain the high performance of the receiver.

Appendix A: Derivations of (3.36)-(3.37)

The derivatives with respect to $w = x + jy$ and $w^* = x - jy$ of $f(w)$ are called the formal partial derivatives of f at $w \in \mathbb{C}$ [Brandwood, 1983], and they are defined as

$$\frac{\partial}{\partial w} f(w) = \frac{1}{2} \left[\frac{\partial}{\partial x} f(w) - j \frac{\partial}{\partial y} f(w) \right], \quad \frac{\partial}{\partial w^*} f(w) = \frac{1}{2} \left[\frac{\partial}{\partial x} f(w) + j \frac{\partial}{\partial y} f(w) \right].$$

Alternatively, when computing $\frac{\partial}{\partial w} f(w)$ and $\frac{\partial}{\partial w^*} f(w)$, w and w^* can be treated as independent variables, i.e., $\frac{\partial w}{\partial w^*} = \frac{\partial w^*}{\partial w} = 0$.

Recall that the filter coefficient matrices are of the form $\mathbf{W} = \begin{bmatrix} w_1 & w_2 \\ w_2^* & w_1^* \end{bmatrix}$. The

*CHAPTER 3. BLIND FREQUENCY-DEPENDENT I/Q IMBALANCE
COMPENSATION FOR DIRECT-CONVERSION RECEIVERS*

derivative is thus defined as [Højrunnes and Gesbert, 2007; Brandwood, 1983]

$$\frac{\partial}{\partial \mathbf{W}^*} f(\mathbf{W}) = \begin{bmatrix} \frac{\partial f}{\partial w_1^*} & \frac{\partial f}{\partial w_2^*} \\ \frac{\partial f}{\partial w_2} & \frac{\partial f}{\partial w_1} \end{bmatrix}.$$

The terms that are needed in computing the gradients in (3.36)-(3.37) are given as follows.

$$\begin{aligned} \frac{\partial}{\partial \mathbf{W}^*} \text{tr}(\mathbf{W}\mathbf{A}) &= \frac{\partial}{\partial \mathbf{W}^*} \text{tr}(\mathbf{A}\mathbf{W}) = \frac{\partial}{\partial \mathbf{W}^*} \text{tr} \left(\begin{bmatrix} a_{11} & a_{12} \\ a_{21} & a_{22} \end{bmatrix} \begin{bmatrix} w_1 & w_2 \\ w_2^* & w_1^* \end{bmatrix} \right) \\ &= \begin{bmatrix} \frac{\partial(a_{11}w_1 + a_{12}w_2^* + a_{21}w_2 + a_{22}w_1^*)}{\partial w_1^*} & \frac{\partial(a_{11}w_1 + a_{12}w_2^* + a_{21}w_2 + a_{22}w_1^*)}{\partial w_2^*} \\ \frac{\partial(a_{11}w_1 + a_{12}w_2^* + a_{21}w_2 + a_{22}w_1^*)}{\partial w_2} & \frac{\partial(a_{11}w_1 + a_{12}w_2^* + a_{21}w_2 + a_{22}w_1^*)}{\partial w_1} \end{bmatrix} = \begin{bmatrix} a_{22} & a_{12} \\ a_{21} & a_{11} \end{bmatrix} \triangleq \mathfrak{T}(\mathbf{A}). \\ \\ \frac{\partial}{\partial \mathbf{W}^*} \text{tr}(\mathbf{A}\mathbf{W}^H) &= \frac{\partial}{\partial \mathbf{W}^*} \text{tr} \left(\begin{bmatrix} a_{11} & a_{12} \\ a_{21} & a_{22} \end{bmatrix} \begin{bmatrix} w_1^* & w_2^* \\ w_2 & w_1 \end{bmatrix} \right) \\ &= \begin{bmatrix} \frac{\partial(a_{11}w_1^* + a_{12}w_2 + a_{21}w_2^* + a_{22}w_1)}{\partial w_1^*} & \frac{\partial(a_{11}w_1^* + a_{12}w_2 + a_{21}w_2^* + a_{22}w_1)}{\partial w_2^*} \\ \frac{\partial(a_{11}w_1^* + a_{12}w_2 + a_{21}w_2^* + a_{22}w_1)}{\partial w_2} & \frac{\partial(a_{11}w_1^* + a_{12}w_2 + a_{21}w_2^* + a_{22}w_1)}{\partial w_1} \end{bmatrix} = \begin{bmatrix} a_{11} & a_{21} \\ a_{12} & a_{22} \end{bmatrix} = \mathbf{A}. \end{aligned}$$

Appendix B: Derivations of (3.42)-(3.44)

Note that the LPFs for both I- and Q-branches are real filters. We therefore have $G_I(f) = G_I^*(-f)$, $G_Q(f) = G_Q^*(-f)$ [Proakis, 1996b] and

$$G_d^*(-f) = \frac{\gamma G_Q^*(-f)}{G_I^*(-f)} = G_d(f). \quad (3.46)$$

Using (3.5) and (3.46), we have

$$\begin{aligned} G_1[k] + G_2^*[-k] &= G_1^*[-k] + G_2[k] = G_I[k], \\ G_1[k] - G_2^*[-k] &= G_I[k]G_d[k]e^{-j\phi}, \\ G_2[k] - G_1^*[-k] &= -G_I[k]G_d[k]e^{j\phi}. \end{aligned} \quad (3.47)$$

*CHAPTER 3. BLIND FREQUENCY-DEPENDENT I/Q IMBALANCE
COMPENSATION FOR DIRECT-CONVERSION RECEIVERS*

Then we can write

$$\begin{aligned}
& \mathbb{E} \{ |X[k] + X^*[-k]|^2 \} \\
&= \mathbb{E} \{ |(G_1[k] + G_2^*[-k])S[k] + (G_1^*[-k] + G_2[k])S^*[-k]|^2 \} \\
&= \mathbb{E} \{ |G_I[k](S[k] + S^*[-k])|^2 \} \\
&= |G_I[k]|^2 (\mathbb{E} \{ |S[k]|^2 \} + \mathbb{E} \{ |S[-k]|^2 \} + \mathbb{E} \{ S[k]S[-k] \} + \mathbb{E} \{ S^*[k]S^*[-k] \}) \\
&= 2|G_I[k]|^2 \sigma_s^2.
\end{aligned} \tag{3.48}$$

Similarly we evaluate the following second-order statistics:

$$\begin{aligned}
& \mathbb{E} \{ |X[k] - X^*[-k]|^2 \} \\
&= \mathbb{E} \{ |(G_1[k] - G_2^*[-k])S[k] + (G_1^*[-k] - G_2[k])S^*[-k]|^2 \} \\
&= 2|G_I[k]|^2 |G_d[k]|^2 \sigma_s^2,
\end{aligned} \tag{3.49}$$

$$\begin{aligned}
\mathbb{E} \{ |X[k]|^2 \} &= |G_1[k]|^2 \mathbb{E} \{ |S[k]|^2 \} + |G_2[k]|^2 \mathbb{E} \{ |S[-k]|^2 \} + \\
&\quad G_1[k]G_2^*[k] \mathbb{E} \{ S[k]S[-k] \} + G_1^*[k]G_2[k] \mathbb{E} \{ S^*[k]S^*[-k] \} \\
&= (|G_1[k]|^2 + |G_2[k]|^2) \sigma_s^2,
\end{aligned} \tag{3.50}$$

$$\begin{aligned}
\mathbb{E} \{ |X[-k]|^2 \} &= |G_1[-k]|^2 \mathbb{E} \{ |S[-k]|^2 \} + |G_2[-k]|^2 \mathbb{E} \{ |S[k]|^2 \} + \\
&\quad G_1[-k]G_2^*[-k] \mathbb{E} \{ S[k]S[-k] \} + G_1^*[-k]G_2[-k] \mathbb{E} \{ S^*[k]S^*[-k] \} \\
&= (|G_1[-k]|^2 + |G_2[-k]|^2) \sigma_s^2,
\end{aligned} \tag{3.51}$$

$$\begin{aligned}
& \mathbb{E} \{ |X[k]|^2 - |X[-k]|^2 \} \\
&= \mathbb{E} \{ |X[k]|^2 \} - \mathbb{E} \{ |X[-k]|^2 \} \\
&= \frac{1}{4} |G_I[k]|^2 \left(|1 + G_d[k]e^{-j\phi}|^2 - |1 + G_d^*[k]e^{-j\phi}|^2 - |1 - G_d[k]e^{j\phi}|^2 + |1 + G_d^*[k]e^{j\phi}|^2 \right) \sigma_s^2 \\
&= 2|G_I[k]|^2 \mathcal{Im}\{G_d[k]\} \sin(\phi).
\end{aligned} \tag{3.52}$$

*CHAPTER 3. BLIND FREQUENCY-DEPENDENT I/Q IMBALANCE
COMPENSATION FOR DIRECT-CONVERSION RECEIVERS*

and

$$\begin{aligned}
 \mathbb{E} \{X[k]X[-k]\} &= G_1[k]G_2[-k]\mathbb{E} \{|S[k]|^2\} + G_1[-k]G_2[k]\mathbb{E} \{|S[-k]|^2\} + \\
 &\quad G_1[k]G_1[-k]\mathbb{E} \{S[k]S[-k]\} + G_2[k]G_2[-k]\mathbb{E} \{S^*[k]S^*[-k]\} \\
 &= (G_1[k]G_2[-k] + G_1[-k]G_2[k])\sigma_s^2 \\
 &= |G_I[k]|^2 \left[\frac{1}{2} (1 - |G_d[k]|^2) - j\mathcal{R}e\{G_d[k]\} \sin(\phi) \right] \sigma_s^2. \quad (3.53)
 \end{aligned}$$

Recall that $G_d[k] = \alpha[k]e^{j\beta[k]}$. Using (3.52) and (3.53), the phase estimate of $\beta[k]$ is expressed in (3.43). Using (3.48), (3.49), the amplitude estimate $\alpha[k]$ is given by (3.42). From (3.43), (3.42) and (3.52), we can estimate the mismatch phase ϕ using (3.44).

Chapter 4

Wideband Spectrum Sensing Based on Sub-Nyquist Sampling

4.1 Introduction

Cognitive radio (CR) is an emerging wireless communication technology that can make efficient use of the radio spectrum by actively locating white spectral space for opportunistic data transmission [Haykin, 2005][Mitola and Maguire, 1999]. Spectrum sensing is a key functionality of cognitive radio, through which the CR searches for unused spectral bands for transmission opportunities, while not interfering with any on-going transmissions by other users. Since in a typical cognitive radio scenario, the CR users have no prior knowledge about the spectrum usage information, sensing a wide band of spectrum is necessary. A number of spectrum sensing methods exist, such as energy detection, filterbank spectrum sensing and multi-taper spectrum estimation, etc. [Ariananda *et al.*, 2009]. All these sensing approaches are based on the Nyquist rate sampling of the signal in the frequency band of interest. In the wideband regime, a major challenge arises from the stringent requirements by the high sampling rate on the analog-to-digital (A/D) converters employed in the receiver. A simple approach is to use a tunable narrowband bandpass filter at the radio-frequency (RF)

CHAPTER 4. WIDEBAND SPECTRUM SENSING BASED ON SUB-NYQUIST SAMPLING

front-end to sense one narrow frequency band at a time [Sahai and Cabric, 2005]. However, the sequential nature of such a scheme could result in missed opportunities or causing interferences to existing users, due to the dynamic nature of the spectrum activities. Alternatively, multiple narrowband bandpass filters [Farhang-Boroujeny, 2008] may be employed, which requires a large number of RF front-end components and therefore significantly increases the cost. Hence a flexible and fast wideband spectrum sensing technique that can operate at sub-Nyquist rate is of great interest.

Sub-Nyquist sampling, also known as compressive sampling [Donoho, 2006a], refers to the techniques of recovering signals from samples obtained using a rate below the Nyquist rate. One straightforward approach to wideband sensing based on sub-Nyquist sampling is a two-stage method. That is, we first reconstruct the wideband signal using the sub-Nyquist samples and then perform spectrum sensing on the reconstructed signal. For the signal reconstruction stage, there are methods for non-blind and blind recovery of multiband signals. The non-blind recovery method was proposed in [Venkataramani and Bresler, 2000] using the multicocet sub-Nyquist sampling to perfectly recover multiband signals. However, this method requires the location of the subbands to be known. (Note that term cocet used in [Venkataramani and Bresler, 2000] is equivalent to a complex A/D converter [Arias and et al., 2006]. Hence in this paper, the terms cocet and complex A/D converter are used interchangeably). Assume that each cocet operates at a sampling rate L times lower than the Nyquist rate. For the non-blind method, if there are $M(\leq L)$ subbands active, then M cocets are sufficient for signal recovery. On the other hand, the blind methods proposed in [Mishali and Eldar, 2009] [Feng and Bresler, 2006] can recover multiband signals without subband information; but at least $2M$ cocets are needed to blindly recover M multiband signals, using the techniques of compressing sensing [Donoho, 2006a]. Other sub-Nyquist sampling techniques include the ones proposed in [Mishali and Eldar, 2010] [Laska and et al., 2006] that involve analog front-end processing.

CHAPTER 4. WIDEBAND SPECTRUM SENSING BASED ON SUB-NYQUIST SAMPLING

Note that for spectrum sensing applications, it is not necessary to recover the multiband signal since the objective is to determine the locations of the active frequency bands. By forgoing the signal recovery stage, it is possible to develop more efficient wideband sensing techniques. In this paper, we propose a single-stage frequency-domain sensing technique based on the multicoset sub-Nyquist sampling. This method can blindly detect the locations of the active subbands. The only prior information required is an upper bound M on the total number of active subbands and the maximum bandwidth W_{\max} of the active subbands. The method is based on directly estimating the power spectrum of the entire frequency band of interest using the coset samples and then perform spectrum detection based on the estimated power spectrum.

There are several works on spectrum estimation with sub-Nyquist sampling. In [Tian and Giannakis, 2007], it is assumed that each subband has sharp edges and an edge detection algorithm is used to detect the subbands. In [Pal and Vaidyanathan, 2011], the coprime sampling scheme is employed that involves using two sampling branches with sampling rates coprime with each other. More closely related works to this paper are [Lexa *et al.*, 2011], [Ariananda *et al.*, 2011], and [Leus and Ariananda, 2011], where various multi-coset sampling schemes are proposed. In [Leus and Ariananda, 2011], only half of the equations are utilized and the compression ratio is inferior to the proposed method in this paper. In [Ariananda *et al.*, 2011] a time-domain method is used whereas here we propose a frequency-domain method which can directly estimate the power spectrum after the time-domain samples are transformed into frequency domain. The method in [Lexa *et al.*, 2011] is a frequency domain approach and depending on the bandwidth and frequency resolution, the number of unknowns could be very large, resulting in large number of A/D branches which makes it difficult to implement in practice due to the fact that multicoset architecture is sensitive to timing jittering.

For the proposed power spectrum estimation, we also analyze the relationship

CHAPTER 4. WIDEBAND SPECTRUM SENSING BASED ON SUB-NYQUIST SAMPLING

between the number of cosets and the subbands. First, a sufficient condition is proved for an universal sampling pattern of the multi-coset sampler. Second, the minimum number of required cosets P is given that satisfies $P(P-1)+1 \geq L \geq M$, where $L = \left\lceil \frac{W_{\text{tot}}}{W_{\text{max}}} \right\rceil$, and W_{tot} is the total bandwidth. For the sampling pattern that can achieve the highest possible compression ratio, i.e. $\frac{L}{P}$, the problem can be reformulated as a minimal sparse ruler problem [Ariananda *et al.*, 2011], which is a combinatorial problem and computationally hard [Leech, 1956]. On the other hand, note that for the spectrum sensing application, there is a tradeoff between compression rate and sensing performance. That is, higher compression ratio leads to worse sensing performance. Hence in practice, the compression ratio should be kept at a level such that the sensing performance is acceptable. Finally, we note that the multicoset sub-Nyquist sampling is closely related to the the maximum degree-of-freedom antenna array design problem [Ma *et al.*, 2009], [Pal and Vaidyanathan, 2010].

The remainder of the paper is organized as follows. In Section 4.2, the multiband signal model and the spectrum sensing problem are described. In Section 4.3, a blind power spectrum estimation method based on multicoset sampling is proposed, and the corresponding digital implementation is discussed. In Section 4, a constant-false-alarm frequency-bin energy detector based on the estimated power spectrum is developed. Simulation results are provided in Section 4.5. Finally Section 4.6 concludes the paper.

4.2 Signal Model and Problem Statement

Assume that the wideband spectrum to be monitored in a cognitive radio system is $\mathcal{F} = [f_{\min}, f_{\max}]$. During the sensing period, there are m active disjoint subband user signals present in \mathcal{F} . The i -th subband signal is given by

$$s_i(t) = \sum_{n \in \mathbb{Z}} d_i[n] g_i(t - nT_i) e^{j2\pi f_i t}, \quad i = 1, 2, \dots, m, \quad (4.1)$$

CHAPTER 4. WIDEBAND SPECTRUM SENSING BASED ON SUB-NYQUIST SAMPLING

where $\{d_i[n]\}$ is a sequence of modulation symbols, $g_i(t)$ is the pulse-shaping function, and f_i is the carrier frequency of $s_i(t)$. Each subband signal $s_i(t)$ is bandlimited to $B_i = [f_i^l, f_i^u]$, $i = 1, 2, \dots, m$ with bandwidth $W_i = f_i^u - f_i^l$ and carrier frequency $f_i = \frac{f_i^l + f_i^u}{2}$. It is assumed that the subband signals $s_1(t), s_2(t), \dots, s_m(t)$ are independent and zero-mean. The observed signal during the sensing period is given by

$$x(t) = \sum_{i=1}^m s_i(t - \tau_i) + n(t),$$

where τ_i is the delay of the i -th subband signal and $n(t)$ is the additive white Gaussian noise with power spectrum density σ^2 . Fig. 4.1 (a) illustrates a wideband spectrum $\mathcal{F} = [0, f_{\max}]$ in which there are three ($m = 3$) active subbands B_1 , B_2 and B_3 being used by the primary or secondary users for data transmission.

Denote $W_{\max} = \max_{i=1}^m W_i$. The wideband spectrum sensing problem is the following. Given an upper bound M on the total number of active subband signals and the maximum subband bandwidth W_{\max} , we need to estimate the actual number m of the active subbands and their frequency bands B_1, B_2, \dots, B_m , with $m \leq M$.

One traditional approach to solve the above wideband spectrum sensing problem is to first estimate the power spectrum density over \mathcal{F} , based on which we then perform energy detection to identify the active bands. This kind of spectral estimator is referred to as periodogram [Urkowitz, 1967]. In practice, periodogram is often computed by using FFT from a finite Nyquist samples and is formed after taking the average magnitude squared of the FFT. One of major advantages of classical periodogram-based spectral estimation methods is that they have lower computation cost, and, therefore can be efficiently implemented by using FFT. On the other hand, the frequency resolution (frequency bin) of periodogram could be limited by finite collected Nyquist samples. For example, if without using any zero-padding, the maximum frequency resolution is equal to $2\pi/N$ for N input Nyquist samples.

Since the location of each active subband is unknown, in general, the Nyquist sampling with rate $\frac{1}{T} = f_{\max} - f_{\min}$ is needed, which might not be feasible by

CHAPTER 4. WIDEBAND SPECTRUM SENSING BASED ON SUB-NYQUIST SAMPLING

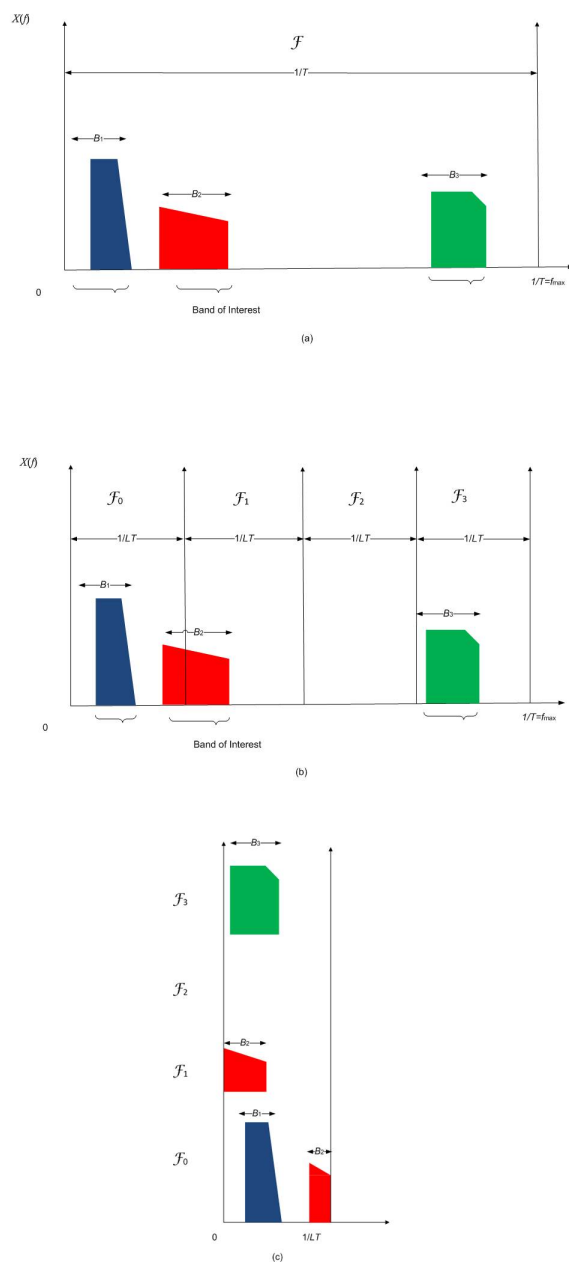


Figure 4.1: (a) Multiband signals with different central carrier frequencies. (b) The vector $\mathbf{X}(f)$ is constructed by dividing \mathcal{F} into $L = 4$ (down-sampling factor) intervals. (c) The folded spectrum $\mathbf{Y}(f)$.

the current A/D conversion technology due to the wideband nature of the signal. An alternative approach is to evenly divide the spectrum \mathcal{F} into L parts, $\mathcal{F}_i = [f_{\min} + \frac{i}{LT}, f_{\min} + \frac{i+1}{LT})$, $i = 0, \dots, L-1$, and to estimate the power spectrum of each part. Specifically, we can employ L bandpass filters to partition \mathcal{F} into L parts, followed by L bandpass samplers each with a decimated sampling rate $\frac{1}{LT}$ [Vaughan *et al.*, 1991]. However, such an approach incurs high cost both in terms of hardware (since L bandpass filters and samplers are needed) and computation (since L power spectra are computed). In this paper, we consider a sub-Nyquist sampling scheme called multicoset sampling [Venkataramani and Bresler, 2000] and develop an efficient power spectrum estimation method based on such sampling scheme.

4.3 Power Spectrum Estimation under Multicoset Sampling

4.3.1 Multicoset Sampling

The multicoset sampling is based on the multirate signal processing and it employs parallel cosets (or A/D branches) that uniformly sample the signal at a decimated rate. In particular, given a decimation factor L , the number of cosets P satisfies $P \leq L$. Each coset corresponds to a polyphase component of the bandlimited signal $x(t)$. When $P = L$, all polyphase components of $x(t)$ are included and the multicoset sampling becomes equivalent to the polyphase implementation of the Nyquist sampling. The sampling pattern for the coset branches (or polyphase components) is described by the set $\mathcal{C} = \{c_0, c_1, \dots, c_{P-1}\} \subseteq \{0, 1, \dots, L-1\}$ which contains P distinct integers. The i -th coset then takes uniform samples with rate $\frac{1}{LT}$ at time instants $(kL + c_i)T$, $k \in \mathbb{Z}$. The continuous-time sampled signal of the i -th coset (i -th polyphase component) is given by [Venkataramani and Bresler, 2000], [Mishali

CHAPTER 4. WIDEBAND SPECTRUM SENSING BASED ON SUB-NYQUIST SAMPLING

and Eldar, 2009]

$$y_i(t) = x(t) \sum_{m \in \mathbb{Z}} \delta(t - (mL + c_i)T), \quad i = 0, 1, \dots, P-1, \quad (4.2)$$

where $\delta(t)$ denotes the delta function. Denote the corresponding discrete-time sample sequence as [Venkataramani and Bresler, 2000]

$$y_i[n] = \begin{cases} x(nT), & n = mL + c_i, \\ 0, & \text{otherwise,} \end{cases} \quad i = 0, 1, \dots, P-1, \quad (4.3)$$

where $\delta[n]$ is the Kronecker delta function. The Fourier transform of $y_i(t)$ can be written as [Venkataramani and Bresler, 2000]

$$\begin{aligned} Y_i(f) &= \int_{-\infty}^{\infty} y_i(t) e^{-j2\pi ft} dt = \int_{-\infty}^{\infty} \sum_{m \in \mathbb{Z}} x(t) \delta(t - (mL + c_i)T) e^{-j2\pi ft} dt \\ &= \sum_{m \in \mathbb{Z}} x((mL + c_i)T) e^{-j2\pi f(mL + c_i)T} = \sum_{n=-\infty}^{\infty} y_i[n] e^{-j2\pi fnT} = Y_i(e^{j2\pi fT}) \end{aligned} \quad (4.4)$$

where $Y_i(e^{j2\pi fT})$ is the discrete-time Fourier transform (DTFT) of $y_i[n]$. On the other hand, from (4.2), $Y_i(f)$ can also be expressed as

$$\begin{aligned} Y_i(f) &= X(f) * \frac{1}{LT} \sum_{\ell \in \mathbb{Z}} \delta\left(f + \frac{\ell}{LT}\right) e^{\frac{j2\pi c_i \ell}{L}} \\ &= \frac{1}{LT} \sum_{\ell \in \mathbb{Z}} \underbrace{X\left(f + \frac{\ell}{LT}\right)}_{X_\ell(f)} e^{\frac{j2\pi c_i \ell}{L}} \\ &= \frac{1}{LT} \sum_{\ell=0}^{L-1} X_\ell(f) e^{\frac{j2\pi c_i \ell}{L}}, \quad f \in \left[0, \frac{1}{LT}\right). \end{aligned} \quad (4.5)$$

where $*$ denotes the convolution; and (4.5) follows from the assumption that $X(f) = 0$ for $f \notin \mathcal{F} = [0, f_{\max}]$. We can write (4.5) in matrix form as (cf. Appendix in [Mishali and Eldar, 2009])

CHAPTER 4. WIDEBAND SPECTRUM SENSING BASED ON SUB-NYQUIST SAMPLING

$$\underbrace{\begin{bmatrix} Y_0(e^{j2\pi fT}) \\ Y_1(e^{j2\pi fT}) \\ \vdots \\ Y_{P-1}(e^{j2\pi fT}) \end{bmatrix}}_{\mathbf{Y}(e^{j2\pi fT})} = \frac{1}{LT} \underbrace{\begin{bmatrix} e^{\frac{j2\pi c_1 0}{L}} & e^{\frac{j2\pi c_1 1}{L}} & \dots & e^{\frac{j2\pi c_1 (L-1)}{L}} \\ e^{\frac{j2\pi c_2 0}{L}} & e^{\frac{j2\pi c_2 1}{L}} & \dots & e^{\frac{j2\pi c_2 (L-1)}{L}} \\ \vdots & \vdots & \dots & \vdots \\ e^{\frac{j2\pi c_P 0}{L}} & e^{\frac{j2\pi c_P 1}{L}} & \dots & e^{\frac{j2\pi c_P (L-1)}{L}} \end{bmatrix}}_{\mathbf{A}} \underbrace{\begin{bmatrix} X_0(f) \\ X_1(f) \\ \vdots \\ X_{L-1}(f) \end{bmatrix}}_{\mathbf{X}(f)}, \quad f \in \left[0, \frac{1}{LT}\right). \quad (4.6)$$

It is seen from (4.6) that the spectrum band of interest \mathcal{F} is evenly divided into L parts, $\mathcal{F}_i = \left[\frac{i}{LT}, \frac{i+1}{LT}\right)$, $i = 0, 1, \dots, L-1$. Moreover, $\mathcal{F}_1, \mathcal{F}_2, \dots, \mathcal{F}_L$ are all folded into \mathcal{F}_0 to form $\mathbf{Y}(e^{j2\pi fT})$. These are illustrated in Fig. 4.1 (b)-(c).

Recall that the observed signal is given by $x(t) = s(t) + n(t)$, where $s(t) = \sum_{i=1}^m s_i(t - \tau_i)$. The corresponding Fourier transform is given by $X(f) = S(f) + N(f)$, where $S(f)$ and $N(f)$ denote the Fourier transforms of $s(t)$ and $n(t)$, respectively. Define $S_i(f) = S(f + \frac{i}{LT})$, $i = 0, 1, \dots, L-1$ and $\mathbf{S}(f) = [S_0(f), S_1(f), \dots, S_{L-1}(f)]^T$. Similarly define $N_i(f)$ and $\mathbf{N}(f)$. Then (4.6) can be written as

$$\mathbf{Y}(e^{j2\pi fT}) = \mathbf{A}\mathbf{X}(f) = \mathbf{A}[\mathbf{S}(f) + \mathbf{N}(f)], \quad f \in \left[0, \frac{1}{LT}\right). \quad (4.7)$$

Proposition 1: If the decimation factor L is chosen such that $\frac{1}{LT} \geq W_{\max}$, then we have $\|\mathbf{S}(f)\|_0 \leq M, \forall f \in \left[0, \frac{1}{LT}\right)$, i.e., the number of nonzero elements in $\mathbf{S}(f)$ is less than or equal to M for all $f \in \left[0, \frac{1}{LT}\right)$.

Proof: Since M is the upper bound on the total number of active subbands in \mathcal{F} , if $\|\mathbf{S}(f)\|_0 > M$, then at least two nonzero elements of $\mathbf{S}(f)$, say $S_i(f) = S(f + \frac{i}{LT})$ and $S_j(f) = S(f + \frac{j}{LT})$, $i \neq j$, belong to a same active subband, say B_l , which implies that the bandwidth of B_l satisfies $W_l \geq \frac{|j-i|}{LT} \geq \frac{1}{LT}$. This contradicts the assumption that $\frac{1}{LT} \geq W_{\max}$. \square

We next introduce some definitions and properties associated with the multiset sampling which are instrumental to the subsequent development.

Definition 1: The Kruskal-rank (K-rank) of a matrix \mathbf{A} , denote as $K_{\mathbf{A}}$, is the maximum number κ such that any κ columns of \mathbf{A} are linearly independent [Venkataramani

CHAPTER 4. WIDEBAND SPECTRUM SENSING BASED ON SUB-NYQUIST SAMPLING

and Bresler, 2000]. It is obvious that the rank of a matrix is greater than or equal to its K-rank.

Definition 2: A sampling pattern \mathcal{C} is called (L, P) universal, if any P columns of \mathbf{A} are linearly independent [Venkataramani and Bresler, 2000]. A sampling pattern \mathcal{C} that yields full K-rank is simply called universal. That is, for a universal sampling pattern \mathcal{C} , the K-rank of the $P \times L$ ($P < L$) matrix \mathbf{A} is P .

Property 1: For any given L and P , with $P \leq L$, the sampling pattern $\mathcal{C} = \{0, 1, \dots, P-1\}$ is universal. This is because the corresponding matrix \mathbf{A} is a Vandermonde matrix. In fact, any P consecutive numbers in $\{0, 1, \dots, L-1\}$ yield a universal sampling pattern.

In the multicoset sampling scheme discussed above, the sampling pattern $\mathcal{C} = \{c_0, c_1, \dots, c_{P-1}\}$ should be universal. The proposed multiband spectrum sensing method based on multicoset sampling is illustrated in Fig. 4.2.

4.3.2 Power Spectrum Estimation

Define the autocorrelation matrix of $\mathbf{Y}(e^{j2\pi fT})$ as

$$\mathbf{R}_{\mathbf{Y}}(e^{j2\pi fT}) \triangleq \mathbb{E} \{ \mathbf{Y}(e^{j2\pi fT}) \mathbf{Y}^H(e^{j2\pi fT}) \}.$$

Similarly define $\mathbf{R}_{\mathbf{X}}(f)$, $\mathbf{R}_{\mathbf{S}}(f)$ and $\mathbf{R}_{\mathbf{N}}(f)$. Then from (4.7) we have

$$\mathbf{R}_{\mathbf{Y}}(e^{j2\pi fT}) = \mathbf{A} \mathbf{R}_{\mathbf{X}}(f) \mathbf{A}^H = \mathbf{A} [\mathbf{R}_{\mathbf{S}}(f) + \mathbf{R}_{\mathbf{N}}(f)] \mathbf{A}^H. \quad (4.8)$$

The (i, j) -th element of $\mathbf{R}_{\mathbf{X}}(f)$ can be expressed as

$$\begin{aligned} [\mathbf{R}_{\mathbf{X}}(f)]_{i,j} &= \mathbb{E} \{ X_i(f) X_j^*(f) \} = \mathbb{E} \{ (S_i(f) + N_i(f)) (S_j(f) + N_j(f))^* \} \\ &= \mathbb{E} \{ S_i(f) S_j^*(f) \} + \mathbb{E} \{ N_i(f) N_j^*(f) \} \\ &= \mathbb{E} \{ |S_i(f)|^2 \} \delta(i-j) + \sigma^2 \delta(i-j), \end{aligned} \quad (4.9)$$

where in the last equality the first term follows from Proposition 1; and the second term follows from the assumption that the noise is stationary and white wherein the

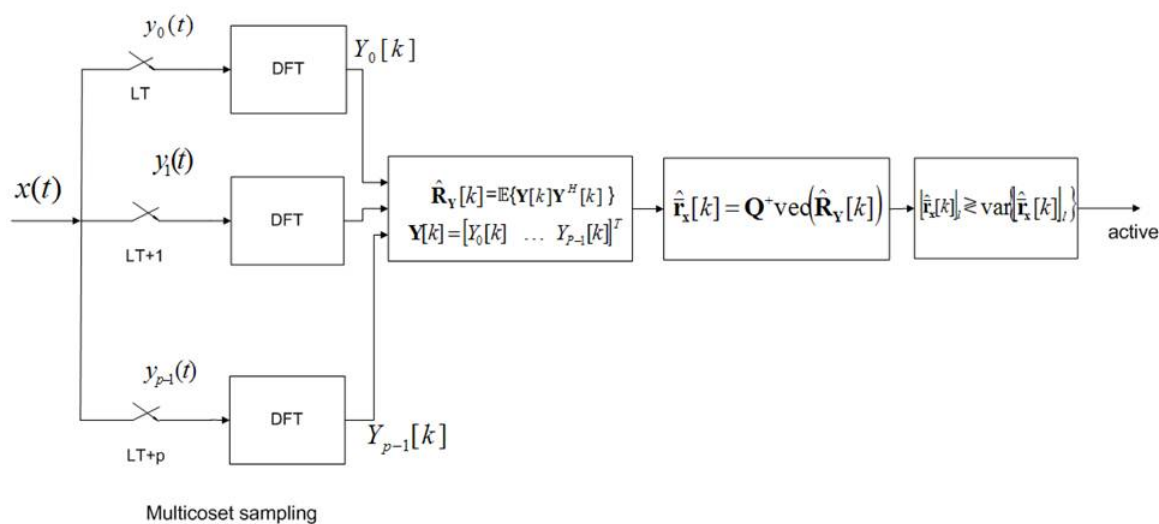


Figure 4.2: The diagram of the proposed multiband spectrum sensing method based on multicoset sampling.

CHAPTER 4. WIDEBAND SPECTRUM SENSING BASED ON SUB-NYQUIST SAMPLING

fact that for stationary processes $\mathbb{E}\{N(f)N^*(f - \alpha)\} = 0, \forall \alpha \neq 0$ [Gardner *et al.*, 2006].

From (4.9) and Proposition 1, it follows that $\mathbf{R}_S(f)$ is an $L \times L$ diagonal matrix with at most M non-zero elements on the diagonal but $\mathbf{R}_N(f)$ has L non-zero elements on the diagonal, therefore, $\mathbf{R}_X(f)$ has L non-zero elements on the diagonal. Define the $\text{vec}(\cdot)$ operator as $\text{vec}(\mathbf{A}) \triangleq [\mathbf{a}_1^T, \mathbf{a}_2^T, \dots]^T$, where \mathbf{a}_j denotes the j -th column of matrix \mathbf{A} . Using the matrix identity $\text{vec}(\mathbf{AXB}) = (\mathbf{B}^T \otimes \mathbf{A}) \text{vec}(\mathbf{X})$, where \otimes denotes the Kronecker product, we have

$$\begin{aligned} \mathbf{r}_Y(e^{j2\pi fT}) &\triangleq \text{vec}(\mathbf{R}_Y(e^{j2\pi fT})) \\ &= \left[(\mathbf{A}^H)^T \otimes \mathbf{A} \right] \text{vec}(\mathbf{R}_X(f)) \\ &= (\mathbf{A}^* \otimes \mathbf{A}) \mathbf{r}_X(f). \end{aligned} \quad (4.10)$$

Note that from (4.9) the $L^2 \times 1$ vector $\mathbf{r}_X(f)$ is of the form

$$\begin{aligned} \mathbf{r}_X(f) = \text{vec}(\mathbf{R}_X(f)) &= \left[\mathbf{r}_{\mathbf{x}_0}^T, \mathbf{r}_{\mathbf{x}_1}^T, \dots, \mathbf{r}_{\mathbf{x}_{L-1}}^T \right]^T \\ &= [P_0(f)\mathbf{e}_0^T, P_1(f)\mathbf{e}_1^T, \dots, P_{L-1}(f)\mathbf{e}_{L-1}^T]^T. \end{aligned} \quad (4.11)$$

where $P_i(f) \triangleq \mathbb{E}\{|X_i(f)|^2\} = \mathbb{E}\{|S_i(f)|^2\} + \sigma^2$, and \mathbf{e}_i is an $L \times 1$ vector with the i -th element being 1 and zeros elsewhere.

We further define an $L \times 1$ vector $\bar{\mathbf{r}}_X(f) \triangleq [P_0(f), P_1(f), \dots, P_{L-1}(f)]^T$, and an $L^2 \times L$ selection matrix \mathbf{B} that has a “1” at the j -th column and the $[(j-1)L + j]$ -th row, $j = 1, 2, \dots, L$, and zeros elsewhere. Then we can write

$$\mathbf{r}_X(f) = \mathbf{B} \bar{\mathbf{r}}_X(f). \quad (4.12)$$

Therefore (4.10) can be rewritten as

$$\mathbf{r}_Y(e^{j2\pi fT}) = (\mathbf{A}^* \otimes \mathbf{A}) \mathbf{B} \bar{\mathbf{r}}_X(f) = \mathbf{Q} \bar{\mathbf{r}}_X(f), \quad (4.13)$$

$$\text{with} \quad \mathbf{Q} \triangleq (\mathbf{A}^* \otimes \mathbf{A}) \mathbf{B}, \quad (4.14)$$

where \mathbf{Q} is a $P^2 \times L$ matrix. If \mathbf{Q} has full column rank, denoting its pseudo inverse as \mathbf{Q}^\dagger , then

$$\bar{\mathbf{r}}_X(f) = \mathbf{Q}^\dagger \mathbf{r}_Y(e^{j2\pi fT}). \quad (4.15)$$

CHAPTER 4. WIDEBAND SPECTRUM SENSING BASED ON SUB-NYQUIST SAMPLING

Thus, using (4.15), the power spectrum in each partition $\mathcal{F}_0, \mathcal{F}_1, \dots, \mathcal{F}_{L-1}$ corresponding to any folded frequency $f \in [0, \frac{1}{LT})$ can be computed and therefore the power spectrum for the entire band \mathcal{F} can be obtained. Note that the matrix \mathbf{Q}^\dagger can be calculated off-line.

In (4.15), it is assumed that the pseudo-inverse of the \mathbf{Q} matrix exists. Therefore, we need to analyze the \mathbf{Q} matrix to see under what condition this assumption is valid. First, we give a sufficient condition for the $P^2 \times L$ matrix \mathbf{Q} to be of full column rank L . It turns out that the simplest sampling pattern, i.e. the universal sampling pattern, can guarantee the full column rank of \mathbf{Q} .

Proposition 2: If the $P \times L$ matrix $\mathbf{A} = [\mathbf{a}_1 \ \mathbf{a}_2 \ \dots \ \mathbf{a}_L]$ in (4.6) is obtained from a universal sampling pattern \mathcal{C} , then the K-rank of matrix \mathbf{Q} is L , i.e., $K_{\mathbf{Q}} = L$ when $2P - 1 \geq L$.

Proof: Since $\mathbf{Q} \triangleq (\mathbf{A}^* \otimes \mathbf{A}) \mathbf{B}$ and \mathbf{B} selects the $[(j-1)L + j]$ -th column from $(\mathbf{A}^* \otimes \mathbf{A})$, for $j = 1, \dots, L$, then \mathbf{Q} can be written as

$$\mathbf{Q} = \begin{bmatrix} \mathbf{a}_1^* \otimes \mathbf{a}_1 & \mathbf{a}_2^* \otimes \mathbf{a}_2 & \dots & \mathbf{a}_L^* \otimes \mathbf{a}_L \end{bmatrix} = \mathbf{A}^* \odot \mathbf{A}, \quad (4.16)$$

where \odot is the Khatri-Rao product [Sidiropoulos and Liu, 2001]. Lemma 1 (The K-rank of Khatri-Rao Product) in [Sidiropoulos and Liu, 2001] states that if $\mathbf{D}_{I \times F} = \mathbf{B}_{I \times F} \odot \mathbf{C}_{J \times F}$, then $K_{\mathbf{D}} \geq \min(K_{\mathbf{B}} + K_{\mathbf{C}} - 1, F)$. Since $\mathbf{Q}_{P^2 \times L} = \mathbf{A}_{P \times L}^* \odot \mathbf{A}_{P \times L}$, we have

$$K_{\mathbf{Q}} \geq \min(K_{\mathbf{A}^*} + K_{\mathbf{A}} - 1, L). \quad (4.17)$$

By the definition of universality [cf. Definition 2], we have $K_{\mathbf{A}} = K_{\mathbf{A}^*} = P$. If $K_{\mathbf{A}^*} + K_{\mathbf{A}} - 1 = 2P - 1 \geq L$, then from (4.16) and the fact that the number of columns of \mathbf{Q} is L , we can conclude that $K_{\mathbf{Q}} = L$. \square

Remark 1: By Propositions 1 and 2, if the number of cosets P and the decimation factor L are chosen such that $2P - 1 \geq L \geq M$, then it is guaranteed that the power spectrum vector $\bar{\mathbf{r}}_{\mathbf{X}}(f)$ can be computed by (4.15) for $f \in [0, \frac{1}{LT})$. This way we can obtain the power spectrum of the entire band of interest \mathcal{F} .

CHAPTER 4. WIDEBAND SPECTRUM SENSING BASED ON SUB-NYQUIST SAMPLING

In addition, the Proposition 2 can be extended to use for the sufficient condition for the unique recovery condition in compressed sensing when the number of supports (unknown) in $\bar{\mathbf{r}}_{\mathbf{x}}(f)$ is less than P (cf. Lemma 1 in [Pal and Vaidyanathan, 2012]). In other words, if $\|\bar{\mathbf{r}}_{\mathbf{x}}(f)\|_0 \leq P$, where $\|\mathbf{x}\|_0$ denotes 0-norm of vector \mathbf{x} and since the K-rank of matrix $\mathbf{Q} \geq 2P$ is satisfied for any universal sampling pattern then unique recovery of $\bar{\mathbf{r}}_{\mathbf{x}}(f)$ is guaranteed.

4.3.3 A Lower Bound on the Number of Cosets

Proposition 2 gives a *sufficient* condition on P for \mathbf{Q} to have full rank, i.e., $P \geq \frac{L+1}{2}$. Next we give a necessary condition on P , similar to those given in [Lexa *et al.*, 2011; Ariananda *et al.*, 2011].

Proposition 3: A necessary condition on P such that \mathbf{Q} has full column rank is $P(P-1) + 1 \geq L$.

Proof: From (16), \mathbf{Q} is the Khatri-Rao product of \mathbf{A}^* and \mathbf{A} and the number of rows in \mathbf{Q} is P^2 . From (4.6), the q -th row, $0 \leq q = \mu P + \nu \leq P^2 - 1$, where $0 \leq \mu, \nu \leq P-1$ of \mathbf{Q} can be expressed as $\left(\frac{1}{LT}\right)^2 \left[e^{\frac{-j2\pi(c_\mu - c_\nu)0}{L}}, e^{\frac{-j2\pi(c_\mu - c_\nu)1}{L}}, \dots, \frac{-j2\pi(c_\mu - c_\nu)(L-1)}{L} \right]$, where $c_\mu, c_\nu \in \mathcal{C}$ and \mathcal{C} is a sampling pattern set. When $\mu = \nu$ such that $c_\mu - c_\nu = 0$, then the rows of \mathbf{Q} indexed as $0, P+1, 2P+2, \dots, P(P-1) + P-1$ are identical. The rank of \mathbf{Q} is maximized when the remaining $P^2 - P$ rows are linearly independent and they are independent of this identical row. Therefore, the rank of the \mathbf{Q} is upper bounded by $P(P-1) + 1$. \square

Remark 2: One can immediately conclude that in order to achieve the smallest value of P , a sampling pattern set \mathcal{C} should be chosen to satisfy $P(P-1) + 1 = L$ and the rank of \mathbf{Q} has to be equal to L . The condition can be satisfied if the difference set $\mathcal{D}_c = \{|c_\mu - c_\nu| : \mu, \nu \in \mathcal{C}\}$ equals $\left\{0, 1, 2, \dots, \frac{(L-1)}{2}\right\}$. In this case, \mathbf{Q} will be a Vandermonde matrix with L distinct rows thus \mathbf{Q} will have full rank L . This is a combinatorial optimization problem known as the minimal sparse ruler which is computationally hard [Leech, 1956], [Leus and Ariananda, 2011], [Shakeri *et al.*, 2012].

CHAPTER 4. WIDEBAND SPECTRUM SENSING BASED ON SUB-NYQUIST SAMPLING

Therefore, although the universal sampling pattern can only achieve $P \cong \frac{L}{2}$, this sampling pattern is trivial to obtain with no computation involved and it exists for every value of L . It will be seen in Section 5 that the spectrum detection performance degrades as the compression ratio $\frac{L}{P}$ becomes higher. Hence, in practice, we need to balance the compression ratio and the detection performance. We next give two simple structured sampling patterns with compression ratios higher than 2 that do not require a pattern search.

Proposition 4: For P branches, the sampling patterns $\mathcal{C} = \{0, 1, \dots, P-2, 2P-3\} + \alpha$ where $\alpha \in \{0, 1, 2, \dots, 2(P-1)-1\}$ yield full rank \mathbf{Q} matrix for $L = 2(2P-3) + 1$.

Proof: Since \mathbf{Q} is a “tall” matrix, we focus on the distinct rows since they determine the rank of \mathbf{Q} . Using the sampling pattern \mathcal{C} , there exist $L = 2(2P-3) + 1$ distinct consecutive phase differences $c_u - c_v \in \{0 \pm 1 \pm 2 \dots \pm(2P-3)\}$. Consider an $L \times L$ submatrix of \mathbf{Q} composed of these L distinct consecutive phase differences, i.e. $\begin{bmatrix} e^{-j\frac{2\pi(c_u-c_v)0}{L}} & e^{-j\frac{2\pi(c_u-c_v)1}{L}} & \dots & e^{-j\frac{2\pi(c_u-c_v)(L-1)}{L}} \end{bmatrix}$ and denote this submatrix of \mathbf{Q} as \mathbf{Q}_v . It then follows that \mathbf{Q}_v is a Vandermonde matrix. Since these distinct phase differences are consecutive, using the fact that a Vandermonde matrix with generators spaced equally on a unit circle has full rank (cf. Theorem 2.2.2 in [Gershman and Sidiropoulos, 2005]), this proposition is proved. \square

The next sampling pattern is inspired by [Pal and Vaidyanathan, 2010], where a two-level nested array geometry is proposed that leads to a Vandermonde matrix therefore can also be utilized as a sampling pattern. To be more specific, assuming P is even, then for $L = \frac{P^2-2}{2} + P$, the sampling pattern

$$\mathcal{C} = \left\{ \left\{ \{n\} \cup \left\{ n\left(\frac{P}{2} + 1\right) \right\} \right\} + \alpha, n = 1, 2, \dots, \frac{P}{2} \right\}$$

where $\alpha \in \{-1\} \cup \{1, 2, \dots, \frac{L-1}{2}\}$ guarantees a full rank \mathbf{Q} .

4.3.4 Digital Implementation

In practice, the Fourier transform is implemented in the digital domain by using the FFT. In this subsection, we discuss the digital implementation of the power spectrum estimation method described in the previous section.

The wideband signal is sampled via the multicoset sampling scheme in which P cosets are used, each with a sampling rate of $\frac{1}{LT}$. Although in (4.3) each sequence $y_i[n], i = 0, \dots, P-1$ contains $L-1$ zeros in between the down-sampled signal, in practice, the FFT of $y_i[n]$ can be obtained from the FFT of $\bar{y}_i[m]$, where $\bar{y}_i[m] = y_i[mL + c_i]$, is the down-sampled signal without the zero insertions. In particular, consider the U -point FFT of $y_i[n]$ where $U = NL$. We have

$$\begin{aligned} Y_i[k] &= \frac{1}{\sqrt{U}} \sum_{n=0}^{U-1} y_i[n] e^{-j\frac{2\pi}{U}nk} = \frac{1}{\sqrt{U}} \sum_{m=0}^{N-1} x[mL + c_i] e^{-j\frac{2\pi}{NL}(mL+c_i)k} \\ &= \left(\frac{1}{\sqrt{U}} \sum_{m=0}^{N-1} \bar{y}_i[m] e^{-j\frac{2\pi}{N}mk} \right) e^{-j\frac{2\pi}{U}c_ik}, \quad 0 \leq k \leq U-1 \end{aligned} \quad (4.18)$$

That is the U -point FFT of $y_i[n]$ is obtained by multiplying the N -point FFT of $\bar{y}_i[m]$ by a constant phasor $e^{-j\frac{2\pi}{U}c_ik}$. Note that the frequency resolution is $\Delta f = \frac{1}{NLT} = \frac{1}{UT}$ and this corresponds to discretizing $[0, \frac{1}{LT})$ into N grids.

On the other hand, if the signal is sampled at the Nyquist rate $\frac{1}{T}$, i.e., $y[n] = x(nT)$, then the U -point FFT of $y[n]$ also has a frequency resolution $\Delta f = \frac{1}{UT}$ which corresponds to discretizing $\mathcal{F} = [0, \frac{1}{T})$ into U grids. Thus, although in our proposed method, the sampling rate is L -times lower than the Nyquist rate, the frequency resolution remains the same.

For the finite-length discrete-time signals we can derive the DFT version of (4.6) as follows. Note that the finite-length discrete impulse train is

$$v_i[n] = \sum_{m=0}^{N-1} \delta[n - (mL + c_i)], \quad 0 \leq n \leq NL - 1.$$

CHAPTER 4. WIDEBAND SPECTRUM SENSING BASED ON SUB-NYQUIST SAMPLING

Its DFT can be expressed as

$$\begin{aligned}
 V_i[k] &= \frac{1}{\sqrt{NL}} \sum_{n=0}^{NL-1} \left\{ \sum_{m=0}^{N-1} \delta[n - (mL + c_i)] \right\} e^{-j\frac{2\pi}{NL}nk} \\
 &= \frac{1}{\sqrt{NL}} \sum_{m=0}^{N-1} \sum_{n=0}^{NL-1} \delta[n - (mL + c_i)] e^{-j\frac{2\pi}{NL}nk} \\
 &= \frac{1}{\sqrt{NL}} \sum_{m=0}^{N-1} e^{-j\frac{2\pi}{N}mk} e^{-j\frac{2\pi}{NL}c_ik} \\
 &= \sqrt{\frac{N}{L}} \sum_{\ell=0}^{L-1} \delta[k - \ell N] e^{-j\frac{2\pi}{NL}c_ik} \\
 &= \sqrt{\frac{N}{L}} \sum_{\ell=0}^{L-1} \delta[k - \ell N] e^{-j\frac{2\pi}{L}c_i\ell}, \quad 0 \leq k \leq NL - 1. \tag{4.19}
 \end{aligned}$$

Define $x[n] \triangleq x(nT)$, its DFT $X[k] \triangleq \frac{1}{\sqrt{NL}} \sum_{n=0}^{NL-1} x[n] e^{-j\frac{2\pi}{NL}nk}$, $0 \leq k \leq NL - 1$, and the partitions $X_i[k] \triangleq X[k + iN]$, $0 \leq i \leq L - 1$, $0 \leq k \leq N - 1$. Since $y_i[n] = x[n] \cdot v_i[n]$, after taking the DFT, we have $Y_i[k] = X[k] \star V_i[k]$, where \star denotes the circular convolution. Let $z[(n - m)_L]$ denote the circular shift of a sequence $z[n]$ of length L . Then for $0 \leq k \leq N - 1$,

$$\begin{aligned}
 Y_i[k] &= \sqrt{\frac{N}{L}} \sum_{\ell=0}^{L-1} X[k] \star \delta[(k - \ell N)] e^{-j\frac{2\pi}{L}c_i\ell} = \sqrt{\frac{N}{L}} \sum_{\ell=0}^{L-1} X[(k - \ell N)_{NL}] e^{-j\frac{2\pi}{L}c_i\ell} \\
 &= \sqrt{\frac{N}{L}} \left\{ X[k] e^{-j\frac{2\pi}{L}c_i0} + X[k + (L - 1)N] e^{-j\frac{2\pi}{L}c_i1} + X[k + (L - 2)N] e^{-j\frac{2\pi}{L}c_i2} + \right. \\
 &\quad \left. \dots + X[k + N] e^{-j\frac{2\pi}{L}c_i(L-1)} \right\} \\
 &= \sqrt{\frac{N}{L}} \left\{ X_0[k] + X_{L-1}[k] e^{j\frac{2\pi}{L}c_i(L-1)} + X_{L-2}[k] e^{j\frac{2\pi}{L}c_i(L-2)} + \dots + X_1[k] e^{j\frac{2\pi}{L}c_i} \right\} \tag{4.20}
 \end{aligned}$$

where $e^{-j\frac{2\pi}{L}c_i\ell} = e^{-j\frac{2\pi}{L}c_i(\ell-L)} = e^{j\frac{2\pi}{L}c_i(L-\ell)}$ is used in the last equality. Thus, from

CHAPTER 4. WIDEBAND SPECTRUM SENSING BASED ON SUB-NYQUIST SAMPLING

(4.20), we have the discrete-time form of (4.6):

$$\underbrace{\begin{bmatrix} Y_0[k] \\ Y_1[k] \\ \vdots \\ Y_{P-1}[k] \end{bmatrix}}_{\mathbf{Y}[k]} = \sqrt{\frac{N}{L}} \underbrace{\begin{bmatrix} e^{\frac{j2\pi c_1 0}{L}} & e^{\frac{j2\pi c_1 1}{L}} & \dots & e^{\frac{j2\pi c_1 L-1}{L}} \\ e^{\frac{j2\pi c_2 0}{L}} & e^{\frac{j2\pi c_2 1}{L}} & \dots & e^{\frac{j2\pi c_2 L-1}{L}} \\ \vdots & \vdots & \dots & \vdots \\ e^{\frac{j2\pi c_P 0}{L}} & e^{\frac{j2\pi c_P 1}{L}} & \dots & e^{\frac{j2\pi c_P L-1}{L}} \end{bmatrix}}_{\mathbf{A}} \underbrace{\begin{bmatrix} X_0[k] \\ X_1[k] \\ \vdots \\ X_{L-1}[k] \end{bmatrix}}_{\mathbf{X}[k]}, \quad k=0, 1, \dots, N-1. \quad (4.21)$$

The following definitions are instrumental to deriving the spectrum estimator.

Definition 3: The cyclic cross-spectrum of a signal $z_1(t)$ and $z_2(t)$ is defined as $\mathcal{S}_{z_1 z_2}(\alpha; f) = \mathbb{E} \{Z_1(f) Z_2^*(f - \alpha)\}$ [Antoni, 2007], [Gardner, 1988]. Similarly, the complimentary spectral correlation is defined as $\mathcal{S}_{z_1 z_2}^c(\alpha; f) = \mathbb{E} \{Z_1(f) Z_2(f - \alpha)\}$. Also, the cyclic (auto)-spectrum of a signal $x(t)$ is defined in terms of the spectral correlation as $\mathcal{S}_{xx}(\alpha; f) = \mathbb{E} \{X(f) X^*(f - \alpha)\}$. If the cyclic frequency $\alpha = 0$, the cyclic spectrum reduces to the power spectrum $\mathcal{S}_{xx}(\alpha = 0; f) = \mathbb{E} \{|X(f)|^2\}$. The complimentary cyclic (auto)-spectrum is defined as $\mathcal{S}_{xx}^c(\alpha; f) = \mathbb{E} \{X(f) X(f - \alpha)\}$.

Definition 4: The frequency-smoothed cyclic cross-periodogram is utilized as a consistent estimate of the cyclic cross-spectrum $\mathcal{S}_{z_1 z_2}(\alpha; f)$ [Dandawate and B.Giannakis, 1994], given by

$$\hat{\mathcal{S}}_{Z_1 Z_2}(\alpha; f) \triangleq \frac{1}{N} \sum_{n=0}^{N-1} w_N \left(e^{j2\pi(f - \frac{n}{NT})T} \right) Z_1^{(N)} \left(e^{j2\pi \frac{n}{N}} \right) Z_2^{(N)*} \left(e^{j2\pi(\frac{n}{NT} - \alpha)T} \right),$$

where $Z_i^{(N)}(e^{j2\pi f T}) = \frac{1}{\sqrt{N}} \sum_{n=0}^{N-1} z_i[n] e^{-j2\pi f n T}$ is the finite DTFT of $z_i[n] \triangleq z_i(nT)$, and $w_N(\cdot)$ is the spectral window function given by [Brillinger, 1981]

$$w_N(e^{j2\pi f T}) = \frac{1}{B_N} \sum_{n=-\infty}^{\infty} W \left(\frac{fT + n}{B_N} \right),$$

where $B_N > 0$, and as $N \rightarrow \infty$, $B_N \rightarrow 0$, $B_N N \rightarrow \infty$, and $W(f)$ is an even, real-valued function satisfying $\int_{-\infty}^{\infty} W(f) df = 2\pi$ and $\int_{-\infty}^{\infty} |W(f)| df < \infty$.

In digital implementations, the finite DTFT is replaced by FFT. Correspondingly, the frequency-smoothed cyclic cross-periodogram is given by

$$\hat{\mathcal{S}}_{Z_1 Z_2} \left(\alpha = \frac{m}{NT}; f = \frac{k}{NT} \right) \triangleq \frac{1}{N} \sum_{n=0}^{N-1} w_N[k-n] Z_1[n] Z_2^*[n-m], \quad (4.22)$$

where $w_N[k] \triangleq w_N(e^{j2\pi fT})|_{f=\frac{k}{NT}}$, and $Z_i[k] = Z_i(e^{j2\pi fT})|_{f=\frac{k}{NT}}$. Therefore the frequency-smoothed estimate $\hat{\mathbf{R}}_{\mathbf{Y}}[k]$ of the correlation matrix $\mathbf{R}_{\mathbf{Y}}[k]$ is given by

$$\begin{aligned} \hat{\mathbf{R}}_{\mathbf{Y}}[k] &= \frac{1}{N} \sum_{n=0}^{N-1} w_N[k-n] \mathbf{Y}[n] \mathbf{Y}^H[n] \\ &= \mathbf{A} \left(\frac{1}{N} \sum_{n=0}^{N-1} w_N[k-n] \mathbf{X}[n] \mathbf{X}^H[n] \right) \mathbf{A}^H = \mathbf{A} \hat{\mathbf{R}}_{\mathbf{X}}[k] \mathbf{A}^H. \end{aligned} \quad (4.23)$$

Note that by the consistency of the frequency-smoothed estimator, for large N , the (i, j) -th element of $\hat{\mathbf{R}}_{\mathbf{Y}}[k]$ in (4.23) satisfies

$$\begin{aligned} [\hat{\mathbf{R}}_{\mathbf{Y}}[k]]_{i,j} &\rightarrow \mathbb{E} \{ Y_i[k] Y_j^*[k] \} = \hat{\mathcal{S}}_{Y_i Y_j} \left(\alpha = 0; f = \frac{k}{NLT} \right) \\ &= \mathbb{E} \left\{ Y \left(\frac{i}{LT} + \frac{k}{NLT} \right) Y^* \left(\frac{j}{LT} + \frac{k}{NLT} \right) \right\} = \hat{\mathcal{S}}_{YY} \left(\alpha = \frac{i-j}{LT}; f = \frac{i}{LT} + \frac{k}{NLT} \right). \end{aligned} \quad (4.24)$$

Similarly to (4.15), we can then obtain the power spectrum estimates, given by

$$\hat{\mathbf{r}}_{\mathbf{X}}[k] = \mathbf{Q}^\dagger \hat{\mathbf{r}}_{\mathbf{Y}}[k], \quad k = 0, 1, \dots, N-1, \quad (4.26)$$

where $\hat{\mathbf{r}}_{\mathbf{Y}}[k] = \text{vec}(\hat{\mathbf{R}}_{\mathbf{Y}}[k])$.

Finally the spectral detection is performed to identify the active subbands, which is discussed in the next subsection.

4.4 Spectral Detection

4.4.1 Analysis of Spectrum Estimation Error

Recall that each element of $\hat{\mathbf{r}}_{\mathbf{X}}[k]$ in (4.26) is an estimate of the energy of a frequency bin, based on which we perform spectral detection, i.e., to decide whether this frequency bin is occupied by a primary user or not. In order to perform such detection, we first characterize the statistics of $\hat{\mathbf{r}}_{\mathbf{X}}[k]$, due to the finite sample size.

CHAPTER 4. WIDEBAND SPECTRUM SENSING BASED ON SUB-NYQUIST SAMPLING

We start with the analysis of the estimation error of \mathbf{R}_Y in (4.23). Define the estimation error of the correlation matrix as $\mathbf{E}_Y[k] \triangleq \hat{\mathbf{R}}_Y[k] - \mathbf{R}_Y[k]$ and $\mathbf{e}_Y[k] = \text{vec}(\mathbf{E}_Y[k])$. Denote $\{i\}_P \triangleq \text{mod}(i, P)$ and $[i]_P \triangleq \lfloor i/P \rfloor$. Then we have the following result on the asymptotic distribution of $\mathbf{e}_Y[k]$. The proof is given in Appendix A.

Proposition 5: As $N \rightarrow \infty$, the estimation error $\mathbf{e}_Y[k]$ is asymptotically Gaussian with zero mean, and the covariance matrix $\Sigma_{\mathbf{e}_Y[k]}$ whose (i, j) -th element is given by

$$\begin{aligned} [\Sigma_{\mathbf{e}_Y[k]}]_{ij} &= \mathbb{E} \left\{ [\mathbf{e}_Y[k]]_i [\mathbf{e}_Y[k]]_j^* \right\} \\ &= \mathcal{S}_{Y_{\{i\}_P} Y_{\{j\}_P}} \left(\alpha = 0; f = \frac{k}{NLT} \right) \mathcal{S}_{Y_{[i]_P} Y_{[j]_P}} \left(\alpha = 0; f = \frac{k}{NLT} \right) \\ &\quad + \mathcal{S}_{Y_{\{i\}_P} Y_{[j]_P}}^c \left(\alpha = 0; f = \frac{k}{NLT} \right) \mathcal{S}_{Y_{[i]_P} Y_{\{j\}_P}}^c \left(\alpha = 0; f = \frac{k}{NLT} \right)^* \end{aligned} \quad (4.27)$$

Note that the estimates of $\mathcal{S}_{Y_i Y_j}(\alpha = 0; f = \frac{k}{NLT})$ are contained in $\hat{\mathbf{R}}_Y[k]$ as shown in (4.24). And similarly the estimates of $\mathcal{S}_{Y_i Y_j}^c(\alpha = 0; f = \frac{k}{NLT})$ are contained in $\hat{\mathbf{R}}_Y^c[k] = \frac{1}{N} \sum_{n=0}^{N-1} w_N[k-n] \mathbf{Y}[n] \mathbf{Y}[n]^H$. Once the covariance matrix $\Sigma_{\mathbf{e}_Y[k]}$ is estimated, it then follows from (4.26) that the covariance of the estimator $\hat{\mathbf{r}}_X[k]$ is given by

$$\text{cov}(\hat{\mathbf{r}}_X[k]) = \mathbf{Q}^\dagger \Sigma_{\mathbf{e}_Y[k]} (\mathbf{Q}^\dagger)^H. \quad (4.28)$$

However, the above procedure for estimating $\text{cov}(\hat{\mathbf{r}}_X[k])$ is computationally very intensive. We next develop a simpler estimator that is based directly on $\hat{\mathbf{r}}_X[k]$ itself.

4.4.2 A Simple Error Covariance Estimator

Recall that by denoting $\mathbf{r}_X[k] \triangleq \text{vec}(\mathbf{R}_X[k])$, we have $\mathbf{r}_X[k] = \mathbf{B} \bar{\mathbf{r}}_X[k]$ [cf. (4.12)]. Denote $\mathbf{G} \triangleq \mathbf{B}^\dagger$. Then we have

$$\text{cov}(\bar{\mathbf{r}}_X[k]) = \mathbf{G} \text{cov}(\mathbf{r}_X[k]) \mathbf{G}^H. \quad (4.29)$$

Note that since the Nyquist-rate samples $\mathbf{X}[n]$ are not available, the estimate of $\mathbf{r}_X[k]$, i.e., $\hat{\mathbf{R}}_X[k]$ in (4.23) cannot be obtained. We next show that the error covari-

CHAPTER 4. WIDEBAND SPECTRUM SENSING BASED ON SUB-NYQUIST SAMPLING

ance $\text{cov}(\mathbf{r}_{\mathbf{X}}[k])$ can be estimated using sub-Nyquist samples, if the signal $x(t)$ has a statistical property called proper [Neuser and Massey, 1993b].

Definition 6: A complex random process $x(t)$ is said to be proper if $\mathbb{E}\{x(t)x(t+\tau)\} = 0$, for all τ .

Hence a proper process has a vanishing complementary covariance. For example, most quadrature amplitude modulated (QAM) signals are proper because of a special symmetry in the signaling constellation.

Proposition 6: If the signal $x(t)$ is proper, then $\text{cov}(\mathbf{r}_{\mathbf{X}}[k])$ is a diagonal matrix with the diagonal elements

$$\begin{aligned} [\text{cov}(\mathbf{r}_{\mathbf{X}}[k])]_{i,i} &= \mathbb{E}\left\{\left|X\left(\frac{\{i\}_L}{LT} + \frac{k}{NLT}\right)\right|^2\right\} \mathbb{E}\left\{\left|X\left(\frac{[i]_L}{LT} + \frac{k}{NLT}\right)\right|^2\right\} \\ &= \mathcal{S}_{XX}\left(\alpha=0; f=\frac{\{i\}_L}{LT} + \frac{k}{NLT}\right) \mathcal{S}_{XX}\left(\alpha=0; f=\frac{[i]_L}{LT} + \frac{k}{NLT}\right), 0 \leq i \leq L^2-1 \end{aligned} \quad (4.30)$$

The proof is given in Appendix B. Note that

$$\mathbb{E}\left\{\left|X\left(\frac{\ell}{LT} + \frac{k}{NLT}\right)\right|^2\right\} = [\bar{\mathbf{r}}_{\mathbf{X}}[k]]_{\ell},$$

which is the power spectrum of $x(t)$ at frequency $f = \frac{\ell}{LT} + \frac{k}{NLT}$. Hence the error covariance $\text{cov}(\mathbf{r}_{\mathbf{X}}[k])$ can be approximated using the estimated power spectrum $\hat{\mathbf{r}}_{\mathbf{X}}[k]$ as

$$[\text{cov}(\mathbf{r}_{\mathbf{X}}[k])]_{i,i} \approx \left[\hat{\mathbf{r}}_{\mathbf{X}}[k]\right]_{\{i\}_L} \left[\hat{\mathbf{r}}_{\mathbf{X}}[k]\right]_{[i]_L}, \quad 0 \leq i \leq L^2-1. \quad (4.31)$$

Finally using (4.29), the variance of the i -th element of $\hat{\mathbf{r}}_{\mathbf{X}}[k]$ can then be approximated as

$$\begin{aligned} \text{var}\left\{\left[\hat{\mathbf{r}}_{\mathbf{X}}[k]\right]_i\right\} &= [\mathbf{G} \text{cov}(\mathbf{r}_{\mathbf{X}}[k]) \mathbf{G}^H]_{i,i} \\ &\approx \left[\hat{\mathbf{r}}_{\mathbf{X}}[k]\right]_{\{i\}_L} \left[\hat{\mathbf{r}}_{\mathbf{X}}[k]\right]_{[i]_L} \sum_{j=0}^{L^2-1} |g_{ij}|^2. \end{aligned} \quad (4.32)$$

Note that this estimator is much simpler than that based on (4.28).

4.4.3 Constant-False-Alarm Frequency-bin Energy Detector

Denote the output of the power spectrum estimator as $\hat{\mathbf{r}}_{\mathbf{x}}[k] = [\hat{r}_0[k], \hat{r}_1[k], \dots, \hat{r}_{L-1}[k]]^T$. From the error analysis in the previous subsection, we can formulate the spectrum detection problem as the following binary hypothesis testing problem for each frequency bin,

$$\begin{aligned} H_0 : \quad & \hat{r}_\ell[k] \sim \mathcal{N}(\sigma^2, v_{\ell,k}^2), \\ H_1 : \quad & \hat{r}_\ell[k] \sim \mathcal{N}(P_\ell[k] + \sigma^2, v_{\ell,k}^2), \end{aligned} \quad (4.33)$$

where $v_{\ell,k}^2 = \text{var}\{\hat{\mathbf{r}}_{\mathbf{x}}[k]_\ell\}$. We assume that the noise power level σ^2 is known but the signal power spectrum $P_\ell[k]$ is unknown. We impose a constant false alarm probability P_{FA} across all frequency bins, it then follows that the detection threshold $\theta_\ell[k]$ is given by

$$\theta_\ell[k] = \sqrt{v_{\ell,k}^2} Q^{-1}(P_{\text{FA}}) + \sigma^2, \quad (4.34)$$

where $Q(x) \triangleq \frac{1}{2\pi} \int_x^\infty e^{-\frac{t^2}{2}} dt$. Then the spectral detection for each frequency bin can be performed as follows: declare H_1 if $\hat{r}_\ell[k] > \theta_\ell[k]$ and H_0 otherwise. Finally the active frequency bands can be found by aggregating the frequency bins for which H_1 is declared, which is discussed next.

After performing the spectrum detection on all frequency bins, a binary set $\mathbb{T} = \{T_0, \dots, T_{U-1}\}$, $T_i \in \{0, 1\}$ can be formed, where T_i with $i = (N\ell + k)$, is the detection result on $\hat{r}_\ell[k]$. Further refinement can be performed if more information about the signal is available. For example, similar to [Mishali and Eldar, 2010], the spectral detection results can be refined based on the minimum bandwidth W_{\min} of a subband among all m subbands, and the smallest possible spacing between subbands Δ_{\min} . In particular, denote Δf as the bandwidth of each frequency bin. Then we can perform the following two refinement steps. (1) For any segment of consecutive 1's with length less than $W_{\min}/\Delta f$, flip those 1's to 0's; (2) For any adjacent two segments of consecutive 1's, if there are less than $\Delta_{\min}/\Delta f$ consecutive 0's in between, flip those 0's to 1's.

4.5 Simulation Results

4.5.1 Simulation Setup

We provide three simulation experiments for illustration purpose. In the first experiment, we assume that there are $m = 5$ subbands in the frequency range $\mathcal{F} \in [0, f_{\max}] = [0, 1.5]$ GHz. Hence the Nyquist rate is $f_{\max} = 1/T = 1.5$ GHz. The bandwidths of the subbands are $W_1 = W_2 = W_3 = W_4 = W_5 = 5$ MHz. The central frequencies of the subbands are $f_1 = 750$, $f_2 = 880$, $f_3 = 1000$, $f_4 = 1100$ and $f_5 = 1300$ MHz. To sample the whole band it requires GHz A/D converters which is very difficult and expensive with the current technologies. Fig. 4.3(a) illustrates the power spectrum for the first experiment. The down-sampling factor is chosen as $L = 20$, corresponding to a sub-Nyquist rate of $1/LT = 75$ MHz ($> B_{\max} = 5$ MHz [cf. Proposition 1]). According to Proposition 2, the number of cosets should satisfy $P \geq \lceil \frac{L+1}{2} \rceil = 11$ when university sampling pattern is used. At least, compared with the polyphase implementation of the Nyquist-rate sampling, the number of A/D converters can be saved up to $1 - 11/20 = 45\%$. Based on Property 1 and Proposition 2, the universal sampling pattern $\mathcal{C} = \{0, 1, \dots, P - 1 = 10\}$ is used as a baseline. However, according to Proposition 3, the minimum sampling cosets $P > 5$ are required. Hence, the maximum compression rate is bound to $L/P = 20/5 = 4$ in this example. Note that although a larger L leads to lower sub-Nyquist sampling rate, the number of A/D converters (cosets) will be increased. Thus there is a trade-off between the sub-Nyquist sampling rate and required number of A/D converters. Two FFT sizes are considered, i.e., $N = 12000$ and $N = 24000$, corresponding to the frequency resolution $\Delta f = \frac{1}{NLT} = 12.5$ and 6.25 KHz, respectively, or sensing time $\tau = NLT = 80$ and 160 μ s, respectively. On each subband QPSK symbols $\{d_i[n]\}$ are transmitted, and the root-raised cosine pulse shaping $g_i(t)$ with roll-over factor 0.1 is employed. The Hamming function [Proakis, 1996c] is used as the spectral window function in the estimator (4.23), with a fixed frequency-smoothed bandwidth $B_N = 512.5$ KHz.

CHAPTER 4. WIDEBAND SPECTRUM SENSING BASED ON SUB-NYQUIST SAMPLING

Therefore, corresponding to the sensing time $\tau = 80$ and $160 \mu s$ the spectral window sizes are $512.5/12.5 = 41$, and $512.25/6.25 = 81$ respectively.

In the second experiment, we assume that there are $m = 8$ subbands in the frequency range $\mathcal{F} \in [0, f_{\max}] = [0, 1.5]$ GHz. The bandwidths the subbands are $W_1 = 5$, $W_2 = 5$, $W_3 = 10$, $W_4 = 4$, $W_5 = 4$, $W_6 = 4$, $W_7 = 4$ and $W_8 = 6$ MHz. The central frequencies are $f_1 = 400$, $f_2 = 700$, $f_3 = 750$, $f_4 = 800$, $f_5 = 900$, $f_6 = 1000$, $f_7 = 1100$ and $f_8 = 1300$ MHz. Fig. 4.3(b) illustrates the power spectrum for the second experiment. The down sampling factor is set as $L = 12$. Then the maximum number of cosets satisfies $P \geq \lceil \frac{L+1}{2} \rceil = 7$ and the universal sampling pattern $\mathcal{C} = \{0, 1, \dots, P-1 = 6\}$ is used in this example as baseline. All other simulation parameters are the same as those in the first experiment.

In the third experiment, we assume that there are $m = 6$ subbands in the frequency range $\mathcal{F} \in [0, f_{\max}] = [0, 1.5]$ GHz. The bandwidths the subbands are $W_1 = 50$, $W_2 = 30$, $W_3 = 50$, $W_4 = 50$, $W_5 = 30$, and $W_6 = 20$ MHz. The central frequencies are $f_1 = 200$, $f_2 = 400$, $f_3 = 600$, $f_4 = 750$, $f_5 = 900$ and $f_6 = 1100$ MHz. Fig. 4.3(c) illustrates the power spectrum for the second experiment. The down sampling factor is set as $L = 15$ and $L = 25$ in this example since both $1/(15T) = 75$ MHz and $1/(25T) = 60$ ($> B_{\max} = 50$) MHz. Then the number of cosets satisfies $P \geq \lceil \frac{15+1}{2} \rceil = 8$ for $L = 15$ and $P \geq \lceil \frac{25+1}{2} \rceil = 13$ for $L = 25$, respectively. All other simulation parameters are the same as those in the first experiment.

4.5.2 Multiband Spectrum Sensing Performance

We first illustrate the performance of the spectrum estimator based on the multicosect sampling proposed in Section 3. Fig. 4.4(a) shows the estimated power spectrum corresponding to the first experiment setup where there are $m = 5$ active frequency bands. Clearly there are 5 peaks in the estimated power spectrum. We then apply the spectral detector given in Section 4.3 on each frequency bin, with a target false alarm probability $P_{FA} = 0.01$. The detection results are shown in Fig. 3.4(b). It is seen that

CHAPTER 4. WIDEBAND SPECTRUM SENSING BASED ON SUB-NYQUIST SAMPLING

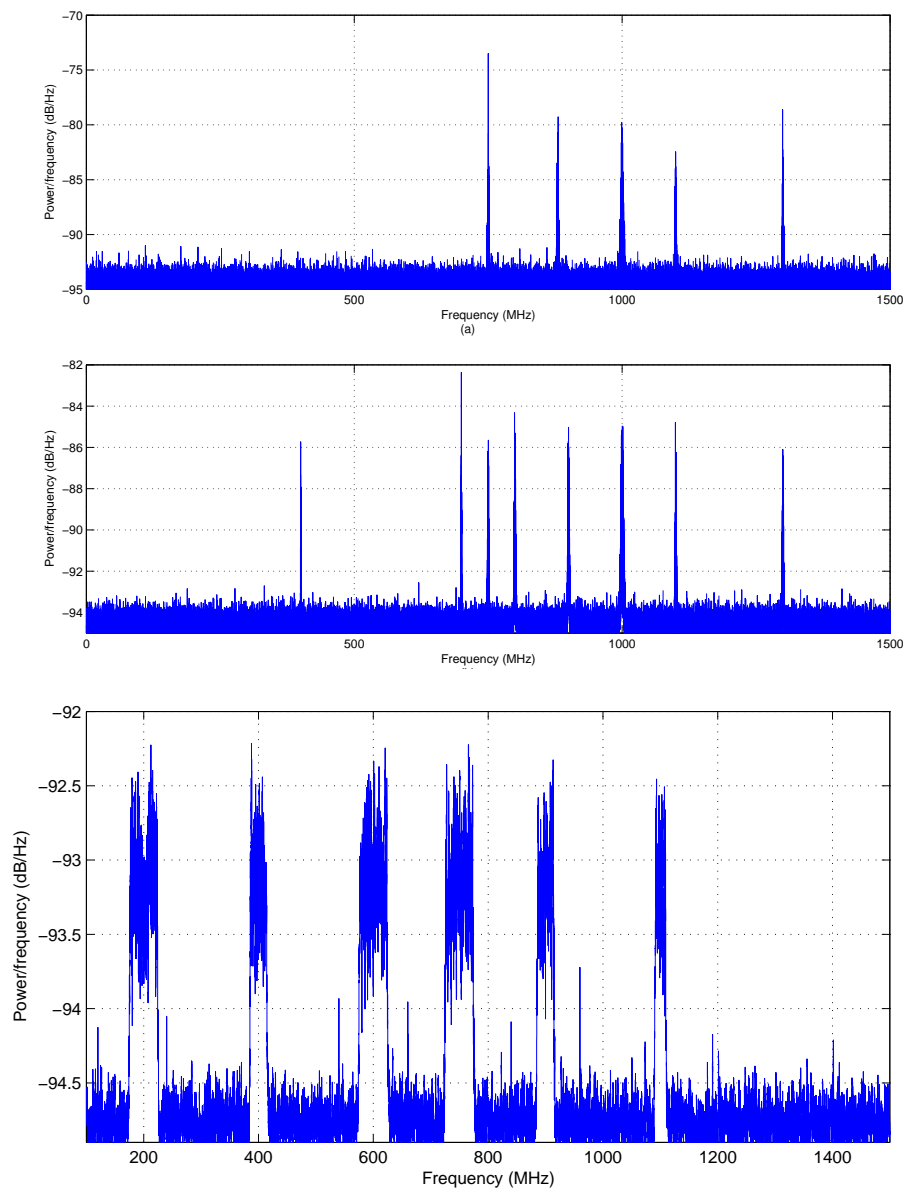


Figure 4.3: (a) The power spectrum for experiment 1 with five subbands. (b) The power spectrum for experiment 2 with eight subbands. (c) The power spectrum for experiment 3 with six subbands.

CHAPTER 4. WIDEBAND SPECTRUM SENSING BASED ON SUB-NYQUIST SAMPLING

there are quite a few false spurs due to the false alarm of the detector. Finally we perform the refinement step using a bandwidth threshold $W_{\min} = 2.5$ MHz, i.e., all detected subbands with bandwidths less than W_{\min} are eliminated. The results after the refinement is shown in Fig. 4.4(c), where it is seen that 5 subbands are identified.

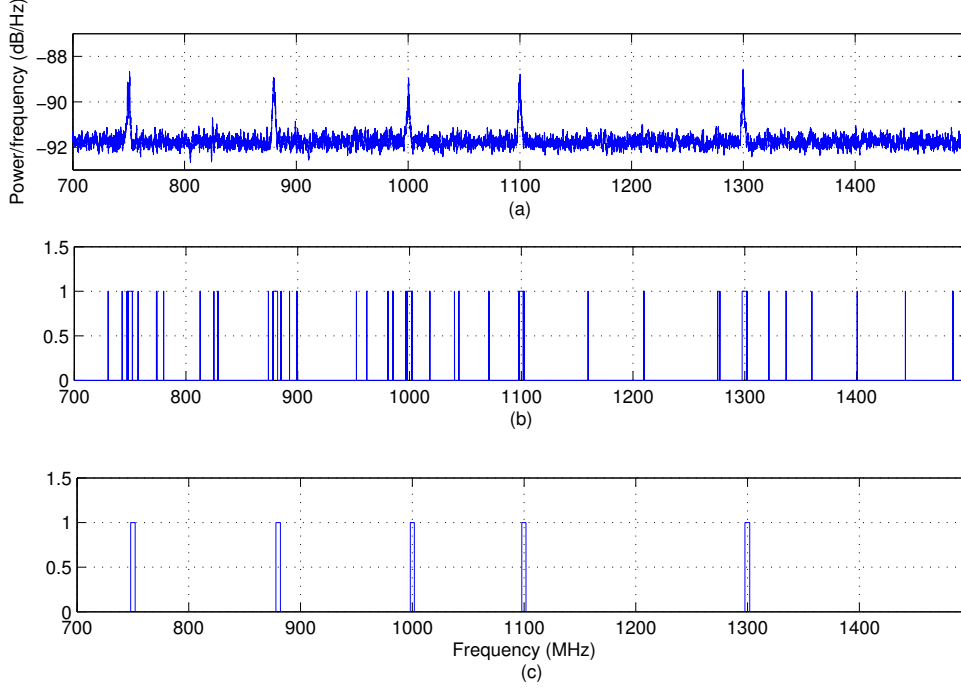


Figure 4.4: (a) The estimated power spectrum for experiment 1. $L = 20, P = 12$. (b) The detection results for the frequency bins using the constant-false alarm detector. (c) The subbands obtained after applying the refinement step on the detection results of (b).

In Fig. 4.5 we plot the actual false alarm probabilities of the frequency-bin detector for both experiment setups. The target is $P_{\text{FA}} = 0.01$. It is seen that the actual false alarm rate fluctuates around the target P_{FA} and hence the proposed detector does achieve constant false alarm. This also demonstrates the effectiveness of the simple variance estimator developed in Section 4.2.

Next we define the multiband normalized spectrum sensing error as the sum of the

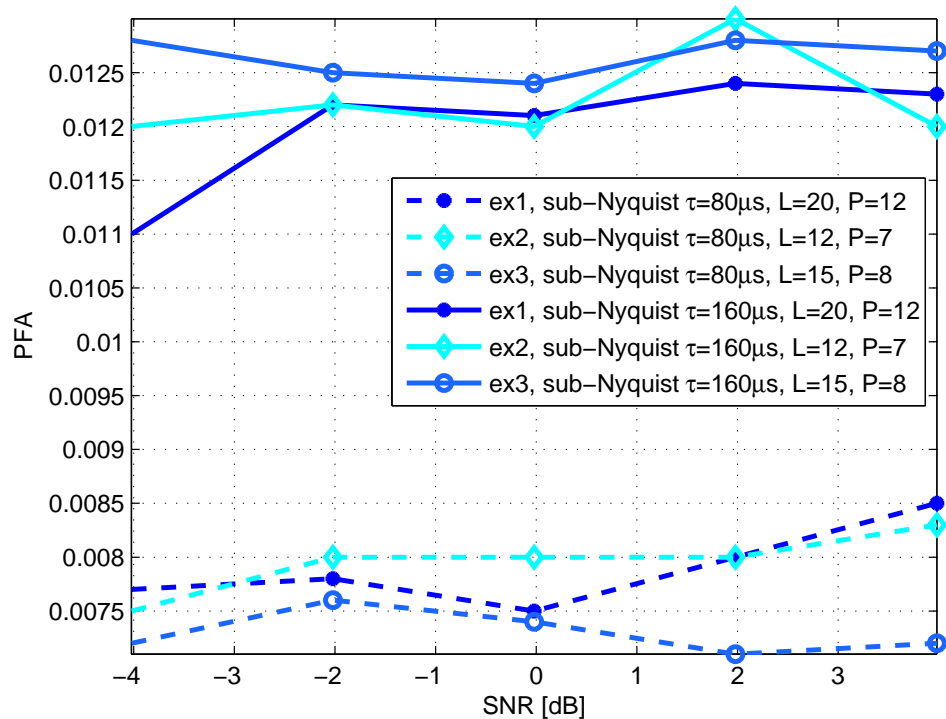


Figure 4.5: The probability of false alarm performance of the frequency bin detector for experiments 1, 2 and 3.

CHAPTER 4. WIDEBAND SPECTRUM SENSING BASED ON SUB-NYQUIST SAMPLING

band boundary estimation errors of all subbands, each normalized by the bandwidth of the corresponding subband, i.e.,

$$\varepsilon \triangleq \sum_{i=1}^m \frac{|\hat{f}_i^l - f_i^l| + |\hat{f}_i^u - f_i^u|}{f_i^u - f_i^l}. \quad (4.35)$$

In Figs. 4.6(a) - (c), the multiband sensing error performances are shown for experiments 1, 2 and 3, respectively. In each figure, we plot the error performances under both the sub-Nyquist sampling ($P < L$) and Nyquist sampling ($P = L$), and for sensing durations of $\tau = 160$ and $\tau = 80 \mu\text{s}$. It is seen that a longer sensing time leads to improved sensing accuracy, because increased sensing time results in better estimation of $\hat{\mathbf{R}}_{\mathbf{Y}}[k]$ in (4.23). The performance loss by the sub-Nyquist-rate sampling compared to the Nyquist-rate sampling is due to the noisier estimate of $\hat{\mathbf{R}}_{\mathbf{Y}}[k]$. This performance gap can be reduced by increasing the sensing time. In the following two figures, i.e., Fig. 4.7 and Fig. 4.8 shows the spectrum sensing error performance for the second and third experiment with a range of number of cosets P corresponding to different compression ratios are simulated. To demonstrate higher compression ratio in this example, the down-sampling factor $L = 50$ is selected for second experiment. According to Proposition 3, the minimum number of cosets $P = 8$ can satisfy the rank $L = 50$ and it is corresponding to maximum compression ratio is equal to $50/8 = 6.25$ in this case. The sensing time is fixed $\tau = 160 \mu\text{s}$ for Fig. 3.6 and the range of number of cosets $P = 8, 12, 16, 20, 24$ are simulated which are corresponding to the compression ratio is from 6.25, 4.167, 3.125, 2.5, 2.08, respectively. The sampling pattern for $P = 8, 12, 16, 20, 24$ is obtained by using blind search method. Here, for $P = 8$, the sampling pattern $\mathcal{C} = \{20, 24, 30, 31, 40, 43, 45, 48\}$ is used, for $P = 12$, the sampling pattern $\mathcal{C} = \{3, 12, 13, 14, 15, 28, 33, 38, 42, 44, 45, 47\}$ is used, for $P = 16$, the sampling pattern $\mathcal{C} = \{1, 8, 13, 17, 20, 22, 23, 24, 28, 30, 31, 32, 36, 42, 45, 49\}$ is used, and for $P = 24$, the sampling pattern $\mathcal{C} = \{0, 4, 8, 9, 10, 13, 16, 19, 20, 22, 23, 26, 27, 28, 35, 36, 37, 38, 43, 44, 45, 46, 47, 48\}$ is used. From Fig. 4.7, it is seen that when P increases, the performance improves. This is because we observe the variance in (4.32) is getting higher

CHAPTER 4. WIDEBAND SPECTRUM SENSING BASED ON SUB-NYQUIST SAMPLING

when lower compression ratio is used to maintain the CFA. Hence, the compression ratio is an engineering trade-off with the detection performance for compressive spectrum sensing. In Fig. 4.8, the down sampling rate $L = 15$ are $L = 20$ used for evaluation. So according to Proposition 3, the minimum number of cosets $P = 5$ can satisfy the full rank of \mathbf{Q} matrix for $L = 15$ and the compression ratio is equal to $15/5 = 3$ in this case. From Proposition 4, the sampling pattern $\mathcal{C} = \{0, 1, 2, 3, 7\}$, and $\mathcal{C} = \{0, 1, 2, 5, 8\}$ [Pal and Vaidyanathan, 2010] for two-level are selected to guarantee \mathbf{Q} matrix having full rank as well. The sensing time is set to $\tau = 160 \mu\text{s}$ in this simulation. When $L = 25$, the minimum number of cosets $P = 6$ can satisfy the full rank of \mathbf{Q} matrix and the corresponding compression ratio is equal to $25/6 = 4.167$. If we choose the sampling pattern from Proposition 4 then the number of cosets $P = 8$ are required and the corresponding compression ratio is equal to $25/8 = 3.12$. If the sampling pattern is chosen from two-level methods then the number of cosets $P = 7$ are required and the corresponding compression ratio is equal to $25/7 = 3.57$. For minimum number of cosets $P = 6$ case, the sampling pattern $\mathcal{C} = \{0, 1, 2, 3, 8, 12\}$ is used. For number of cosets $P = 8$ case, the sampling pattern $\mathcal{C} = \{0, 1, 2, 3, 4, 5, 6, 13\}$ is used. For number of cosets $P = 7$, i.e., two-level case, the sampling pattern $\mathcal{C} = \{0, 1, 2, 3, 7, 11, 15\}$ is used. Similar to previous experiment show in Fig. 4.7, the spectrum detection performance is enhanced when compression ratio is getting lower. The detection performance among Proposition 4, two-level and minimum number of cosets are similar when L is small.

4.6 Conclusions

We have proposed a new technique for multiband spectrum sensing using sub-Nyquist sampling. The basic procedure of the proposed method involves multicorset sampling of the signal, followed by power spectrum estimation and energy detection on the frequency bins. The only prior knowledge needed is an upper bound on the number of

CHAPTER 4. WIDEBAND SPECTRUM SENSING BASED ON SUB-NYQUIST SAMPLING

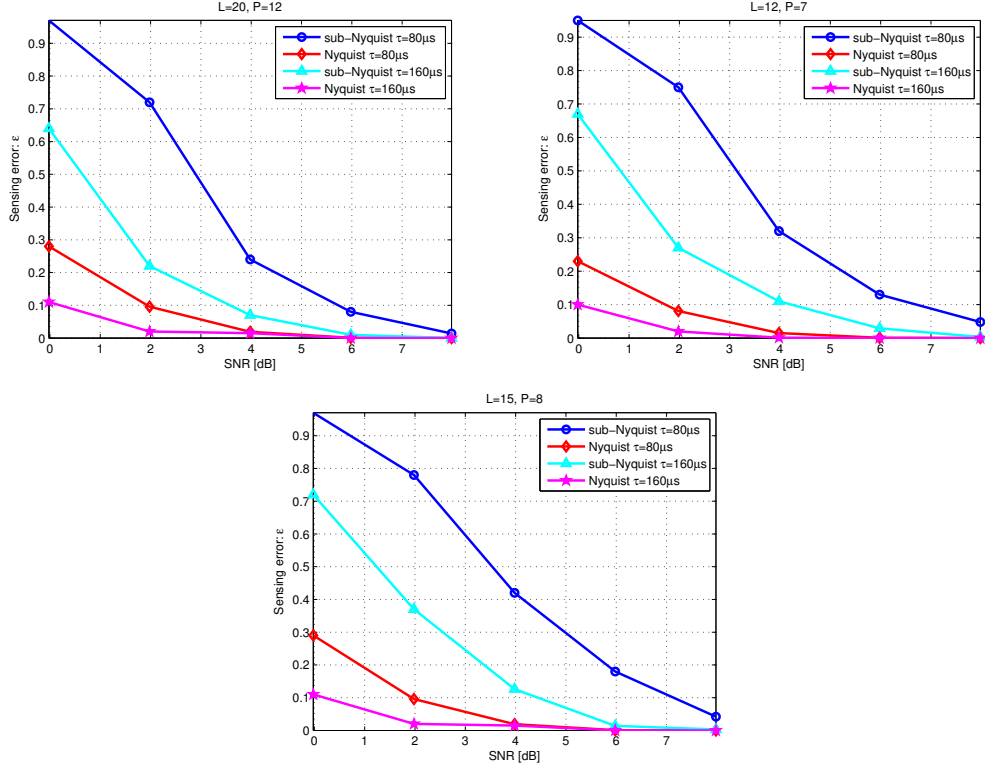


Figure 4.6: The multiband spectrum sensing performance as a function of SNR. Sensing times $\tau = 160$ and $\tau = 80 \mu\text{s}$ are considered. (a) experiment 1: $L=20$, $P=12$. (b) experiment 2: $L=12$, $P=7$. (c) experiment 3: $L=15$, $P=8$.

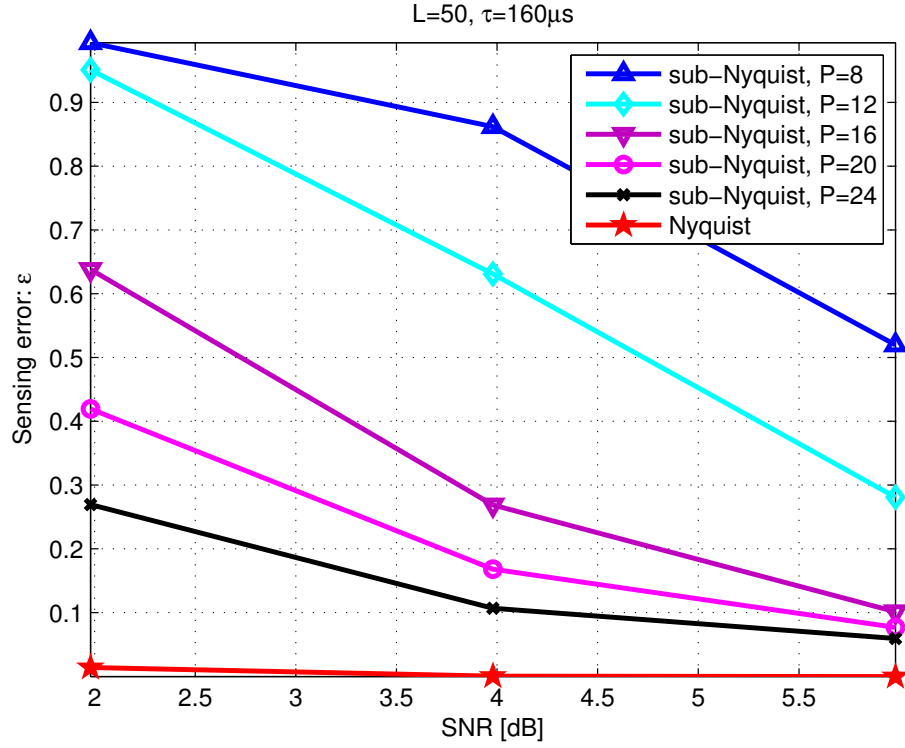


Figure 4.7: The multiband spectrum sensing performance for experiment 2 with different $P = 8, 12, 16, 20, 24$ cosets which are corresponding to the compression ratio from 6.25, 4.167, 3.125, 2.5, 2.08, when $L = 50, \tau = 160 \mu\text{s}$.

CHAPTER 4. WIDEBAND SPECTRUM SENSING BASED ON SUB-NYQUIST SAMPLING

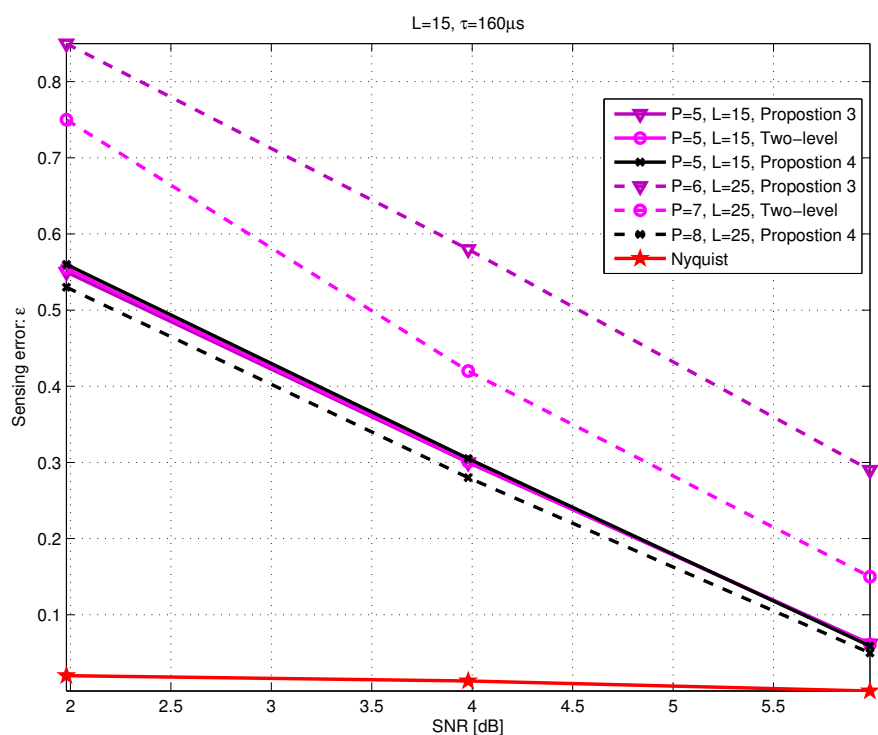


Figure 4.8: The multiband spectrum sensing performance for experiment 3 with different sampling patterns with $L = 15$ and $L = 25$, $\tau = 160 \mu\text{s}$.

CHAPTER 4. WIDEBAND SPECTRUM SENSING BASED ON SUB-NYQUIST SAMPLING

active subbands in the frequency range of interest. And the proposed multiband sensing algorithm outputs the number of active subbands and the location of each active subband. The key ingredients of the proposed wideband sensing algorithm, including a power spectrum estimator based on multicoset sampling, and a constant-false-alarm frequency-bin energy detector, are developed theoretically; and their effectiveness is demonstrated by simulations. Compared with the polyphase implementation of the Nyquist sampling approach, for a large down-sampling factor, the new method can reduce the sampling rate by a factor of at least about 2, which translates into the same factor of saving in terms of the number of A/D converters needed at the front end.

Appendix A: Proof of Proposition 5

We first introduce the following definition.

Definition 6: Given the complex signals $z_i(t)$ and $z_j(t)$, their cyclic cross-periodogram is defined as

$$I_{Z_i Z_j}^{(N)}(\alpha; f) \triangleq \frac{1}{N} Z_i^{(N)}(e^{j2\pi f T}) Z_j^{(N)*}(e^{j2\pi(f-\alpha)T}),$$

and their complimentary cyclic cross-periodogram is defined as

$$C_{Z_i Z_j}^{(N)}(\alpha; f) \triangleq \frac{1}{N} Z_i^{(N)}(e^{j2\pi f T}) Z_j^{(N)}(e^{j2\pi(f-\alpha)T}),$$

where $Z_i^{(N)}(e^{j2\pi f T}) \triangleq \frac{1}{\sqrt{N}} \sum_{n=0}^{N-1} z_i[n] e^{-j2\pi f n T}$, and $z_i[n] \triangleq z_i(nT)$.

The following Lemma is useful for the proofs of Proposition 3 and 4.

Lemma 1 (Cross-covariance of the cyclic cross-periodogram) If the 4-th order cyclic cumulant spectrum $\mathcal{S}_{Z_1 Z_2 Z_3 Z_4}(\alpha; f_1, f_2, f_3)$ exists and is finite, then the cross-covariance of the cyclic cross-periodogram is asymptotically

$$\begin{aligned} & \lim_{N \rightarrow \infty} \text{cov} \left\{ I_{Z_1 Z_2}^{(N)}(\alpha_1; f_1), I_{Z_3 Z_4}^{(N)}(\alpha_2; f_2) \right\} \\ = & S_{Z_1 Z_3}(f_1 - f_2; f_1) S_{Z_4 Z_2}(f_2 - \alpha_2 - f_1 + \alpha_1; f_2 - \alpha_2) \\ & + S_{Z_1 Z_4}^c(f_1 - f_2 + \alpha_2; f_1) S_{Z_2 Z_3}^{c*}(f_1 - f_2 - \alpha_1; f_1 - \alpha_1). \end{aligned} \quad (4.36)$$

CHAPTER 4. WIDEBAND SPECTRUM SENSING BASED ON SUB-NYQUIST SAMPLING

Proof: The asymptotic cross-covariance of the cyclic cross-periodogram for real signals is given in Theorem 1 in [Sadler and Dandawate, 1997]. Here we extend it to complex signals. According to Theorem 2.3.2 in [Brillinger, 1981], the cross-covariance can be evaluated as

$$\begin{aligned}
& \text{cov} \left\{ I_{Z_1 Z_2}^{(N)}(\alpha_1; f_1), I_{Z_3 Z_4}^{(N)}(\alpha_2; f_2) \right\} = \text{cum} \left\{ I_{Z_1 Z_2}^{(N)}(\alpha_1; f_1), \left(I_{Z_3 Z_4}^{(N)}(\alpha_2; f_2) \right)^* \right\} \\
&= \frac{1}{N^2} \text{cum} \left\{ Z_1^{(N)}(e^{j2\pi f_1 T}) Z_2^{(N)*}(e^{j2\pi(f_1 - \alpha_1)T}), \left(Z_3^{(N)}(e^{j2\pi f_2 T}) Z_4^{(N)*}(e^{j2\pi(f_2 - \alpha_2)T}) \right)^* \right\} \\
&= \frac{1}{N^2} \text{cum} \left\{ Z_1^{(N)}(e^{j2\pi f_1 T}), Z_2^{(N)*}(e^{j2\pi(f_1 - \alpha_1)T}), Z_3^{(N)*}(e^{j2\pi f_2 T}), Z_4^{(N)}(e^{j2\pi(f_2 - \alpha_2)T}) \right\} \\
&\quad + \frac{1}{N^2} \text{cum} \left\{ Z_1^{(N)}(e^{j2\pi f_1 T}), Z_3^{(N)*}(e^{j2\pi f_2 T}) \right\} \cdot \text{cum} \left\{ Z_2^{(N)*}(e^{j2\pi(f_1 - \alpha_1)T}), Z_4^{(N)}(e^{j2\pi(f_2 - \alpha_2)T}) \right\} \\
&\quad + \frac{1}{N^2} \text{cum} \left\{ Z_1^{(N)}(e^{j2\pi f_1 T}), Z_4^{(N)}(e^{j2\pi(f_2 - \alpha_2)T}) \right\} \cdot \text{cum} \left\{ Z_3^{(N)*}(e^{j2\pi f_2 T}), Z_2^{(N)*}(e^{j2\pi(f_1 - \alpha_1)T}) \right\} \\
&= \frac{1}{N^2} \text{cum} \left\{ Z_1^{(N)}(e^{j2\pi f_1 T}), Z_2^{(N)*}(e^{j2\pi(f_1 - \alpha_1)T}), Z_3^{(N)*}(e^{j2\pi f_2 T}), Z_4^{(N)}(e^{j2\pi(f_2 - \alpha_2)T}) \right\} \\
&\quad + \frac{1}{N} \text{cum} \left\{ Z_1^{(N)}(e^{j2\pi f_1 T}), Z_3^{(N)*}(e^{j2\pi f_2 T}) \right\} \cdot \frac{1}{N} \text{cum} \left\{ Z_4^{(N)}(e^{j2\pi(f_2 - \alpha_2)T}), Z_2^{(N)*}(e^{j2\pi(f_1 - \alpha_1)T}) \right\} \\
&\quad + \frac{1}{N} \text{cum} \left\{ Z_1^{(N)}(e^{j2\pi f_1 T}), Z_4^{(N)}(e^{j2\pi(f_2 - \alpha_2)T}) \right\} \cdot \frac{1}{N} \text{cum} \left\{ Z_2^{(N)*}(e^{j2\pi(f_1 - \alpha_1)T}), Z_3^{(N)*}(e^{j2\pi f_2 T}) \right\}.
\end{aligned} \tag{4.37}$$

From the proof of Theorem 1 in [Sadler and Dandawate, 1997], we have

$$\begin{aligned}
& \frac{1}{N} \text{cum} \left\{ Z_1^{(N)}(e^{j2\pi f_1 T}), Z_2^{(N)*}(e^{j2\pi(f_1 - \alpha_1)T}), Z_3^{(N)*}(e^{j2\pi f_2 T}), Z_4^{(N)}(e^{j2\pi(f_2 - \alpha_2)T}) \right\} \\
& \rightarrow \mathcal{S}_{Z_1 Z_2 Z_3 Z_4}(\alpha_1 - \alpha_2; f_1, \alpha_1 - f_1, -f_2).
\end{aligned}$$

Since $\mathcal{S}_{Z_1 Z_2 Z_3 Z_4}(\alpha_1 - \alpha_2; f_1, \alpha_1 - f_1, -f_2)$ exists and is finite, the first term in (4.37) goes to zero when $N \rightarrow \infty$. Moreover, we have $\frac{1}{N} \text{cum} \left\{ Z_1^{(N)}(e^{j2\pi f_1 T}), Z_3^{(N)*}(e^{j2\pi f_2 T}) \right\} \rightarrow S_{Z_1 Z_3}(f_1 - f_2; f_1)$, $\frac{1}{N} \text{cum} \left\{ Z_4^{(N)}(e^{j2\pi(f_2 - \alpha_2)T}), Z_2^{(N)*}(e^{j2\pi(f_1 - \alpha_1)T}) \right\} \rightarrow S_{Z_4 Z_2}(f_2 - \alpha_2 - f_1 + \alpha_1; f_2 - \alpha_2)$, $\frac{1}{N} \text{cum} \left\{ Z_1^{(N)}(e^{j2\pi f_1 T}), Z_4^{(N)}(e^{j2\pi(f_2 - \alpha_2)T}) \right\} \rightarrow S_{Z_1 Z_4}^c(f_1 - f_2 + \alpha_2; f_1)$, and $\frac{1}{N} \text{cum} \left\{ Z_2^{(N)*}(e^{j2\pi(f_1 - \alpha_1)T}), Z_3^{(N)*}(e^{j2\pi f_2 T}) \right\} \rightarrow S_{Z_2 Z_3}^{c*}(f_1 - f_2 - \alpha_1; f_1 - \alpha_1)$.

Thus (4.36) is obtained □

Now we proceed to prove Proposition 3. Note that

$$\left[\mathbf{r}_Y[k] \right]_i = \left[\mathbf{R}_Y[k] \right]_{(\{i\}_P, [i]_P)} = \mathbb{E} \left\{ Y_{\{i\}_P}[k] Y_{[i]_P}^*[k] \right\} = \mathcal{S}_{Y_{\{i\}_P} Y_{[i]_P}} \left(\alpha = 0; f = \frac{k}{NLT} \right). \tag{4.38}$$

CHAPTER 4. WIDEBAND SPECTRUM SENSING BASED ON SUB-NYQUIST SAMPLING

It is shown in [Dandawate and B.Giannakis, 1994] that the frequency-smoothed cyclic cross-periodogram defined in Definition 4 is asymptotically Gaussian, unbiased and consistent. Therefore we have for large N , $\mathbb{E}\{\mathbf{e}_Y[k]\} = \mathbf{0}$. Using Lemma 1, for large N , the covariance of $\mathbf{e}_Y[k]$ is given by

$$\begin{aligned}
& \mathbb{E}\left\{\left[\mathbf{e}_Y[k]\right]_i \left[\mathbf{e}_Y[k]\right]_j^* \right\} = \text{cov}\left\{Y_{\{i\}_P}[k]Y_{[i]_P}^*[k], Y_{\{j\}_P}[k]Y_{[j]_P}^*[k]\right\} \\
&= \text{cov}\left\{S_{Y_{\{i\}_P}Y_{[i]_P}}\left(\alpha=0; f=\frac{k}{NLT}\right), S_{Y_{\{j\}_P}Y_{[j]_P}}\left(\alpha=0; f=\frac{k}{NLT}\right)\right\} \\
&= S_{Y_{\{i\}_P}Y_{\{j\}_P}}\left(0; f=\frac{k}{NLT}\right) S_{Y_{[i]_P}Y_{[j]_P}}\left(0; f=\frac{k}{NLT}\right) \\
&+ S_{Y_{\{i\}_P}Y_{[j]_P}}^c\left(0; f=\frac{k}{NLT}\right) S_{Y_{[i]_P}Y_{\{j\}_P}}^{c*}\left(0; f=\frac{k}{NLT}\right). \tag{4.39}
\end{aligned}$$

□

Appendix B: Proof of Proposition 6

Using Lemma 1, the error covariance of $\mathbf{r}_X[k]$ can be evaluated in terms of the cyclic spectrum as

$$\begin{aligned}
& \left[\text{cov}\{\mathbf{r}_X[k]\}\right]_{i,j} = \text{cov}\left\{X_{\{i\}_P}[k]X_{[i]_P}^*[k], X_{\{j\}_P}[k]X_{[j]_P}^*[k]\right\} \\
&= S_{XX}\left(\alpha=\frac{\{i\}_L-\{j\}_L}{LT}; f=\frac{\{i\}_L}{LT}+\frac{k}{NLT}\right) S_{XX}\left(\alpha=\frac{-[i]_L+[j]_L}{LT}; f=\frac{[j]_L}{LT}+\frac{k}{NLT}\right) \\
&+ \underbrace{S_{XX}^c\left(\alpha=\frac{\{i\}_L-[j]_L}{LT}; f=\frac{\{i\}_L}{LT}+\frac{k}{NLT}\right)}_0 \underbrace{S_{XX}^{c*}\left(\alpha=\frac{-\{j\}_L+[j]_L}{LT}; f=\frac{[i]_L}{LT}+\frac{k}{NLT}\right)}_0, \tag{4.40}
\end{aligned}$$

where we have used the fact that for a proper signal $x(t)$, the complementary cyclic spectrum is zero, i.e. $S_{XX}^c(\alpha; f) = 0$.

Moreover, for any (i, j) such that $\{i\}_L \neq \{j\}_L$ or $[i]_L \neq [j]_L$, we have $i \neq j$. When $i \neq j$, the terms in (4.40) are the cross-correlations between $X\left(\frac{\{i\}_L}{LT}+\frac{k}{NLT}\right)$ and $X\left(\frac{\{j\}_L}{LT}+\frac{k}{NLT}\right)$, which from the proof of the Proposition 1, must be from distinct subbands. Thus when $i \neq j$, (4.40) is zero because it is assumed that signals from different subbands are independent and zero-mean. □

Chapter 5

Beamformed Millimeter-Wave Full-dimensional MIMO Channel Estimation Based on Atomic Norm Minimization

5.1 Introduction

Millimeter wave (mmWave) communications have been proposed as an important physical-layer technology for the 5th generation (5G) mobile networks to provide multi-gigabit services [Rappaport *et al.*, 2013]. Two prominent features of the mmWave spectrum are the massive bandwidth available and the tiny wavelengths compared to conventional microwave bands, thus enabling dozens or even hundreds of antenna elements to be accommodated at communication link ends within a reasonable physical form factor. This suggests that massive MIMO and mmWave technologies should be considered jointly to provide higher data rates and spectrum efficiency. In particular, the mmWave full-dimensional MIMO (FD-MIMO) systems [Cheng *et al.*, 2014],[Hur *et al.*, 2013] employ uniform or non-uniform planar arrays at both the

CHAPTER 5. BEAMFORMED MILLIMETER-WAVE FULL-DIMENSIONAL MIMO CHANNEL ESTIMATION BASED ON ATOMIC NORM MINIMIZATION

basestation (BS) and user equipment (UE) and provide an extra degree of freedom in the elevation-angle domain. Users can now be distinguished not only by their AoAs in the azimuth domain but also by their AoDs in the elevation domain [Nam *et al.*, 2013]. In this paper, we consider channel estimation for mmWave FD-MIMO systems that simultaneously support both azimuth and elevation beamforming.

The mmWave band channel is significantly different from those in sub-6GHz bands. The key challenge in designing new radio access technologies for mmWave is how to overcome the much larger path-loss and reduce blockage probability. To that end, beamforming is essential in combating the serve path-loss for wireless system operating in mmWave bands [Kutty and Sen, 2016]. However, to estimate the full channel state information (CSI) under beamformed FD-MIMO is somehow challenging because the receiver typically only obtains the beamformed CSI instead of full CSI. To address this issue, fast beam scanning and searching techniques have been extensively studied [Hur *et al.*, 2013; Wang, 2009]. The objective of beam scanning is to search for the best beamformer-combiner pair by letting the transmitter and receiver scan the adaptive sounding beams chosen from pre-determined sounding beam codebooks. However, the exhaustive search may be hampered by the high training overhead in practice and suffer from low spectral efficiency. Another approach is to estimate the mmWave channel or its associated parameters, by exploiting the sparse scattering nature of the mmWave channels [Samimi and Rappaport, 2016],[Thomas *et al.*, 2014],[Ayach *et al.*, 2014], that is, mmWave channel estimation can be formulated as a sparse signal recovery problem [Alkhateeb *et al.*, 2014], [Alkhateeb *et al.*, 2015], [Guo *et al.*, 2017], [Sun and Rappaport, 2017] and solved using the compressive sensing (CS)-based approach [Donoho, 2006b]. In the CS-based approach, a sensing matrix needs to be constructed first, by dividing certain parameter space into a finite number of grids and thus the channel estimation performance is limited by the grid resolution. On the other hand, in [Rappaport *et al.*, 2014], a subspace-based mmWave MIMO channel estimation method that makes use of the MUSIC algorithm is pro-

CHAPTER 5. BEAMFORMED MILLIMETER-WAVE FULL-DIMENSIONAL MIMO CHANNEL ESTIMATION BASED ON ATOMIC NORM MINIMIZATION

posed. A 2D-MUSIC algorithm for beamformed mmWave MIMO channel estimation is proposed in [Guo *et al.*, 2017] to further enhance the channel estimation performance. The MUSIC algorithm is able to identify multiple paths with high resolution but it is sensitive to antenna position, gain, and phase errors.

Recently, the atomic norm minimization [Tang *et al.*, 2013] has been applied to many signal processing problems such as super-resolution frequency estimation [Bhaskar *et al.*, 2013b], [Steinwandt *et al.*, 2016], spectral estimation [Bhaskar *et al.*, 2013a], AoA estimation, [Zhang *et al.*, 2017; Tian *et al.*, 2017], uplink multiuser MIMO channel estimation [Zhang *et al.*, 2015] and linear system identification [Shah *et al.*, 2012]. Under certain conditions, atomic norm minimization can achieve exact frequency localization, avoiding the effects of basis mismatch which can plague grid-based CS techniques. Different from the prior works such as CS-based and subspace-based channel estimation methods mentioned above, we formulate the mmWave FD-MIMO channel estimation as an atomic norm minimization problem. Unlike [Zhang *et al.*, 2015] that considers uplink multiuser MIMO channel estimation, in which the uniform linear array is assumed and only the AoA parameter is estimated, in this paper, we consider the mmWave beamformed FD-MIMO channel, which involves the estimation of both AoA and AoD. Hence, instead of one-dimensional (1D) atomic norm minimization, our problem is formulated as a four-dimensional (4D) atomic norm minimization problem. The 4D atomic norm minimization can be transformed into semi-definite program (SDP) which is of high dimensional and involves block Toeplitz matrices, leading to very high computational complexity. Therefore, we introduce a 4D atomic norm approximation method to reduce the computational complexity and an efficient algorithm based on the alternating direction method of multipliers (ADMM) is derived.

Recently, non-uniform planar array (NUPA) has attracted more interest due to its ability in reducing sidelobes and antenna correlation [Liu *et al.*, 2017; Wang *et al.*, 2016]. NUPA can potentially increase the achievable multiplexing gain of mmWave

CHAPTER 5. BEAMFORMED MILLIMETER-WAVE FULL-DIMENSIONAL MIMO CHANNEL ESTIMATION BASED ON ATOMIC NORM MINIMIZATION

FD-MIMO beamforming. However, the corresponding atomic norm minimization problem cannot be transformed into an SDP when the antennas are not uniformly placed [Tang *et al.*, 2013]. Hence, we propose a gradient descent method for mmWave FD-MIMO channel estimation with NUPA.

The remainder of the paper is organized as follows. In Section 5.2, the mmWave beamformed FD-MIMO channel model is introduced. In Section 5.3, we formulate the mmWave FD-MIMO channel estimation as an atomic norm minimization problem for the case of UPA. In Section 5.4, we develop efficient algorithms for implementing the proposed atomic-norm-based channel estimator. In Section 5.5, we consider the case of NUPA and provide the formulation and algorithm for the atomic-norm-based channel estimator. In Section 5.6, simulation results are provided. Finally, Section 5.7 concludes the paper.

5.2 System Descriptions and Background

5.2.1 System and Channel Models

We consider a mmWave FD-MIMO system with M receive antennas and N transmit antennas that simultaneously supports elevation and azimuth beamforming. The channel matrix can be expressed in terms of transmit and receive array responses [Ayach *et al.*, 2014]:

$$\mathbf{H} = \mathbf{B}\mathbf{\Sigma}\mathbf{A}^H = \sum_{l=1}^L \sigma_l \mathbf{b}(\mathbf{f}_l) \mathbf{a}(\mathbf{g}_l)^H, \quad (5.1)$$

where $(\cdot)^H$ denotes the Hermitian transpose; the matrix

$$\mathbf{\Sigma} = \text{diag}(\boldsymbol{\sigma}) = \text{diag}\left([\sigma_1 \ \sigma_2 \ \dots \ \sigma_L]^T\right)$$

is a diagonal matrix with each $\sigma_l \in \mathbb{C}$ denoting the l -th multipath gain; L denotes the number of paths; the matrices $\mathbf{B} = [\mathbf{b}(\mathbf{f}_1) \ \dots \ \mathbf{b}(\mathbf{f}_L)]$ and $\mathbf{A} = [\mathbf{a}(\mathbf{g}_1) \ \dots \ \mathbf{a}(\mathbf{g}_L)]$ denote the steering responses of the receive and transmit arrays, respectively. For a

CHAPTER 5. BEAMFORMED MILLIMETER-WAVE FULL-DIMENSIONAL MIMO CHANNEL ESTIMATION BASED ON ATOMIC NORM MINIMIZATION

linear array with half-wavelength separation of adjacent antenna elements, the array response is in the form of a uniformly sampled complex sinusoid with frequency $x \in [-\frac{1}{2}, \frac{1}{2})$:

$$\mathbf{c}_n(x) = \frac{1}{\sqrt{n}} [1 \ e^{j2\pi x} \dots e^{j2\pi(n-1)x}]^T \in \mathbb{C}^{n \times 1}. \quad (5.2)$$

We assume that both the transmitter (Tx) and receiver (Rx) are equipped with uniformly spaced planar antenna arrays (UPA)s [Choi *et al.*, 2015; Han *et al.*, 2014], each with half-wavelength antenna element separations along the elevation-and-azimuth-axis. Then the Tx and Rx array responses can be expressed as [Han *et al.*, 2014]

$$\mathbf{a}(\mathbf{g}_l) = \mathbf{c}_{N_1}(g_{l,1}) \otimes \mathbf{c}_{N_2}(g_{l,2}), \quad (5.3)$$

$$\mathbf{b}(\mathbf{f}_l) = \mathbf{c}_{M_1}(f_{l,1}) \otimes \mathbf{c}_{M_2}(f_{l,2}), \quad (5.4)$$

with

$$\mathbf{g}_l = \left\{ g_{l,1} = \frac{1}{2} \sin(\vartheta_l) \cos(\varphi_l), g_{l,2} = \frac{1}{2} \cos(\vartheta_l) \right\}, \quad (5.5)$$

$$\mathbf{f}_l = \left\{ f_{l,1} = \frac{1}{2} \sin(\theta_l) \cos(\phi_l), f_{l,2} = \frac{1}{2} \cos(\theta_l) \right\}, \quad (5.6)$$

where \otimes denotes the Kronecker product; ϑ_l, φ_l denote elevation and azimuth angles of the angle of departure (AoD) of the l -th path, respectively; and θ_l, ϕ_l denote elevation and azimuth angles of the angle of arrival (AoA), respectively. Here, N_1, N_2 denote the numbers of elevation and azimuth transmit antennas, respectively, and the total number of transmit antennas is $N = N_1 N_2$. Similarly, M_1, M_2 denote the numbers of elevation and azimuth receive antennas, respectively, and the total number of receive antennas is $M = M_1 M_2$. For the UPA configuration, it can resolve the AoA and AoD in 360° range, thereby $\vartheta_l, \theta_l, \varphi_l, \phi_l \in [-\pi, \pi]$ and $g_{l,1} = \frac{1}{2} \sin(\vartheta_l) \cos(\varphi_l) \in [-\frac{1}{2}, \frac{1}{2})$, $g_{l,2} = \frac{1}{2} \cos(\vartheta_l) \in [-\frac{1}{2}, \frac{1}{2})$, $f_{l,1} = \frac{1}{2} \sin(\theta_l) \cos(\phi_l) \in [-\frac{1}{2}, \frac{1}{2})$, $f_{l,2} = \frac{1}{2} \cos(\theta_l) \in [-\frac{1}{2}, \frac{1}{2})$.

To estimate the channel matrix, the transmitter transmits P distinct beams during P successive time slots. i.e., in the p -th time slot, the beamforming vector $\mathbf{p}_p \in$

CHAPTER 5. BEAMFORMED MILLIMETER-WAVE FULL-DIMENSIONAL MIMO CHANNEL ESTIMATION BASED ON ATOMIC NORM MINIMIZATION

$\mathbb{C}^{N \times 1}$ is selected from a set of unitary vectors in the form of Kronecker-product-based codebook, e.g., $\mathbf{p}_p = \mathbf{p}_{p,1} \otimes \mathbf{p}_{p,2}$ where $\mathbf{p}_{p,1} \in \mathbb{C}^{N_1}$ and $\mathbf{p}_{p,2} \in \mathbb{C}^{N_2}$ are selected from two DFT codebooks of dimensions N_1 and N_2 , respectively [Yang *et al.*, 2010]. The p -th received signal vector can be expressed as

$$\mathbf{y}_p = \mathbf{H}\mathbf{p}_p s_p + \mathbf{w}_p, \quad (5.7)$$

where $\mathbf{w}_p \sim \mathcal{CN}(\mathbf{0}, \sigma_w^2 \mathbf{I}_M)$ is the additive white Gaussian noise (AWGN) with \mathbf{I}_M denoting the $M \times M$ identity matrix, and s_p denotes the pilot symbol in the p -th time slot. The receiver collects $\mathbf{y}_p \in \mathbb{C}^{M \times 1}$ for $p = 1, \dots, P$ and concatenates them to obtain the signal matrix

$$\mathbf{Y} = [\mathbf{y}_1 \ \mathbf{y}_2 \ \dots \ \mathbf{y}_P] = \mathbf{H}\mathbf{P}\mathbf{S} + \mathbf{W} = \mathbf{B}\Sigma\mathbf{A}^H\mathbf{P}\mathbf{S} + \mathbf{W}, \quad (5.8)$$

where $\mathbf{P} = [\mathbf{p}_1 \ \mathbf{p}_2 \ \dots \ \mathbf{p}_P] \in \mathbb{C}^{N \times P}$, $\mathbf{W} = [\mathbf{w}_1 \ \mathbf{w}_2 \ \dots \ \mathbf{w}_P] \in \mathbb{C}^{M \times P}$ and

$$\mathbf{S} = \text{diag}([s_1 \ s_2 \ \dots \ s_P]) \in \mathbb{C}^{P \times P}.$$

For simplicity, we assume that $\mathbf{S} = \sqrt{P_t}\mathbf{I}_P$, where P_t is the power of the pilot symbol. Then we have

$$\mathbf{Y} = \sqrt{P_t}\mathbf{H}\mathbf{P} + \mathbf{W} = \sqrt{P_t}\mathbf{B}\Sigma\mathbf{A}^H\mathbf{P} + \mathbf{W}. \quad (5.9)$$

Our goal is to estimate the channel matrix $\mathbf{H} \in \mathbb{C}^{M \times N}$ from the measurements $\mathbf{Y} \in \mathbb{C}^{M \times P}$. Note that the number of pilots is usually smaller than the number of transmit antennas, i.e., $P < N$. Hence, we need to exploit the sparsity of \mathbf{H} for its estimation, which will be discussed in the next section.

5.2.2 Existing mmWave Channel Estimation Methods

Before describing our proposed mmWave channel estimator, we briefly discuss some existing mmWave channel estimation methods [Alkhateeb *et al.*, 2014; Lee *et al.*, 2014; Sun and Rappaport, 2017; Guo *et al.*, 2017] which can be divided into two categories.

5.2.2.1 CS-based mmWave channel estimators

The mmWave channel is usually composed of small number of propagation paths and CS-based algorithms have been developed [Alkhateeb *et al.*, 2014; Lee *et al.*, 2014; Sun and Rappaport, 2017] for channel estimation. First the dictionary matrices $\mathbf{A}_D \in \mathbb{C}^{N \times N_G}$ and $\mathbf{B}_D \in \mathbb{C}^{M \times N_G}$ are constructed based on quantized AoD angle of the transmitter and AoA angle of the receiver. The AoDs and AoAs are assumed to be taken from a uniform grid of N_G points with $N_G \gg L$. The resulting dictionary matrix is expressed (take the transmitter \mathbf{A}_D for example, the receiver dictionary matrix \mathbf{B}_D is similar.)

$$\mathbf{A}_D = [\mathbf{a}(\bar{\mathbf{g}}_1) \mathbf{a}(\bar{\mathbf{g}}_2) \dots \mathbf{a}(\bar{\mathbf{g}}_{N_G})], \quad (5.10)$$

where $\bar{\mathbf{g}}_i = \{\bar{g}_{i,1}, \bar{g}_{i,2}\} = \{\frac{1}{2} \sin(\bar{\vartheta}_i) \cos(\bar{\varphi}_i), \frac{1}{2} \cos(\bar{\vartheta}_i)\}$ with $\bar{\vartheta}_i = \frac{(i-1)2\pi}{N_G} - \pi$, $\bar{\varphi}_i = \frac{(i-1)2\pi}{N_G} - \pi$ denotes the transmit array response vector for the grid point $\bar{\vartheta}_i$ and $\bar{\varphi}_i$ for $i = 1, 2, \dots, N_G$. The size N_G of the angle grids can be set according to the desired angular resolution. On this basis, the received signal \mathbf{Y} in (5.9) can be vectorized as [Alkhateeb *et al.*, 2014]

$$\mathbf{y} = \text{vec}(\mathbf{Y}) = \sqrt{P_t} (\mathbf{P}^T \otimes \mathbf{I}_M) \text{vec}(\mathbf{H}) + \mathbf{w} \quad (5.11)$$

$$= \sqrt{P_t} (\mathbf{P}^T \otimes \mathbf{I}_M) (\mathbf{A}_D^* \odot \mathbf{B}_D) \mathbf{x} + \mathbf{w} = \sqrt{P_t} \mathbf{G} \mathbf{x} + \mathbf{w}, \quad (5.12)$$

where \odot denotes the matrix Khatri-Rao products, $(\cdot)^T$ denotes the transpose operation, $(\cdot)^*$ denotes the complex conjugate, $\mathbf{x} \in \mathbb{C}^{N_G^4}$ is a sparse vector that has non-zero elements in the locations associated with the dominant paths. Note that the angle spaces of interest are discretized into a large number of grids, and the actual AoA and AoD angles may not exactly reside on the predefined grids. Those off-grid angles can lead to mismatches in the channel model and degrade the estimation performance.

5.2.2.2 Subspace-based mmWave channel estimators

Another existing approach to mmWave channel estimation is based on the subspace methods such as the MUSIC algorithm [Guo *et al.*, 2017]. The MUSIC algorithm

firstly calculates the covariance matrix of the received signal \mathbf{Y} and then finds the signal and noise subspaces via eigendecomposition. It then estimates each channel path's array response, i.e., $\hat{\mathbf{g}}_l$ and $\hat{\mathbf{f}}_l$ for $l = 1, 2, \dots, \hat{L}$, where \hat{L} is the estimated number of paths, by exploiting the orthogonality between the signal and noise subspaces. Finally, each channel path's coefficient, i.e., $\hat{\sigma}_l$ can be estimated via the least-squares (LS) method. The MUSIC algorithm has been popular for its good resolution and accuracy in AoD/AoA estimation [Gupta and Kar, 2015], [Zhang *et al.*, 2014]. However, it is also reported that the off-grid CS method [Tang *et al.*, 2013] can outperform the MUSIC algorithm in terms of estimation accuracy in noisy environments [Bhaskar *et al.*, 2013a; Yang and Xie, 2016].

5.3 Channel Estimation via Atomic Norm Minimization

As explained in the previous section, the performance of the mmWave channel estimators based on on-grid methods such as CS can be degraded due to grid mismatch. In this section, we propose a new mmWave channel estimator based on an off-grid CS method, i.e., the atomic norm minimization method.

5.3.1 Background on Multi-dimensional Atomic Norm

First we briefly introduce the concept of multi-dimensional atomic norm [Yang *et al.*, 2016]. A d -dimensional (d -dim) atom is defined as

$$\mathbf{q}_d(x_1, \dots, x_d) = \mathbf{c}_{n_1}(x_1) \otimes \dots \otimes \mathbf{c}_{n_d}(x_d), \quad (5.13)$$

where n_i is the length of the normalized vector $\mathbf{c}_{n_i}(x_i)$ defined in (5.2) and $x_i \in [-\frac{1}{2}, \frac{1}{2})$ for $i = 1, 2, \dots, d$. The d -dim atomic set is then given by

$$\mathcal{A} = \left\{ \mathbf{q}_d(x_1, \dots, x_d) : x_i \in \left[-\frac{1}{2}, \frac{1}{2}\right), i = 1, \dots, d \right\}. \quad (5.14)$$

CHAPTER 5. BEAMFORMED MILLIMETER-WAVE FULL-DIMENSIONAL MIMO CHANNEL ESTIMATION BASED ON ATOMIC NORM MINIMIZATION

For any vector \mathbf{t}_d of the form $\mathbf{t}_d = \sum_l \alpha_l \mathbf{q}_d(x_{l,1}, x_{l,2}, \dots, x_{l,d})$, its d -dim atomic norm with respect to \mathcal{A} is defined as

$$\begin{aligned} \|\mathbf{t}_d\|_{\mathcal{A}} &= \inf \{t : \mathbf{t}_d \in t \text{conv}(\mathcal{A})\}, \\ &= \inf_{\substack{x_{l,1}, x_{l,2}, \dots, x_{l,d} \in [-\frac{1}{2}, \frac{1}{2}) \\ \alpha_l \in \mathbb{C}}} \left\{ \sum_l |\alpha_l| \left| \mathbf{t}_d = \sum_l \alpha_l \mathbf{q}_d(x_{l,1}, x_{l,2}, \dots, x_{l,d}) \right. \right\}, \end{aligned} \quad (5.15)$$

where $\text{conv}(\mathcal{A})$ is the convex hull of \mathcal{A} . The d -dim atomic norm of \mathbf{t}_d has following equivalent form [Yang *et al.*, 2016]:

$$\|\mathbf{t}_d\|_{\mathcal{A}} = \inf_{\mathcal{U}_d \in \mathbb{C}^{(2n_d-1) \times (2n_{d-1}-1) \times \dots \times (2n_1-1)}, t \in \mathbb{R}} \left\{ \begin{aligned} &\frac{1}{2n_1 n_2 \dots n_d} \text{Tr}(\mathbb{T}_d(\mathcal{U}_d)) + \frac{1}{2}t \\ &\text{s.t.} \begin{bmatrix} \mathbb{T}_d(\mathcal{U}_d) & \mathbf{t}_d \\ \mathbf{t}_d^H & t \end{bmatrix} \succeq 0 \end{aligned} \right\}, \quad (5.16)$$

where $\text{Tr}(\cdot)$ is the trace of the input matrix, $\mathcal{U}_d \in \mathbb{C}^{(2n_d-1) \times (2n_{d-1}-1) \times \dots \times (2n_1-1)}$ is a d -way tensor and $\mathbb{T}_d(\mathcal{U}_d)$ is a d -level block Toeplitz, which is defined recursively as follows. Denote $\mathbf{n}_d = (n_d, n_{d-1}, \dots, n_1)$ and $\mathcal{U}_{d-1}(i) = \mathcal{U}_d(i, :, :, \dots, :)$ for $i = -n_d + 1, -n_d + 2, \dots, n_d - 1$. For $d = 1$, $\mathbf{n}_1 = (n_1)$ and $\mathbb{T}_1(\mathbf{u}_1) = \text{Toep}(\mathbf{u}_1)$ with $\mathbf{u}_1 \in \mathbb{C}^{(2n_1-1) \times 1}$, i.e.,

$$\mathbb{T}_1(\mathbf{u}_1) = \text{Toep}(\mathbf{u}_1) = \begin{bmatrix} u_1(0) & u_1(1) & \cdots & u_1(n_1 - 1) \\ u_1(-1) & u_1(0) & \cdots & u_1(n_1 - 2) \\ \vdots & \vdots & \ddots & \vdots \\ u_1(1 - n_1) & u_1(2 - n_1) & \cdots & u_1(0) \end{bmatrix}. \quad (5.17)$$

For $d \geq 2$, we have

$$\mathbb{T}_d(\mathcal{U}_d) = \begin{bmatrix} \mathbb{T}_{d-1}(\mathcal{U}_{d-1}(0)) & \mathbb{T}_{d-1}(\mathcal{U}_{d-1}(1)) & \cdots & \mathbb{T}_{d-1}(\mathcal{U}_{d-1}(n_d - 1)) \\ \mathbb{T}_{d-1}(\mathcal{U}_{d-1}(-1)) & \mathbb{T}_{d-1}(\mathcal{U}_{d-1}(0)) & \cdots & \mathbb{T}_{d-1}(\mathcal{U}_{d-1}(n_d - 2)) \\ \vdots & \vdots & \ddots & \vdots \\ \mathbb{T}_{d-1}(\mathcal{U}_{d-1}(1 - n_d)) & \mathbb{T}_{d-1}(\mathcal{U}_{d-1}(2 - n_d)) & \cdots & \mathbb{T}_{d-1}(\mathcal{U}_{d-1}(0)) \end{bmatrix} \quad (5.18)$$

5.3.2 Atomic Norm Minimization Formulation

In this subsection, we formulate the atomic norm minimization problem for channel estimation. First, we vectorize the mmWave FD-MIMO channel matrix \mathbf{H} in (5.1) as

$$\begin{aligned} \mathbf{h} &= \text{vec}(\mathbf{H}) = \sum_{l=1}^L \sigma_l \mathbf{a}(\mathbf{g}_l)^* \otimes \mathbf{b}(\mathbf{f}_l) \\ &= \sum_{l=1}^L \sigma_l \left(\mathbf{c}_{N_1}(g_{l,1}) \otimes \mathbf{c}_{N_2}(g_{l,2}) \right)^* \otimes \left(\mathbf{c}_{M_1}(f_{l,1}) \otimes \mathbf{c}_{M_2}(f_{l,2}) \right) \\ &= \sum_{l=1}^L \sigma_l \mathbf{c}_{N_1}^*(g_{l,1}) \otimes \mathbf{c}_{N_2}^*(g_{l,2}) \otimes \mathbf{c}_{M_1}(f_{l,1}) \otimes \mathbf{c}_{M_2}(f_{l,2}). \end{aligned} \quad (5.19)$$

Comparing (5.15) and (5.19), for the mmWave FD-MIMO channel with UPA configuration, the atom has the form of

$$\mathbf{q}_4(\mathbf{g}, \mathbf{f}) = \mathbf{c}_{N_1}^*(g_1) \otimes \mathbf{c}_{N_2}^*(g_2) \otimes \mathbf{c}_{M_1}(f_1) \otimes \mathbf{c}_{M_2}(f_2), \quad (5.20)$$

and the set of atoms is defined as the collection of all normalized 4D complex sinusoids: $\mathcal{A} = \{\mathbf{q}_4(\mathbf{g}, \mathbf{f}) : \mathbf{f} \in [-\frac{1}{2}, \frac{1}{2}) \times [-\frac{1}{2}, \frac{1}{2}), \mathbf{g} \in [-\frac{1}{2}, \frac{1}{2}) \times [-\frac{1}{2}, \frac{1}{2})\}$ [Chi and Chen, 2013; 2015]. The 4D atomic norm for any \mathbf{h} defined in (5.19) can be written as [Chi and Chen, 2013]:

$$\|\mathbf{h}\|_{\mathcal{A}} = \inf_{\substack{\mathbf{f}_l \in [-\frac{1}{2}, \frac{1}{2}) \times [-\frac{1}{2}, \frac{1}{2}), \\ \mathbf{g}_l \in [-\frac{1}{2}, \frac{1}{2}) \times [-\frac{1}{2}, \frac{1}{2}), \\ \sigma_l \in \mathbb{C}}} \left\{ \sum_l |\sigma_l| \mid \mathbf{h} = \sum_l \sigma_l \mathbf{q}_4(\mathbf{g}_l, \mathbf{f}_l) \right\}. \quad (5.21)$$

The atomic norm can enforce sparsity in the atom set \mathcal{A} . On this basis, an optimization problem will be formulated for the estimation of the path frequencies $\{\mathbf{f}_l, \mathbf{g}_l\}$. For the convenience of calculation, we will use the equivalent form of the atomic norm given by (5.16), i.e.,

$$\|\mathbf{h}\|_{\mathcal{A}} = \inf_{\substack{\mathcal{U}_4 \in \mathbb{C}^{(2N_1-1) \times (2N_2-1) \times (2M_1-1) \times (2M_2-1)}, \\ t \in \mathbb{R}}} \left\{ \begin{aligned} &\frac{1}{2MN} \text{Tr}(\mathbb{T}_4(\mathcal{U}_4)) + \frac{1}{2}t \\ &\text{s.t.} \begin{bmatrix} \mathbb{T}_4(\mathcal{U}_4) & \mathbf{h} \\ \mathbf{h}^H & t \end{bmatrix} \succeq 0 \end{aligned} \right\}, \quad (5.22)$$

CHAPTER 5. BEAMFORMED MILLIMETER-WAVE FULL-DIMENSIONAL MIMO CHANNEL ESTIMATION BASED ON ATOMIC NORM MINIMIZATION

where $\mathbb{T}_4(\mathcal{U}_4)$ is a 4-level Toeplitz matrix defined in (5.18). Define the minimum frequency separations as

$$\Delta_{\min, f_i} = \min_{l \neq l'} \min\{|f_{l,i} - f_{l',i}|, 1 - |f_{l,i} - f_{l',i}|\}, \quad (5.23)$$

$$\Delta_{\min, g_i} = \min_{l \neq l'} \min\{|g_{l,i} - g_{l',i}|, 1 - |g_{l,i} - g_{l',i}|\}, \quad (5.24)$$

for $i = 1, 2$. To show the connection between the atomic norm and the channel matrix, we obtain the following theorem via extending Theorem 1.2 in [Candès and Fernandez-Granda, 2014] for 1D atomic norm to 4D atomic norm.

Theorem 1. *If the path component frequencies are sufficiently separated, i.e.,*

$$\Delta_{\min, f_i} \geq \frac{1}{\lfloor (M_i - 1)/4 \rfloor}, \quad (5.25)$$

$$\Delta_{\min, g_i} \geq \frac{1}{\lfloor (N_i - 1)/4 \rfloor}, \quad (5.26)$$

for $i = 1, 2$, then we have $\|\mathbf{h}\|_{\mathcal{A}} = \sum_l |\sigma_l|$, so the component atoms of \mathbf{h} can be uniquely located via computing its atomic norm.

The proof follows the same line as that in Theorem 1.2 [Candès and Fernandez-Granda, 2014], with the dual polynomial constructed by interpolation with a 4D kernel. The theorem holds because all bounds in the proof of [Theorem 1.2, 34] hold by leveraging the 1D results.

To estimate the mmWave FD-MIMO channel \mathbf{H} in (5.1) based on the signal \mathbf{Y} in (5.9), we then formulate the following optimization problem:

$$\hat{\mathbf{h}} = \min_{\mathbf{h} \in \mathbb{C}^{MN}} \mu \|\mathbf{h}\|_{\mathcal{A}} + \frac{1}{2} \left\| \mathbf{y} - \sqrt{P_t} (\mathbf{P}^T \otimes \mathbf{I}_M) \mathbf{h} \right\|_2^2, \quad (5.27)$$

where $\mathbf{y} = \text{vec}(\mathbf{Y})$ is given by (5.11) and $\mu \propto \sigma_w \sqrt{MN \log(MN)}$ is a weight factor [Zheng and Wang, 2017]. Using (5.22), (5.27) can be equivalently formulated as a semi-definite program (SDP):

$$\begin{aligned} \min_{\substack{\mathcal{U}_4 \in \mathbb{C}^{(2N_1-1) \times (2N_2-1) \times (2M_1-1) \times (2M_2-1)}, \\ \mathbf{h} \in \mathbb{C}^{MN}, t \in \mathbb{R}}} \quad & \frac{\mu}{2MN} \text{Tr}(\mathbb{T}_4(\mathcal{U}_4)) + \frac{\mu}{2} t + \frac{1}{2} \left\| \mathbf{y} - \sqrt{P_t} (\mathbf{P}^T \otimes \mathbf{I}_M) \mathbf{h} \right\|_2^2 \\ \text{s.t.} \quad & \begin{bmatrix} \mathbb{T}_4(\mathcal{U}_4) & \mathbf{h} \\ \mathbf{h}^H & t \end{bmatrix} \succeq 0. \end{aligned} \quad (5.28)$$

The above problem is convex, and can be solved by using a standard convex solver. Suppose the solution to (5.28) is $\hat{\mathbf{h}}$. Then the estimated channel matrix is given by $\hat{\mathbf{H}} = \text{vec}^{-1}(\hat{\mathbf{h}})$ where $\text{vec}^{-1}(\cdot)$ is the inverse operation of $\text{vec}(\cdot)$.

5.4 Efficient Algorithm for Channel Estimation under UPA

5.4.1 A Formulation Based on 2D MMV Atomic Norm

Note that the dimension of the positive semidefinite matrix in (5.28) is $(MN + 1) \times (MN + 1)$, and the 4D atomic norm minimization formulation is of high computational complexity and has large memory requirements. To reduce the complexity, we can treat \mathbf{Y} as 2D multiple measurement vectors (MMV) [Yang and Xie, 2016] in transmit and receive dimensions.

Unlike the 4D atomic norm that is calculated with input vector \mathbf{h} , the MMV atomic norm is calculated with the matrix input \mathbf{H} . Specifically, we define the atom $\bar{\mathbf{Q}}(\mathbf{f}, \bar{\mathbf{a}}) = \mathbf{b}(\mathbf{f}) \bar{\mathbf{a}}^H$ with $\mathbf{f} \in [-\frac{1}{2}, \frac{1}{2}) \times [-\frac{1}{2}, \frac{1}{2})$, and $\bar{\mathbf{a}} \in \mathbb{C}^{N \times 1}$ with $\|\bar{\mathbf{a}}\|_2 = 1$. Correspondingly, the atom set is defined as

$$\mathcal{A}_{\text{MMV}} = \left\{ \bar{\mathbf{Q}}(\mathbf{f}, \bar{\mathbf{a}}) : \mathbf{f} \in [-\frac{1}{2}, \frac{1}{2}) \times [-\frac{1}{2}, \frac{1}{2}), \|\bar{\mathbf{a}}\|_2 = 1 \right\}. \quad (5.29)$$

It is worth noting that $\bar{\mathbf{a}}$ is not restricted by the structural constraint in (5.3). With (5.29), we extend the 1D MMV atomic norm [Yang and Xie, 2016] to the 2D MMV atomic norm of \mathbf{H} defined by

$$\|\mathbf{H}\|_{\mathcal{A}_{\text{MMV}}} = \inf_{\substack{\mathbf{f}_l \in [-\frac{1}{2}, \frac{1}{2}) \times [-\frac{1}{2}, \frac{1}{2}), \\ \bar{\mathbf{a}}_l \in \mathbb{C}^{N \times 1}, \sigma_l \in \mathbb{C}}} \left\{ \sum_l |\sigma_l| \left| \mathbf{H} = \sum_l \sigma_l \bar{\mathbf{Q}}(\mathbf{f}_l, \bar{\mathbf{a}}_l), \|\bar{\mathbf{a}}_l\|_2 = 1 \right. \right\}. \quad (5.30)$$

This atomic norm is equivalent to the solution of the following SDP [Yang and Xie,

2016]:

$$\|\mathbf{H}\|_{\mathcal{A}_{\text{MMV}}} = \inf_{\mathbf{U}_2 \in \mathbb{C}^{(2M_2-1) \times (2M_1-1)}, \mathbf{X} \in \mathbb{C}^{N \times N}} \left\{ \begin{array}{l} \frac{1}{2M} \text{Tr}(\mathbb{T}_2(\mathbf{U}_2)) + \frac{1}{2N} \text{Tr}(\mathbf{X}) \\ \text{s.t.} \begin{bmatrix} \mathbb{T}_2(\mathbf{U}_2) & \mathbf{H} \\ \mathbf{H}^H & \mathbf{X} \end{bmatrix} \succeq 0 \end{array} \right\}, \quad (5.31)$$

where \mathbf{X} is constrained to be a Hermitian matrix. Then using (5.9), we can formulate the following optimization problem for channel estimation:

$$\hat{\mathbf{H}} = \min_{\mathbf{H} \in \mathbb{C}^{M \times N}} \mu \|\mathbf{H}\|_{\mathcal{A}_{\text{MMV}}} + \frac{1}{2} \left\| \sqrt{P_t} \mathbf{H} \mathbf{P} - \mathbf{Y} \right\|_F^2, \quad (5.32)$$

where $\|\cdot\|_F$ denotes matrix Frobenius norm. Plugging (5.31) into (5.32), the size of the positive semidefinite matrix in the constraint is $(M+N) \times (M+N)$, resulting in considerably lower computational complexity and memory requirement than (5.28).

5.4.2 An Approximation to 4D Atomic Norm Minimization

Next we propose an approximation to the 4D atomic norm to reduce the computational complexity. Similar to the 2D MMV atomic norm, the proposed approximation is calculated with input \mathbf{H} . From (5.1), \mathbf{H} is the sum of $\sigma_l \mathbf{b}(\mathbf{f}_l) \mathbf{a}(\mathbf{g}_l)^H$, in which both $\mathbf{a}(\mathbf{g}_l)$ and $\mathbf{b}(\mathbf{f}_l)$ are Fourier bases. Different from the vectorized atomic norm, we introduce the matrix atom $\mathbf{Q}(\mathbf{f}, \mathbf{g}) = \mathbf{b}(\mathbf{f}) \mathbf{a}(\mathbf{g})^H$ and the matrix atom set

$$\mathcal{A}_M = \left\{ \mathbf{Q}(\mathbf{f}, \mathbf{g}) = \mathbf{b}(\mathbf{f}) \mathbf{a}(\mathbf{g})^H : \mathbf{f} \in [-\frac{1}{2}, \frac{1}{2}) \times [-\frac{1}{2}, \frac{1}{2}), \mathbf{g} \in [-\frac{1}{2}, \frac{1}{2}) \times [-\frac{1}{2}, \frac{1}{2}) \right\} \quad (5.33)$$

The matrix atomic norm is then given by

$$\|\mathbf{H}\|_{\mathcal{A}_M} = \inf_{\substack{\mathbf{f}_l \in [-\frac{1}{2}, \frac{1}{2}) \times [-\frac{1}{2}, \frac{1}{2}), \\ \mathbf{g}_l \in [-\frac{1}{2}, \frac{1}{2}) \times [-\frac{1}{2}, \frac{1}{2}), \\ \sigma_l \in \mathbb{C}}} \left\{ \sum_l |\sigma_l| \left| \mathbf{H} = \sum_l \sigma_l \mathbf{Q}(\mathbf{f}_l, \mathbf{g}_l) \right| \right\}. \quad (5.34)$$

The matrix atom set is composed of rank-one matrices, and hence it amounts to atomic norm of low rank matrices. Since the operator $\text{vec}(\cdot)$ is a one-to-one mapping

CHAPTER 5. BEAMFORMED MILLIMETER-WAVE FULL-DIMENSIONAL MIMO CHANNEL ESTIMATION BASED ON ATOMIC NORM MINIMIZATION

and the mapping $\mathcal{A}_M \rightarrow \mathcal{A}$ is also one-to-one, it is straightforward to conclude that $\|\mathbf{H}\|_{\mathcal{A}_M} = \|\mathbf{h}\|_{\mathcal{A}}$. Hence, if the component frequencies satisfy the sufficient separation condition given by (5.25) and (5.26), we have $\|\mathbf{H}\|_{\mathcal{A}_M} = \sum_l |\sigma_l|$ by Theorem 1.

Finding the harmonic components via atomic norm is an infinite programming problem over all feasible \mathbf{f} and \mathbf{g} , which is difficult. For better efficiency, we use $\text{SDP}(\mathbf{H})$ in the following Lemma to approximate $\|\mathbf{H}\|_{\mathcal{A}_M}$.

Lemma 1. For \mathbf{H} given by (5.1), we have $\|\mathbf{H}\|_{\mathcal{A}_M} \geq \text{SDP}(\mathbf{H}) \geq \|\mathbf{H}\|_{\mathcal{A}_{\text{MMV}}}$, where

$$\text{SDP}(\mathbf{H}) \triangleq \inf_{\mathbf{U}_2 \in \mathbb{C}^{(2M_2-1) \times (2M_1-1)}, \mathbf{V}_2 \in \mathbb{C}^{(2N_2-1) \times (2N_1-1)}} \left\{ \begin{array}{l} \frac{1}{2M} \text{Tr}(\mathbb{T}_2(\mathbf{U}_2)) + \frac{1}{2N} \text{Tr}(\mathbb{T}_2(\mathbf{V}_2)) \\ \text{s.t. } \begin{bmatrix} \mathbb{T}_2(\mathbf{U}_2) & \mathbf{H} \\ \mathbf{H}^H & \mathbb{T}_2(\mathbf{V}_2) \end{bmatrix} \succeq 0 \end{array} \right\}, \quad (5.35)$$

with $\mathbb{T}_2(\mathbf{U}_2)$ and $\mathbb{T}_2(\mathbf{V}_2)$ being 2-level Toeplitz matrices defined in (5.18).

Proof. The relation $\text{SDP}(\mathbf{H}) \geq \|\mathbf{H}\|_{\mathcal{A}_{\text{MMV}}}$ can be directly obtained from the definitions in (5.31) and (5.35). It remains to show $\|\mathbf{H}\|_{\mathcal{A}_M} \geq \text{SDP}(\mathbf{H})$. Denote

$$\begin{aligned} \tilde{\mathbf{a}}(\mathbf{g}_l, \omega_l) &= \frac{1}{\sqrt{N}} e^{j2\pi\omega_l} \mathbf{c}_{N_1}^*(g_{l,1}) \otimes \mathbf{c}_{N_2}^*(g_{l,2}), \\ \tilde{\mathbf{b}}(\mathbf{f}_l, \chi_l) &= \frac{1}{\sqrt{M}} e^{j2\pi\chi_l} \mathbf{c}_{M_1}(f_{l,1}) \otimes \mathbf{c}_{M_2}(f_{l,2}), \end{aligned}$$

with $\omega_l \in [0, 2\pi]$ and $\chi_l \in [0, 2\pi]$ such that $\sigma_l = |\sigma_l| e^{j2\pi(\omega_l + \chi_l)}$. For any $\mathbf{H} = \sum_l \sigma_l \mathbf{b}(\mathbf{f}_l) \mathbf{a}(\mathbf{g}_l)^H$, if we set

$$\mathbf{U}_2 = [\mathbf{u}_1(-M_1 + 1), \mathbf{u}_1(-M_1 + 2), \dots, \mathbf{u}_1(M_1 - 1)], \quad (5.36)$$

$$\mathbf{V}_2 = [\mathbf{v}_1(-N_1 + 1), \mathbf{v}_1(-N_1 + 2), \dots, \mathbf{v}_1(N_1 - 1)], \quad (5.37)$$

where

$$\mathbf{u}_1(i) = \frac{1}{\sqrt{M}} \sum_l |\sigma_l| \tilde{\mathbf{c}}_{M_2}(f_{l,2}) e^{j2\pi(i-1)f_{l,1}}, \quad (5.38)$$

$$\mathbf{v}_1(i) = \frac{1}{\sqrt{N}} \sum_l |\sigma_l| \tilde{\mathbf{c}}_{N_2}^*(g_{l,2}) e^{-j2\pi(i-1)g_{l,1}}, \quad (5.39)$$

CHAPTER 5. BEAMFORMED MILLIMETER-WAVE FULL-DIMENSIONAL MIMO CHANNEL ESTIMATION BASED ON ATOMIC NORM MINIMIZATION

with $\tilde{\mathbf{c}}_n(x) = \frac{1}{\sqrt{n}} [e^{j2\pi(1-n)x}, e^{j2\pi(2-n)x}, \dots, e^{j2\pi(n-1)x}]^T \in \mathbb{C}^{2n \times 1}$, then the 2-level Toeplitz matrices $\mathbb{T}_2(\mathbf{U}_2)$ and $\mathbb{T}_2(\mathbf{V}_2)$ satisfy

$$\begin{aligned} \mathbb{T}_2(\mathbf{U}_2) &= \sum_l |\sigma_l| \mathbf{b}(\mathbf{f}_l) \mathbf{b}(\mathbf{f}_l)^H \\ &= \sum_l |\sigma_l| \tilde{\mathbf{b}}(\mathbf{f}_l, \chi_l) \tilde{\mathbf{b}}(\mathbf{f}_l, \chi_l)^H, \end{aligned} \quad (5.40)$$

$$\begin{aligned} \mathbb{T}_2(\mathbf{V}_2) &= \sum_l |\sigma_l| \mathbf{a}(\mathbf{g}_l) \mathbf{a}(\mathbf{g}_l)^H \\ &= \sum_l |\sigma_l| \tilde{\mathbf{a}}(\mathbf{g}_l, \omega_l) \tilde{\mathbf{a}}(\mathbf{g}_l, \omega_l)^H. \end{aligned} \quad (5.41)$$

Moreover, the matrix

$$\mathbf{M} = \begin{bmatrix} \mathbb{T}_2(\mathbf{U}_2) & \mathbf{H} \\ \mathbf{H}^H & \mathbb{T}_2(\mathbf{V}_2) \end{bmatrix} = \sum_l |\sigma_l| \begin{bmatrix} \tilde{\mathbf{b}}(\mathbf{f}_l, \chi_l) \\ \tilde{\mathbf{a}}(\mathbf{g}_l, \omega_l) \end{bmatrix} \begin{bmatrix} \tilde{\mathbf{b}}(\mathbf{f}_l, \chi_l) \\ \tilde{\mathbf{a}}(\mathbf{g}_l, \omega_l) \end{bmatrix}^H \quad (5.42)$$

is positive semidefinite, indicating that the constraints in (5.35) are satisfied. Note that $\text{SDP}(\mathbf{H}) \leq \frac{1}{2M} \text{Tr}(\mathbb{T}_2(\mathbf{U}_2)) + \frac{1}{2N} \text{Tr}(\mathbb{T}_2(\mathbf{V}_2)) = \sum_l |\sigma_l|$ according to the definition in (5.35). Since this holds for any decomposition of \mathbf{H} , we obtain $\text{SDP}(\mathbf{H}) \leq \|\mathbf{H}\|_{\mathcal{A}_M}$. \square

The above lemma shows that $\text{SDP}(\mathbf{H})$ is a lower bound of the matrix atomic norm. Moreover, the following lemma states that if the component frequencies are sufficiently separated, then $\text{SDP}(\mathbf{H})$ is equivalent to $\|\mathbf{H}\|_{\mathcal{A}_M}$.

Lemma 2. *If (5.25)-(5.26) hold, then $\|\mathbf{H}\|_{\mathcal{A}_M} = \text{SDP}(\mathbf{H})$.*

Proof. First it follows from Theorem 4 in [Yang and Xie, 2016] that if (5.25)-(5.26) hold, then we have $\|\mathbf{H}\|_{\mathcal{A}_{\text{MMV}}} = \sum_l |\sigma_l|$. Using Theorem 1 and the fact that $\|\mathbf{h}\|_{\mathcal{A}} = \|\mathbf{H}\|_{\mathcal{A}_M}$, we have $\|\mathbf{H}\|_{\mathcal{A}_M} = \|\mathbf{H}\|_{\mathcal{A}_{\text{MMV}}}$. Finally by Lemma 1 we have $\|\mathbf{H}\|_{\mathcal{A}_M} = \|\mathbf{H}\|_{\mathcal{A}_{\text{MMV}}} = \text{SDP}(\mathbf{H})$. \square

When the sufficient separation condition given by (5.25) and (5.26) is not satisfied, $\text{SDP}(\mathbf{H})$ may not be the same as $\|\mathbf{H}\|_{\mathcal{A}_M}$. However, it is found via simulations

CHAPTER 5. BEAMFORMED MILLIMETER-WAVE FULL-DIMENSIONAL MIMO CHANNEL ESTIMATION BASED ON ATOMIC NORM MINIMIZATION

that $\text{SDP}(\mathbf{H})$ still provides a good approximation to $\|\mathbf{H}\|_{\mathcal{A}_M}$ and usually results in good performance in channel estimation. Moreover, as shown by Lemma 1, $\text{SDP}(\mathbf{H})$ is a lower bound of the atomic norm $\|\mathbf{H}\|_{\mathcal{A}_M}$ (or $\|\mathbf{h}\|_{\mathcal{A}}$ equivalently), i.e., $\|\mathbf{h}\|_{\mathcal{A}} = \|\mathbf{H}\|_{\mathcal{A}_M} \geq \text{SDP}(\mathbf{H})$ in general.

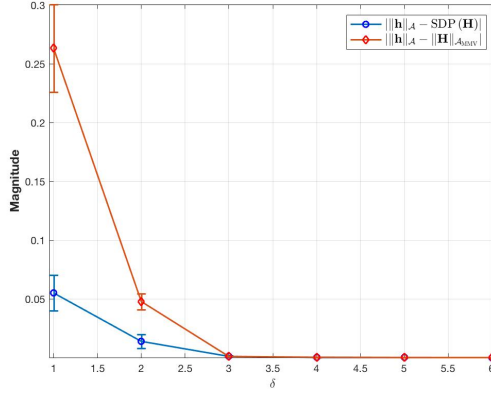


Figure 5.1: The approximation errors $|\|\mathbf{H}\|_{\mathcal{A}_M} - \text{SDP}(\mathbf{H})|$ and $|\|\mathbf{H}\|_{\mathcal{A}_M} - \|\mathbf{H}\|_{\mathcal{A}_{\text{MMV}}}|$ when the separations satisfy $\Delta_{\min, f_i} \geq \delta(M_i - 1)$, $\Delta_{\min, g_i} \geq \delta/(N_i - 1)$, $N_i = M_i = 16$, for $i = 1, 2$. The simulations are run 100 times for each δ .

To show the approximation performances of both $\|\mathbf{H}\|_{\mathcal{A}_{\text{MMV}}}$ and $\text{SDP}(\mathbf{H})$ to $\|\mathbf{h}\|_{\mathcal{A}}$, we perform a series of Monte Carlo trials for parameters $M_1 = M_2 = 16$, $N_1 = N_2 = 16$ with $L = 2$. \mathbf{f}_l and \mathbf{g}_l take random values from $[-\frac{1}{2}, \frac{1}{2}) \times [-\frac{1}{2}, \frac{1}{2})$ such that the separations satisfy $\Delta_{\min, f_i} \geq \delta/\lfloor(N_i - 1)\rfloor$, $\Delta_{\min, g_i} \geq \delta/\lfloor(N_i - 1)\rfloor$ with $1 \leq \delta \leq 6$. In Fig. 5.1, we plot the approximation error against δ and the bars show 95% confidence interval. As δ decreases, both approximation errors become larger. However, $\text{SDP}(\mathbf{H})$ provides a more accurate approximation than $\|\mathbf{H}\|_{\mathcal{A}_{\text{MMV}}}$. When $\delta \geq 4$, both approximation errors become zero.

Therefore, instead of solving the original 4D atomic norm minimization in (5.28),

CHAPTER 5. BEAMFORMED MILLIMETER-WAVE FULL-DIMENSIONAL MIMO CHANNEL ESTIMATION BASED ON ATOMIC NORM MINIMIZATION

we can solve the following SDP

$$\begin{aligned} \hat{\mathbf{H}} = & \min_{\substack{\mathbf{H} \in \mathbb{C}^{M \times N}, \\ \mathbf{U}_2 \in \mathbb{C}^{(2M_2-1) \times (2M_1-1)}, \\ \mathbf{V}_2 \in \mathbb{C}^{(2N_2-1) \times (2N_1-1)}}} \frac{\mu}{2M} \text{Tr}(\mathbb{T}_2(\mathbf{U}_2)) + \frac{\mu}{2N} \text{Tr}(\mathbb{T}_2(\mathbf{V}_2)) + \frac{1}{2} \left\| \sqrt{P_t} \mathbf{H} \mathbf{P} - \mathbf{Y} \right\|_F^2 \\ \text{s.t.} \quad & \mathbf{M} = \begin{bmatrix} \mathbb{T}_2(\mathbf{U}_2) & \mathbf{H} \\ \mathbf{H}^H & \mathbb{T}_2(\mathbf{V}_2) \end{bmatrix} \succeq 0. \end{aligned} \quad (5.43)$$

The size of the positive semidefinite matrix in the constraint is $(M + N) \times (M + N)$, resulting in considerably lower computational complexity and memory requirement than (5.28).

5.4.3 ADMM for Approximate 4D Atomic Norm Minimization

To meet the requirement of real-time signal processing, we next derive an iterative algorithm for solving the SDP in (5.43), based on the alternating direction method of multipliers (ADMM) [Boyd *et al.*, 2011]. To put our problem in an appropriate form for ADMM, rewrite (5.43) as

$$\begin{aligned} \arg \min_{\substack{\mathbf{H} \in \mathbb{C}^{M \times N}, \\ \mathbf{U}_2 \in \mathbb{C}^{(2M_2-1) \times (2M_1-1)}, \\ \mathbf{V}_2 \in \mathbb{C}^{(2N_2-1) \times (2N_1-1)}}} \frac{1}{2} \left\| \mathbf{H} \mathbf{P} - \mathbf{Y} \right\|_F^2 + \frac{\gamma}{2M} \text{Tr}(\mathbb{T}_2(\mathbf{U}_2)) + \frac{\gamma}{2N} \text{Tr}(\mathbb{T}_2(\mathbf{V}_2)) + \mathbb{I}_\infty(\mathbf{M} \succeq \mathbf{0}) \end{aligned} \quad (5.44)$$

where $\mathbb{I}_\infty(z)$ is an indicator function that is 0 if z is true, and infinity otherwise. Dualize the equality constraint via an augmented Lagrangian, we have

$$\begin{aligned} \mathcal{L}_\rho(\mathbf{U}_2, \mathbf{V}_2, \mathbf{H}, \mathbf{Y}, \mathbf{M}) = & \frac{\gamma}{2M} \text{Tr}(\mathbb{T}_2(\mathbf{U}_2)) + \frac{\gamma}{2N} \text{Tr}(\mathbb{T}_2(\mathbf{V}_2)) + \frac{1}{2} \left\| \mathbf{H} \mathbf{P} - \mathbf{Y} \right\|_F^2 + \mathbb{I}_\infty(\mathbf{M} \succeq \mathbf{0}) \\ & + \left\langle \mathbf{Y}, \mathbf{M} - \begin{bmatrix} \mathbb{T}_2(\mathbf{U}_2) & \mathbf{H} \\ \mathbf{H}^H & \mathbb{T}_2(\mathbf{V}_2) \end{bmatrix} \right\rangle \\ & + \frac{\rho}{2} \left\| \mathbf{M} - \begin{bmatrix} \mathbb{T}_2(\mathbf{U}_2) & \mathbf{H} \\ \mathbf{H}^H & \mathbb{T}_2(\mathbf{V}_2) \end{bmatrix} \right\|_F^2, \end{aligned} \quad (5.45)$$

CHAPTER 5. BEAMFORMED MILLIMETER-WAVE FULL-DIMENSIONAL MIMO CHANNEL ESTIMATION BASED ON ATOMIC NORM MINIMIZATION

where $\mathbf{\Upsilon}$ is the dual variable, $\langle \mathbf{\Upsilon}, \mathbf{M} \rangle \triangleq \text{Re}(\text{Tr}(\mathbf{M}^H \mathbf{\Upsilon}))$, $\rho > 0$ is the penalty parameter. The ADMM consists of the following update steps:

$$(\mathbf{U}_2^{l+1}, \mathbf{V}_2^{l+1}, \mathbf{H}^{l+1}) = \arg \min_{\substack{\mathbf{H} \in \mathbb{C}^{M \times N}, \\ \mathbf{U}_2 \in \mathbb{C}^{(2M_2-1) \times (2M_1-1)}, \\ \mathbf{V}_2 \in \mathbb{C}^{(2N_2-1) \times (2N_1-1)}}} \mathcal{L}_\rho(\mathbf{U}_2, \mathbf{V}_2, \mathbf{H}, \mathbf{\Upsilon}^l, \mathbf{M}^l), \quad (5.46)$$

$$\mathbf{M}^{l+1} = \arg \min_{\mathbf{M} \in \mathbb{C}^{(M+N) \times (M+N)}_{\succeq 0}} \mathcal{L}_\rho(\mathbf{U}_2^{l+1}, \mathbf{V}_2^{l+1}, \mathbf{H}^{l+1}, \mathbf{\Upsilon}^l, \mathbf{M}), \quad (5.47)$$

$$\mathbf{\Upsilon}^{l+1} = \mathbf{\Upsilon}^l + \rho \left(\mathbf{M}^{l+1} - \begin{bmatrix} \mathbb{T}_2(\mathbf{U}_2^{l+1}) & \mathbf{H}^{l+1} \\ (\mathbf{H}^{l+1})^H & \mathbb{T}_2(\mathbf{V}_2^{l+1}) \end{bmatrix} \right). \quad (5.48)$$

Now we derive the updates of (5.46) and (5.47) in detail. For convenience, the following partitions are introduced:

$$\mathbf{M}^l = \begin{bmatrix} \mathbf{M}_0^l & \mathbf{M}_2^l \\ (\mathbf{M}_2^l)^H & \mathbf{M}_1^l \end{bmatrix}, \quad (5.49)$$

$$\mathbf{\Upsilon}^l = \begin{bmatrix} \mathbf{\Upsilon}_0^l & \mathbf{\Upsilon}_2^l \\ (\mathbf{\Upsilon}_2^l)^H & \mathbf{\Upsilon}_1^l \end{bmatrix}, \quad (5.50)$$

where \mathbf{M}_0^l and $\mathbf{\Upsilon}_0^l$ are $M \times M$ matrices, \mathbf{M}_2^l and $\mathbf{\Upsilon}_2^l$ are $M \times N$ matrices, \mathbf{M}_1^l and $\mathbf{\Upsilon}_1^l$ are $N \times N$ matrices. Computing the derivative of $\mathcal{L}_\rho(\mathbf{U}_2, \mathbf{V}_2, \mathbf{H}, \mathbf{\Upsilon}, \mathbf{M})$ with respect to \mathbf{H} , \mathbf{U}_2 and \mathbf{V}_2 , we have

$$\nabla_{\mathbf{H}} \mathcal{L}_\rho = (\mathbf{H}\mathbf{P} - \mathbf{Y})\mathbf{P}^H - 2\mathbf{\Upsilon}_2^l + 2\rho(\mathbf{H} - \mathbf{M}_2^l), \quad (5.51)$$

$$\nabla_{U_2(i,k)} \mathcal{L}_\rho = \begin{cases} \frac{\gamma}{2} + M_1 \rho U_2(i, k) - \text{Tr}(\rho \mathbf{M}_0^l + \mathbf{\Upsilon}_0^l), & i = k = 0, \\ (M_1 - i)(M_2 - k) \rho U_2(i, k) - \sum_{m=0}^{M_2-i-1} \text{Tr}_k \left(\mathcal{S}_{i,k}^{(1)}(\rho \mathbf{M}_0^l + \mathbf{\Upsilon}_0^l) \right), & i \neq 0 \text{ or } k \neq 0, \end{cases} \quad (5.52)$$

$$\nabla_{V_2(i,k)} \mathcal{L}_\rho = \begin{cases} \frac{\gamma}{2} + N_1 \rho V_2(i, k) - \text{Tr}(\rho \mathbf{M}_1^l + \mathbf{\Upsilon}_1^l), & i = k = 0, \\ (N_1 - i)(N_2 - k) \rho V_2(i, k) - \sum_{m=0}^{N_2-i-1} \text{Tr}_k \left(\mathcal{S}_{i,k}^{(2)}(\rho \mathbf{M}_1^l + \mathbf{\Upsilon}_1^l) \right), & i \neq 0 \text{ or } k \neq 0, \end{cases} \quad (5.53)$$

where $U_2(i, k)$ and $V_2(i, k)$ are the (i, k) -th elements of \mathbf{U}_2 and \mathbf{V}_2 , respectively. For $\mathbf{X} \in \mathbb{C}^{M \times M}$, $\mathcal{S}_{i,k}^{(1)}(\mathbf{X})$ returns the (i, k) -th $M_1 \times M_1$ submatrix $\mathbf{X}_{i,k}$. For $\mathbf{X} \in \mathbb{C}^{N \times N}$, $\mathcal{S}_{i,k}^{(2)}(\mathbf{X})$ returns the (i, k) -th $N_1 \times N_1$ submatrix $\mathbf{X}_{i,k}$. $\text{Tr}_k(\cdot)$ outputs the trace of the k -th sub-diagonal of the input matrix. $\text{Tr}_0(\cdot)$ outputs the trace of the input matrix.

CHAPTER 5. BEAMFORMED MILLIMETER-WAVE FULL-DIMENSIONAL MIMO CHANNEL ESTIMATION BASED ON ATOMIC NORM MINIMIZATION

By setting the derivatives to 0, \mathbf{H}^{l+1} , \mathbf{U}_2^{l+1} and \mathbf{V}_2^{l+1} can be updated by:

$$\mathbf{H}^{l+1} = (\mathbf{Y}\mathbf{P}^H + 2\rho\mathbf{M}_2^l + 2\mathbf{\Upsilon}_2^l)(\mathbf{P}\mathbf{P}^H + 2\rho\mathbf{I}_N)^{-1}, \quad (5.54)$$

$$\mathbf{U}_2^{l+1} = \mathbb{T}_2^*(\mathbf{M}_0^l + \mathbf{\Upsilon}_0^l/\rho) - \frac{\gamma}{2M\rho}\mathbf{e}_1, \quad (5.55)$$

$$\mathbf{V}_2^{l+1} = \mathbb{T}_2^*(\mathbf{M}_1^l + \mathbf{\Upsilon}_1^l/\rho) - \frac{\gamma}{2N\rho}\mathbf{e}_1, \quad (5.56)$$

where $\mathbf{e}_1 = [1, 0, 0, \dots, 0]^T$, $\mathbb{T}_2^*(\cdot)$ denotes the adjoints of the map $\mathbb{T}_2(\cdot)$. Specifically, suppose $\mathbf{Z} = \mathbb{T}_2^*(\mathbf{X})$ where $\mathbf{Z} = [\mathbf{z}_{-M_2+1}, \mathbf{z}_{-M_2+2}, \dots, \mathbf{z}_{M_2-1}]$ with $\mathbf{z}_i = [z_i(-M_1 + 1), z_i(-M_1 + 2), \dots, z_i(M_1 - 1)]^T$ when $\mathbf{X} \in \mathbb{C}^{M \times M}$. Then we have

$$z_i(k) = \frac{1}{(M_1 - i)(M_2 - k)} \sum_{m=0}^{M_1-i-1} \text{Tr}_k(\mathcal{S}_{i,m}^{(1)}(\mathbf{X})), \quad (5.57)$$

for $i = -M_2 + 1, -M_2 + 2, \dots, M_2 - 1$ and $k = -M_1 + 1, -M_1 + 2, \dots, M_1 - 1$.

The update of \mathbf{M} is given by

$$\mathbf{M}^{l+1} = \arg \min_{\mathbf{M} \in \mathbb{C}^{(M+N) \times (M+N)}_{\succeq 0}} \left\| \mathbf{M} - \tilde{\mathbf{M}}^{l+1} \right\|_F^2, \quad (5.58)$$

where

$$\tilde{\mathbf{M}}^{l+1} = \begin{bmatrix} \mathbb{T}_2(\mathbf{U}_2^{l+1}) & \mathbf{H}^{l+1} \\ (\mathbf{H}^{l+1})^H & \mathbb{T}_2(\mathbf{V}_2^{l+1}) \end{bmatrix} - \mathbf{\Upsilon}^{l+1}/\rho. \quad (5.59)$$

It is equivalent to projecting $\tilde{\mathbf{M}}^{l+1}$ onto the positive semidefinite cone. Specifically, the projection is accomplished by setting all negative eigenvalues of $\tilde{\mathbf{M}}^{l+1}$ to zero. Note that in ADMM the update of variables \mathbf{H} , \mathbf{U}_2 , \mathbf{V}_2 and \mathbf{M} are in closed-form. Compared to the off-the-shelf solvers such as SeDuMi [Sturm, 1999] and SDPT3 [Toh *et al.*, 1999], whose computational complexity is $\mathcal{O}((M+N)^6)$ in each iteration, the complexity of ADMM is $\mathcal{O}((M+N)^3)$ in each iteration, so it runs much faster.

5.5 The General Planar Array Case

So far we have focused on the uniform planar array (UPA). For mmWave beamformed FD-MIMO, because of the larger average inter-antenna element spacing, non-uniform

CHAPTER 5. BEAMFORMED MILLIMETER-WAVE FULL-DIMENSIONAL MIMO CHANNEL ESTIMATION BASED ON ATOMIC NORM MINIMIZATION

planar array (NUPA) requires fewer elements than UPA, whereby reducing the weight and cost of the system in large array applications. Also, the irregular spacing allows the antenna grid spacing to become larger than a half wavelength so it can effectively reduce the channel correlation and enhance multiplexing gain [Torkildson *et al.*, 2009]. Furthermore, there is a fundamental limitation of UPA, namely, the lower resolution of elevation AoA, which limits the UPA performance [Liu *et al.*, 2017].

In this section we consider the beamformed mmWave FD-MIMO channel estimation for NUPA. Define $\mathbf{d}_t = \frac{2}{\lambda} [(d_{t,1}(1), d_{t,2}(1)) \dots (d_{t,1}(N), d_{t,2}(N))]$ as the normalized transmit antenna locations, where $(d_{t,1}(i), d_{t,2}(i))$ is the i -th transmit antenna coordinate in a 2D planar surface. Similarly, $\mathbf{d}_r = \frac{2}{\lambda} [(d_{r,1}(1), d_{r,2}(1)) \dots (d_{r,1}(M), d_{r,2}(M))]$ is the normalized receive antenna locations where $(d_{r,1}(i), d_{r,2}(i))$ is the i -th receive antenna coordinate in a 2D planar surface. Then the steering responses of the transmit and receive arrays for the l -th path can be respectively written as [Nai *et al.*, 2010]

$$\mathbf{a}_{\mathbf{d}_t}(\mathbf{g}_l) = \frac{1}{\sqrt{N}} \left[e^{j2\pi \left(\frac{2d_{t,1}(1)}{\lambda} g_{l,1} + \frac{2d_{t,2}(1)}{\lambda} g_{l,2} \right)} \dots e^{j2\pi \left(\frac{2d_{t,1}(N)}{\lambda} g_{l,1} + \frac{2d_{t,2}(N)}{\lambda} g_{l,2} \right)} \right]^T \quad (5.60)$$

$$\mathbf{b}_{\mathbf{d}_r}(\mathbf{f}_l) = \frac{1}{\sqrt{M}} \left[e^{j2\pi \left(\frac{2d_{r,1}(1)}{\lambda} f_{l,1} + \frac{2d_{r,2}(1)}{\lambda} f_{l,2} \right)} \dots e^{j2\pi \left(\frac{2d_{r,1}(M)}{\lambda} f_{l,1} + \frac{2d_{r,2}(M)}{\lambda} f_{l,2} \right)} \right]^T \quad (5.61)$$

With (5.60) and (5.61), the channel matrix \mathbf{H} of NUPA is given by (5.1) with array responses $\mathbf{a}(\mathbf{g}_l)$ and $\mathbf{b}(\mathbf{f}_l)$ replaced by $\mathbf{a}_{\mathbf{d}_t}(\mathbf{g}_l)$ and $\mathbf{b}_{\mathbf{d}_r}(\mathbf{f}_l)$, respectively.

The atom for NUPA is then defined as

$$\mathbf{q}_{\text{NU}}(\mathbf{g}, \mathbf{f}) = \mathbf{a}_{\mathbf{d}_t}^*(\mathbf{g}) \otimes \mathbf{b}_{\mathbf{d}_r}(\mathbf{f}). \quad (5.62)$$

And the atom set for NUPA is given by

$$\mathcal{A}_{\text{NU}} \triangleq \left\{ \mathbf{q}_{\text{NU}}(\mathbf{g}, \mathbf{f}), \mathbf{g} \in \left[-\frac{1}{2}, \frac{1}{2}\right) \times \left[-\frac{1}{2}, \frac{1}{2}\right), \mathbf{f} \in \left[-\frac{1}{2}, \frac{1}{2}\right) \times \left[-\frac{1}{2}, \frac{1}{2}\right) \right\}. \quad (5.63)$$

The atomic norm $\|\mathbf{h}\|_{\mathcal{A}_{\text{NU}}}$ for any $\mathbf{h} = \text{vec}(\mathbf{H})$ is then given by

$$\|\mathbf{h}\|_{\mathcal{A}_{\text{NU}}} = \inf_{\substack{\mathbf{f}_l \in \left[-\frac{1}{2}, \frac{1}{2}\right) \times \left[-\frac{1}{2}, \frac{1}{2}\right), \\ \mathbf{g}_l \in \left[-\frac{1}{2}, \frac{1}{2}\right) \times \left[-\frac{1}{2}, \frac{1}{2}\right), \\ \sigma_l \in \mathbb{C}}} \left\{ \sum_l |\sigma_l| \left| \mathbf{h} = \sum_l \sigma_l \mathbf{q}_{\text{NU}}(\mathbf{g}_l, \mathbf{f}_l) \right| \right\}. \quad (5.64)$$

CHAPTER 5. BEAMFORMED MILLIMETER-WAVE FULL-DIMENSIONAL MIMO CHANNEL ESTIMATION BASED ON ATOMIC NORM MINIMIZATION

To estimate the channel, we propose to solve the following optimization problem

$$\min_{\mathbf{h}} \mu \|\mathbf{h}\|_{\mathcal{A}_{\text{NU}}} + \frac{1}{2} \left\| \mathbf{y} - \sqrt{P_t} (\mathbf{P}^T \otimes \mathbf{I}_M) \mathbf{h} \right\|_2^2. \quad (5.65)$$

Note that the atom defined in (5.62) is not based on uniform sampling, and consequently the atomic norm in (5.64) does not have the equivalent SDP form as in (5.28) or (5.43). Hence, (5.65) cannot be solved via convex optimization. According to Corollary 2.1 of [Li and Tang, 2016], (5.65) shares the same optimum as the following optimization problem

$$\min_{\substack{\mathbf{f}_l \in [-\frac{1}{2}, \frac{1}{2}] \times [-\frac{1}{2}, \frac{1}{2}], \\ \mathbf{g}_l \in [-\frac{1}{2}, \frac{1}{2}] \times [-\frac{1}{2}, \frac{1}{2}], \\ \sigma_l \in \mathbb{C}}} \Gamma(\{\mathbf{g}_l, \mathbf{f}_l, \sigma_l\}) = \mu \|\boldsymbol{\sigma}\|_1 + \frac{1}{2} \left\| \mathbf{y} - \sqrt{P_t} (\mathbf{P}^T \otimes \mathbf{I}_M) \sum_{l=1}^L \mathbf{q}_{\text{NU}}(\mathbf{g}_l, \mathbf{f}_l) \sigma_l \right\|_2^2. \quad (5.66)$$

Since the problem given by (5.66) is nonconvex, we will employ a gradient-descent algorithm to obtain its local optimum. In practice, L is unknown, so we initialize $\mathbf{q}(\mathbf{g}_l, \mathbf{f}_l)$ on \tilde{L}^0 grid points such that $L \leq \tilde{L}^0 \leq MP$, where P is the number of training beams defined in (5.8). For example, let each \mathbf{g}_l and \mathbf{f}_l be taken from a uniform grid of N_G points with $\tilde{L}^0 = N_G^4 \leq MP$, i.e., $g_{l,i}^0$ and $f_{l,i}^0$ are uniformly taken from $[-1/2, 1/2)$ for $i = 1, 2$ and $1 \leq l \leq N_G^4$, where the superscript 0 indicates iteration 0, i.e., initialization. Let $\boldsymbol{\Omega}^0 = \{(\mathbf{g}_l^0, \mathbf{f}_l^0)_{1 \leq l \leq \tilde{L}^0}\}$. The initial value of $\boldsymbol{\sigma}^0 = [\sigma_1^0 \dots \sigma_{\tilde{L}^0}^0]^T$ can then be obtained by the least-squares (LS) estimate

$$\boldsymbol{\sigma}^0 = ((\mathbf{P}^T \otimes \mathbf{I}_M) [\mathbf{q}_{\text{NU}}(\mathbf{g}_1^0, \mathbf{f}_1^0) \dots \mathbf{q}_{\text{NU}}(\mathbf{g}_{\tilde{L}^0}^0, \mathbf{f}_{\tilde{L}^0}^0)])^\dagger \mathbf{y}, \quad (5.67)$$

where † indicates the pseudo inverse of the matrix. Then the gradient descent method is used to find the local optimum. We use superscript k to denote the quantities in the k -th iteration. Then the gradient descent search proceeds as follows

$$g_{l,i}^{k+1} = [g_{l,i}^k - \kappa^k \nabla_{g_{l,i}} \Gamma(\{\mathbf{g}_l^k, \mathbf{f}_l^k, \sigma_l^k\})]_{-\frac{1}{2}}^{\frac{1}{2}}, \quad (5.68)$$

$$f_{l,i}^{k+1} = [f_{l,i}^k - \kappa^k \nabla_{f_{l,i}} \Gamma(\{\mathbf{g}_l^k, \mathbf{f}_l^k, \sigma_l^k\})]_{-\frac{1}{2}}^{\frac{1}{2}}, \quad (5.69)$$

$$\sigma_l^{k+1} = \sigma_l^k - \kappa^k \nabla_{\sigma_l} \Gamma(\{\mathbf{g}_l^k, \mathbf{f}_l^k, \sigma_l^k\}), \quad (5.70)$$

for $l = 1, \dots, \tilde{L}^k$ and $i = 1, 2$, where κ^k is the step size that can be obtained via Armijo line search [Boumal and Absil, 2015] and $[x]_b^a$ defines the operator that outputs

CHAPTER 5. BEAMFORMED MILLIMETER-WAVE FULL-DIMENSIONAL MIMO CHANNEL ESTIMATION BASED ON ATOMIC NORM MINIMIZATION

$x = \text{mod}(x, a)$ when $x < b$, and outputs $x = \text{mod}(x, b)$ when $x > a$, $\text{mod}(a, b)$ defines the modulo operator. Specifically, in the k -th iteration, κ^k is initialized as $\kappa^k = \bar{\kappa}$. If $\Gamma(\{\mathbf{g}_l^{k+1}, \mathbf{f}_l^{k+1}, \sigma_l^{k+1}\}) \geq \Gamma(\{\mathbf{g}_l^k, \mathbf{f}_l^k, \sigma_l^k\})$, then κ^k is updated by multiplication with a constant $0 < \alpha < 1$, i.e., $\kappa^k \leftarrow \alpha \kappa^k$. The gradients are calculated

$$\nabla_{g_{l,i}} \Gamma(\{\mathbf{g}_l, \mathbf{f}_l, \sigma_l\}) = \mathcal{R} \left\{ \sigma_l \left(\bar{\mathbf{P}} \sum_{l=1}^{\tilde{L}} \mathbf{q}_{\text{NU}}(\mathbf{g}_l, \mathbf{f}_l) \sigma_l - \mathbf{y} \right)^H \bar{\mathbf{P}} (\mathbf{a}_{\mathbf{d}_{t,i}}^*(\mathbf{g}_l) \otimes \mathbf{b}_{\mathbf{d}_r}(\mathbf{f}_l)) \right\}, \quad (5.71)$$

$$\nabla_{f_{l,i}} \Gamma(\{\mathbf{g}_l, \mathbf{f}_l, \sigma_l\}) = \mathcal{R} \left\{ \sigma_l \left(\bar{\mathbf{P}} \sum_{l=1}^{\tilde{L}} \mathbf{q}_{\text{NU}}(\mathbf{g}_l, \mathbf{f}_l) \sigma_l - \mathbf{y} \right)^H \bar{\mathbf{P}} (\mathbf{a}_{\mathbf{d}_t}^*(\mathbf{g}_l) \otimes \mathbf{b}_{\mathbf{d}_{r,i}}(\mathbf{f}_l)) \right\}, \quad (5.72)$$

$$\nabla_{\sigma_l} \Gamma(\{\mathbf{g}_l, \mathbf{f}_l, \sigma_l\}) = \mu \frac{\sigma_l}{2|\sigma_l|} + \frac{1}{2} \left(\bar{\mathbf{P}} \sum_{l=1}^{\tilde{L}} \mathbf{q}_{\text{NU}}(\mathbf{g}_l, \mathbf{f}_l) \sigma_l - \mathbf{y} \right)^T (\bar{\mathbf{P}} \mathbf{q}_{\text{NU}}(\mathbf{g}_l, \mathbf{f}_l))^*, \quad (5.73)$$

where $\mathcal{R}\{\cdot\}$ returns the real part of the input,

$$\bar{\mathbf{P}} = \sqrt{P_t} (\mathbf{P}^T \otimes \mathbf{I}_M), \quad (5.74)$$

$$\mathbf{a}_{\mathbf{d}_{t,i}}(\mathbf{g}_l) = \left(\frac{j2\pi}{\lambda} [d_{t,i}(1), \dots, d_{t,i}(N)]^T \right) \circ \mathbf{a}_{\mathbf{d}_t}(\mathbf{g}_l), \quad (5.75)$$

$$\mathbf{b}_{\mathbf{d}_{r,i}}(\mathbf{f}_l) = \left(\frac{j2\pi}{\lambda} [d_{r,i}(1), \dots, d_{r,i}(M)]^T \right) \circ \mathbf{b}_{\mathbf{d}_r}(\mathbf{f}_l), \quad (5.76)$$

and \circ denotes Hadamard product. The derivations of (5.71) - (5.73) are given in the Appendix. To accelerate the convergence, we introduce a pruning step to remove the atoms whose coefficients are smaller than a threshold during each iteration. Specifically, at the k -th iteration, if $|\sigma_l^k| < \eta^k$ where η^k is a given threshold at the k -th iteration, then l -th path are removed from the set and number of estimated paths is decreased by one, i.e., $\boldsymbol{\Omega}^k \leftarrow \boldsymbol{\Omega}^k \setminus \{(\mathbf{g}_l^k, \mathbf{f}_l^k)\}$ and $\tilde{L}^k \leftarrow \tilde{L}^k - 1$ at the k -th iteration. The algorithm stops when $\|\mathbf{h}^{k+1} - \mathbf{h}^k\| < \varepsilon$, where $\mathbf{h}^k = \sum_{l=1}^{\tilde{L}^k} \mathbf{q}_{\text{NU}}(\mathbf{g}_l^k, \mathbf{f}_l^k) \sigma_l^k$ denotes the channel estimation at the k -th iteration.

5.6 Simulation Results

5.6.1 Simulation Setup

In this section, we evaluate the performance of the proposed channel estimators for mmWave FD-MIMO links with UPA or NUPA. We compare the channel estimation performance of the proposed algorithm with some existing algorithms including the 4D-MUSIC [Guo *et al.*, 2017] and the orthogonal matching pursuit (OMP) [Cai and Wang, 2011]. The simulation parameters are set as follows.

- 1, The numbers of transmit and receive antenna are $N = 16$ and $M = 16$, respectively. For UPA, we set $N_1 = 4$, $N_2 = 4$, $M_1 = 4$ and $M_2 = 4$.
- 2, In the UPA case, the DFT codebooks at the transmitter for elevation and azimuth are given by

$$\begin{aligned}\mathbf{P}_1 &= [\mathbf{c}_{N_1}(\psi_{1,0}) \ \mathbf{c}_{N_1}(\psi_{1,1}) \cdots \mathbf{c}_{N_1}(\psi_{1,P_1-1})] \in \mathbb{C}^{N_1 \times P_1}, \\ \mathbf{P}_2 &= [\mathbf{c}_{N_2}(\psi_{2,0}) \ \mathbf{c}_{N_2}(\psi_{2,1}) \cdots \mathbf{c}_{N_2}(\psi_{2,P_2-1})] \in \mathbb{C}^{N_2 \times P_2},\end{aligned}$$

where P_1 and P_2 are the sizes of elevation and azimuth codebooks, respectively. The DFT angles are $\psi_{1,i} = \frac{i}{P_1}$ for $i = 0, \dots, P_1 - 1$ and $\psi_{2,i} = \frac{i}{P_2}$ for $i = 0, \dots, P_2 - 1$. We take the Kronecker product of \mathbf{P}_1 and \mathbf{P}_2 to form the product codebook $\mathbf{P} = \mathbf{P}_1 \otimes \mathbf{P}_2$ with size $P = P_1 P_2$. Each beamforming vector has a unit norm, i.e., $\|\mathbf{p}_p\| = 1$ for $p = 1, \dots, P$ and $\text{rank}(\mathbf{P}) = P$.

- 3, The weight factor in (5.28) and (5.43) is set as $\mu = \sigma_w \sqrt{MN \log(MN)}$. The weight for the augmented Lagrangian in (5.45) is set as $\rho = 0.05$.
- 4, \mathbf{g}_l and \mathbf{f}_l for each path are assumed to uniformly take values in $[-\frac{1}{2}, \frac{1}{2}) \times [-\frac{1}{2}, \frac{1}{2})$. The number of paths $L = 3$.
- 5, The signal power is controlled by the signal-to-noise ratio (SNR) which is defined as $\text{SNR} = \frac{P_t}{\sigma_w^2}$ with $\sigma_w^2 = 1$.

CHAPTER 5. BEAMFORMED MILLIMETER-WAVE FULL-DIMENSIONAL MIMO CHANNEL ESTIMATION BASED ON ATOMIC NORM MINIMIZATION

- 6, For NUPA, we use circular arrays for both transmitter and receiver with N and M antenna elements located on the 2D plane, respectively. Specifically, the n -th transmit antenna location is set as $d_{t,1}(n) = R_t \cos(\chi_n)$, $d_{t,2}(n) = R_t \sin(\chi_n)$, $n = 1, 2, \dots, N$, where $\chi_n = 2\pi \left(\frac{n}{N}\right)$ is the angular position of the n -th element and R_t is the radius of the transmit array. Similarly, the m -th receive antenna location is $d_{r,1}(m) = R_r \cos(\chi_m)$, $d_{r,2}(m) = R_r \sin(\chi_m)$, $m = 1, 2, \dots, M$, where $\chi_m = 2\pi \left(\frac{m}{M}\right)$ is the angular position of the m -th element and R_r is the radius of the receive array.
- 7, For the gradient descent algorithm, we set $\tilde{L}^0 = MP$ as the initial value in both UPA and NUPA cases. The pruning threshold in the k -th step is set as $\eta^k = 0.7 \max_{1 \leq l \leq \tilde{L}^k} \{\sigma_l^k\}$.
- 8, For the OMP and 4D-MUSIC algorithms, the AoD and AoA grid points are set as $\bar{\vartheta}_i = \frac{(i-1)2\pi}{N_G} - \pi$, $\bar{\varphi}_i = \frac{(i-1)2\pi}{N_G} - \pi$ and $\bar{\theta}_i = \frac{(i-1)2\pi}{N_G} - \pi$, $\bar{\phi}_i = \frac{(i-1)2\pi}{N_G} - \pi$, respectively, for $i = 1, \dots, N_G$.
- 9, In the simulation, we use the CVX package [Grant and Boyd, 2014] to compute the 4D atomic norm-based estimator.

5.6.2 Performance Evaluation

We use the normalized mean square error (NMSE), i.e., $\text{NMSE} = \mathbb{E} \left\{ \frac{\|\hat{\mathbf{H}} - \mathbf{H}\|_F^2}{\|\mathbf{H}\|_F^2} \right\}$ as the channel estimation performance metric. The NMSE statistics across different SNRs with different test setups are evaluated. Each curve is obtained by averaging over 100 realizations. First we compare the channel estimation performance of different algorithms under the UPA setting. Then we show the channel estimation performance for NUPA with the proposed gradient descent estimator and compare it with the 4D-MUSIC and OMP algorithms.

The computational complexity of the proposed approximate 4D atomic-norm-based channel estimator is $\mathcal{O}((M + N)^3)$ per-iteration. The computational complex-

ity of the MUSIC estimator is $\mathcal{O}((NM)^3 + N_G^4(NM)^2)$ where $\mathcal{O}((NM)^3)$ is for eigen decomposition and $\mathcal{O}(N_G^4(NM)^2)$ is for grid search. The complexity of the OMP estimator is $\mathcal{O}(N_G^4(NM)^2)$ per iteration. The complexity of proposed gradient descent estimator is $\mathcal{O}(M(N+P))$ per iteration.

5.6.2.1 Convergence Behavior of the Proposed Channel Estimators

We illustrate the convergence of the proposed ADMM implementation of the approximate 4D atomic-norm-based channel estimator through a simulation example. We compare the NMSE of the ADMM channel estimator with that of the CVX solver [Grant and Boyd, 2014] that directly solves (5.43). As can be seen from Fig. 5.2, 5.3, the proposed ADMM channel estimator converges to the solution given by the CVX after 300-400 iterations for different SNR. It is worth noting that the ADMM runs much faster than the CVX solver because the calculation in each iteration is in closed-form.

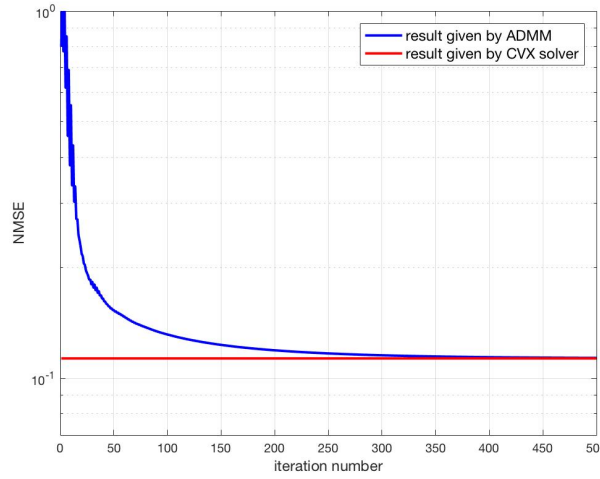


Figure 5.2: Convergence of proposed ADMM channel estimator with different SNR
(a) SNR= 4dB.

CHAPTER 5. BEAMFORMED MILLIMETER-WAVE FULL-DIMENSIONAL MIMO CHANNEL ESTIMATION BASED ON ATOMIC NORM MINIMIZATION

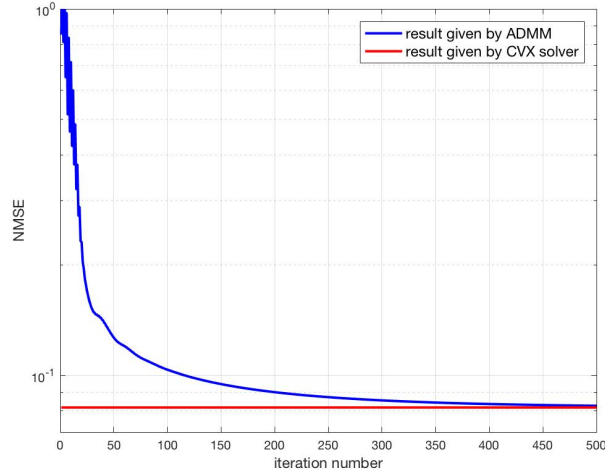


Figure 5.3: Convergence of proposed ADMM channel estimator with different SNR
(b) SNR= 10dB.

We then show the convergence behavior and the number of estimated paths of the proposed gradient-descent-based channel estimator for UPA and NUPA in Fig. 5.4-5.7. It is seen that the algorithm converges within 1500-2000 iterations for different SNR. The estimated number of paths is more accurate at higher SNR when the algorithm converges, as more spurious frequencies arise when the noise is stronger. It is also worth noting that the computational complexity of the gradient descent method is lower than that of the ADMM, but the overall running time is higher because it takes more iterations.

CHAPTER 5. BEAMFORMED MILLIMETER-WAVE FULL-DIMENSIONAL
MIMO CHANNEL ESTIMATION BASED ON ATOMIC NORM MINIMIZATION

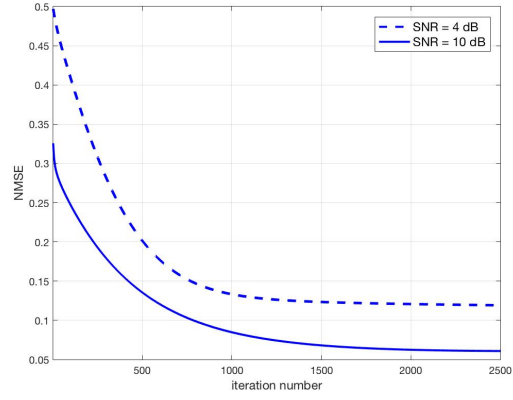


Figure 5.4: (a)

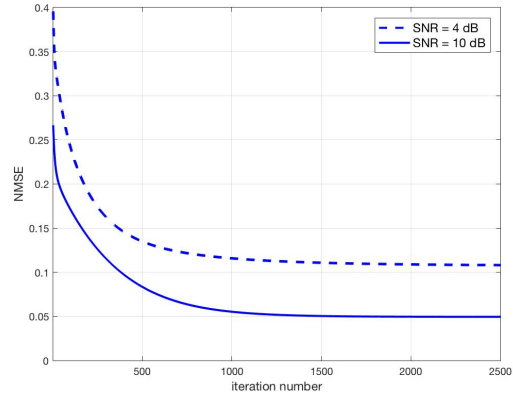


Figure 5.5: (b)

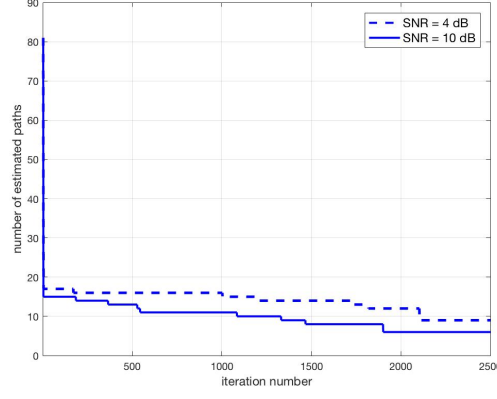


Figure 5.6: (c)

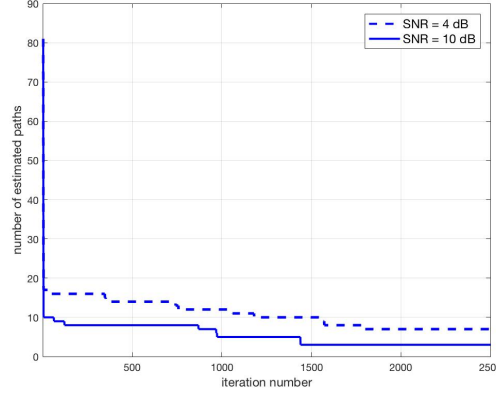


Figure 5.7: Convergence and the number of estimated paths of the proposed gradient descent algorithm for (a)(c) UPA and (b)(d) NUPA.

5.6.2.2 Comparison of On-grid and Off-grid Algorithms

We compare the proposed off-grid channel estimator with two existing on-grid approaches including OMP and MUSIC. For the on-grid algorithms, the continuous AoA and AoD parameter spaces are discretized into a finite set of grids covering $[-\pi, \pi]$, and the estimation performance improves with higher grid resolution (i.e., larger N_G). However, higher grid resolution leads to higher computational complexity.

In Fig. 5.8 and 5.9, the NMSE and running time of different channel estimators

CHAPTER 5. BEAMFORMED MILLIMETER-WAVE FULL-DIMENSIONAL MIMO CHANNEL ESTIMATION BASED ON ATOMIC NORM MINIMIZATION

are plotted against N_G . In this simulation, we use CVX solver to compute the 4D atomic-norm-based estimator and the ADMM algorithm to compute the approximate 4D atomic-norm-based estimator. It is worth noting that the proposed approximate 4D atomic-norm-based estimator has the smallest complexity while its NMSE is much smaller than those of the on-grid algorithms. As the algorithm does not require the grids, its computational complexity does not change with N_G . In addition, its NMSE performance is only slightly worse than the 4D atomic-norm-based channel estimator, indicating that the performance loss caused by the approximation of $\|\mathbf{H}\|_{\mathcal{A}_M}$ by $\text{SDP}(\mathbf{H})$ is small.

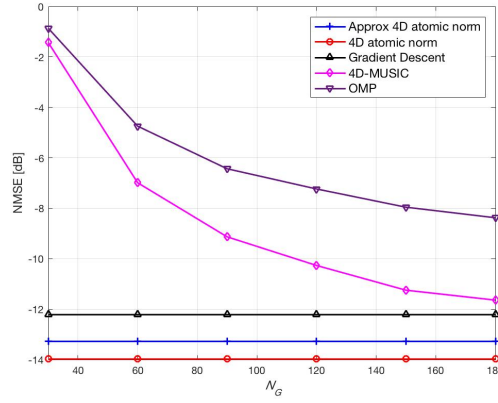


Figure 5.8: Comparison of channel estimation performance and running time against grid size, SNR= 10dB. (a) NMSE performance

CHAPTER 5. BEAMFORMED MILLIMETER-WAVE FULL-DIMENSIONAL MIMO CHANNEL ESTIMATION BASED ON ATOMIC NORM MINIMIZATION

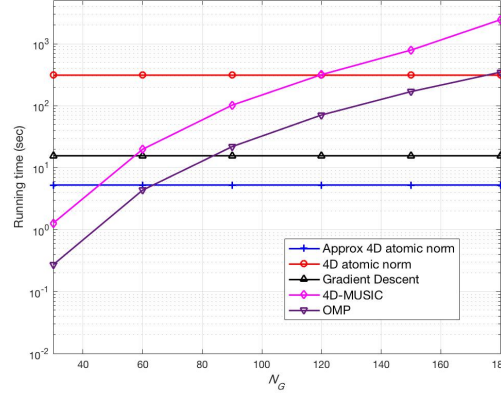


Figure 5.9: Comparison of channel estimation performance and running time against grid size, SNR= 10dB. (b) running time.

5.6.2.3 Channel Estimation Performance

Fig. 5.10 plots the NMSE curves as a function of SNR for different channel estimators under UPA. The number of grid points are set as $N_G = 90, 180$ for 4D-MUSIC-based and OMP-based channel estimators.

It is seen that 4D atomic-norm-based and approximate 4D atomic-norm-based estimators outperform the 4D-MUSIC-based and OMP-based estimators. Meanwhile, the 4D atomic-norm-based channel estimator achieves better performance than the approximate 4D atomic-norm-based channel estimator by about from 0.5 - 0.8 dB. And the approximate 4D atomic-norm-based channel estimator outperforms the gradient-descent-based algorithm by more than 1.0 dB.

CHAPTER 5. BEAMFORMED MILLIMETER-WAVE FULL-DIMENSIONAL MIMO CHANNEL ESTIMATION BASED ON ATOMIC NORM MINIMIZATION

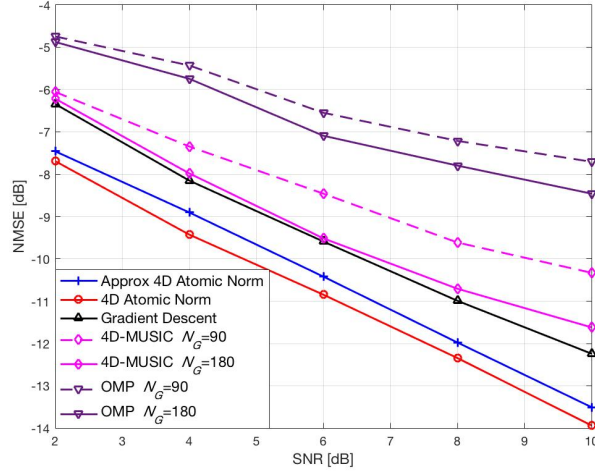


Figure 5.10: The NMSE performance as a function of SNR for UPA.

In Fig. 5.11, we plot the NMSE curves as a function of SNR for different channel estimators under NUPA. It is seen that the proposed gradient-descent-based channel estimator outperforms the 4D-MUSIC and OMP-based channel estimators across the range of SNRs from 2 to 10 dB. This is because the proposed gradient-descent-based channel estimator optimizes the frequency basis in each iteration, so it outperforms the on-grid algorithms.

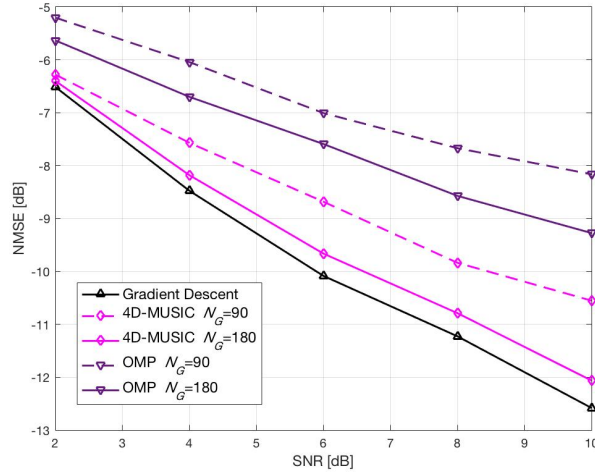


Figure 5.11: The NMSE performance as a function of SNR for NUPA.

5.7 Conclusions

In this paper, we have proposed new channel estimation schemes for mmWave beamformed FD-MIMO systems based on atomic norm minimization under both UPA and NUPA settings. For the UPA case, we approximate the original large-scale 4D atomic norm minimization problem using a semi-definite program (SDP) containing two decoupled two-level Toeplitz matrices which is then solved by an ADMM-based fast algorithm. For the NUPA case, a gradient descent-based algorithm is provided to obtain a suboptimal solution. Simulation results show that the proposed atomic norm based mmWave FD-MIMO channel estimators provide better performance compared to the existing methods based on compressed sensing and MUSIC algorithms.

5.0.1 Derivation for (5.71) and (5.72)

For clarity, define $\bar{\mathbf{P}} = \sqrt{P_t} (\mathbf{P}^T \otimes \mathbf{I}_M)$. Then the gradient with respect to $g_{l,i}$ can be calculated by

$$\nabla_{g_{l,i}} \Gamma(\{\mathbf{g}_l, \mathbf{f}_l, \sigma_l\}) = \frac{1}{2} \frac{\partial (\mathbf{y} - \bar{\mathbf{P}}\mathbf{h})^H (\mathbf{y} - \bar{\mathbf{P}}\mathbf{h})}{\partial g_{l,i}} = \mathcal{R} \left\{ (\bar{\mathbf{P}}\mathbf{h} - \mathbf{y})^H \frac{\partial \bar{\mathbf{P}}\mathbf{h}}{\partial g_{l,i}} \right\}, \quad (77)$$

where

$$\frac{\partial \bar{\mathbf{P}}\mathbf{h}}{\partial g_{l,i}} = \frac{\partial \bar{\mathbf{P}} \sum_{l=1}^L \mathbf{q}_{\text{NU}}(\mathbf{g}_l, \mathbf{f}_l) \sigma_l}{\partial g_{l,i}} = \sigma_l \bar{\mathbf{P}} \frac{\partial \mathbf{q}_{\text{NU}}(\mathbf{g}_l, \mathbf{f}_l)}{\partial g_{l,i}}, \quad (78)$$

$$\frac{\partial \mathbf{q}_{\text{NU}}(\mathbf{g}_l, \mathbf{f}_l)}{\partial g_{l,i}} = \frac{\partial \mathbf{a}_{\mathbf{d}_t}^*(\mathbf{g}_l) \otimes \mathbf{b}_{\mathbf{d}_r}(\mathbf{f}_l)}{\partial g_{l,i}} = \frac{\partial \mathbf{a}_{\mathbf{d}_t}^*(\mathbf{g}_l)}{\partial g_{l,i}} \otimes \mathbf{b}_{\mathbf{d}_r}(\mathbf{f}_l), \quad (79)$$

$$\frac{\partial \mathbf{a}_{\mathbf{d}_t}^*(\mathbf{g}_l)}{\partial g_{l,i}} = \left(\frac{-j2\pi}{\lambda} [d_{t,i}(1), \dots, d_{t,i}(N)]^T \right) \circ \mathbf{a}_{\mathbf{d}_t}^*(\mathbf{g}_l). \quad (80)$$

By plugging (80) into (77), we have (5.71). Similarly we can obtain (5.72).

5.0.2 Derivation for (5.73)

The gradient with respect to σ_l can be calculated by

$$\begin{aligned}\nabla_{\sigma_l} \Gamma(\{\mathbf{g}_l, \mathbf{f}_l, \sigma_l\}) &= \frac{\partial \left(\mu \|\boldsymbol{\sigma}\|_1 + \frac{1}{2} \|\mathbf{y} - \bar{\mathbf{P}}\mathbf{h}\|_2^2 \right)}{\partial \sigma_l^*} \\ &= \frac{\partial \|\boldsymbol{\sigma}\|_1}{\partial \sigma_l^*} - \frac{1}{2} \frac{\partial \mathbf{y}^H \bar{\mathbf{P}}\mathbf{h}}{\partial \sigma_l^*} - \frac{1}{2} \frac{\partial \mathbf{h}^H \bar{\mathbf{P}}^H \mathbf{y}}{\partial \sigma_l^*} + \frac{1}{2} \frac{\partial \mathbf{h}^H \bar{\mathbf{P}}^H \bar{\mathbf{P}}\mathbf{h}}{\partial \sigma_l^*},\end{aligned}\quad (81)$$

where

$$\frac{\partial \mathbf{y}^H \bar{\mathbf{P}}\mathbf{h}}{\partial \sigma_l^*} = \mathbf{y}^H \bar{\mathbf{P}} \mathbf{q}_{\text{NU}}(\mathbf{g}_l, \mathbf{f}_l) \frac{\partial \sigma_l}{\partial \sigma_l^*} = 0, \quad (82)$$

$$\frac{\partial \mathbf{h}^H \bar{\mathbf{P}}^H \mathbf{y}}{\partial \sigma_l^*} = \left((\bar{\mathbf{P}} \mathbf{q}_{\text{NU}}(\mathbf{g}_l, \mathbf{f}_l))^H \mathbf{y} \right)^T \frac{\partial \sigma_l^*}{\partial \sigma_l^*} = \left((\bar{\mathbf{P}} \mathbf{q}_{\text{NU}}(\mathbf{g}_l, \mathbf{f}_l))^H \mathbf{y} \right)^T, \quad (83)$$

$$\frac{\partial \mathbf{h}^H \bar{\mathbf{P}}^H \bar{\mathbf{P}}\mathbf{h}}{\partial \sigma_l^*} = \left((\bar{\mathbf{P}} \mathbf{q}_{\text{NU}}(\mathbf{g}, \mathbf{f}))^H \bar{\mathbf{P}} \mathbf{q}_{\text{NU}}(\mathbf{g}_l, \mathbf{f}_l) \sigma_l \right)^T, \quad (84)$$

$$\begin{aligned}\frac{\partial \|\boldsymbol{\sigma}\|_1}{\partial \sigma_l^*} &= \frac{\partial \sum_l |\sigma_l|}{\partial \sigma_l^*} = \frac{\partial |\sigma_l|}{\partial \sigma_l^*} = \frac{1}{2} \left(\frac{\partial |\sigma_l|}{\partial \mathcal{R}\{\sigma_l\}} + i \frac{\partial |\sigma_l|}{\partial \mathcal{I}\{\sigma_l\}} \right) \\ &= \frac{1}{2} \left(\frac{\partial \sqrt{\mathcal{R}^2\{\sigma_l\} + \mathcal{I}^2\{\sigma_l\}}}{\partial \mathcal{R}\{\sigma_l\}} + i \frac{\partial \sqrt{\mathcal{R}^2\{\sigma_l\} + \mathcal{I}^2\{\sigma_l\}}}{\partial \mathcal{I}\{\sigma_l\}} \right) \\ &= \frac{\sigma_l}{2|\sigma_l|},\end{aligned}\quad (85)$$

where $\mathcal{I}\{\cdot\}$ returns the imaginary part of the input. Plugging (82)-(85) into (81), we obtain (5.73).

Bibliography

- [Abidi, 1995] A. A. Abidi. Direct-conversion radio transceivers for digital communications. *IEEE J. Solid-State Circuits*, 30(12):1399–1410, December 1995.
- [Alkhateeb *et al.*, 2014] A. Alkhateeb, O. El Ayach, G. Leus, and R. W. Heath. Channel estimation and hybrid precoding for millimeter wave cellular systems. *IEEE Journal of Selected Topics in Signal Processing*, 8(5):831–846, Oct 2014.
- [Alkhateeb *et al.*, 2015] A. Alkhateeb, G. Leus, and R. W. Heath. Compressed sensing based multi-user millimeter wave systems: How many measurements are needed? In *2015 IEEE International Conference on Acoustics, Speech and Signal Processing (ICASSP)*, pages 2909–2913, April 2015.
- [Antoni, 2007] Jrme Antoni. Cyclic spectral analysis in practice. *Mechanical Systems and Signal Processing*, 21(2):597–630, February 2007.
- [Anttila *et al.*, 2007] Lauri Anttila, M. Valkama, and Markku Renfors. Blind compensation of frequency-selective I/Q imbalances in quadrature radio receivers: Circularity-based approach. In *Proc. IEEE Int. Symp. Control, Communications, and Signal Processing (ISCCSP’07)*, pages 245–248, 2007.
- [Anttila *et al.*, 2008] Lauri Anttila, M. Valkama, and Markku Renfors. Circularity-based I/Q imbalance compensation in wideband direct-conversion receivers. *IEEE Trans. Vehi. Tech.*, 57(4):2099–2113, July 2008.

BIBLIOGRAPHY

- [Ariananda *et al.*, 2009] D. D. Ariananda, M. K. Lakshmanan, and H. Nikoo. A survey on spectrum sensing techniques for cognitive radio. In *Cognitive Radio and Advanced Spectrum Management, CogART 2009. Second International Workshop on*, pages 74–79, 2009.
- [Ariananda *et al.*, 2011] D. D. Ariananda, G. Leus, and Z. Tian. Multi-coset sampling for power spectrum blind sensing. In *Proc. of the Int. Conf. on Digital Signal Processing (DSP)*, Corfu, Greece, July 2011.
- [Arias and et al., 2006] J. Arias and et al. A 32 mw 320 mhz continuous-time complex delta-sigma adc for multi-mode wireless-lan receivers. *IEEE J. Solid-State Circuits*, 41(2):339–351, February 2006.
- [Ayach *et al.*, 2014] O. E. Ayach, S. Rajagopal, S. Abu-Surra, Z. Pi, and R. W. Heath. Spatially sparse precoding in millimeter wave mimo systems. *IEEE Trans. Wireless Commun.*, 13(3):1499–1513, March 2014.
- [Bello, 1963] P. Bello. Characterization of randomly time-variant linear channels. *IEEE Trans. Commun.*, 11(4):360 – 393, December 1963.
- [Bhaskar *et al.*, 2013a] B. N. Bhaskar, G. Tang, and B. Recht. Atomic norm denoising with applications to line spectral estimation. *IEEE Trans. Sig. Proc.*, 61(23):5987–5999, Dec 2013.
- [Bhaskar *et al.*, 2013b] Badri Narayan Bhaskar, Gongguo Tang, and Benjamin Recht. Atomic norm denoising with applications to line spectral estimation. *IEEE Trans. Sig. Proc.*, 61(23):5987–5999, 2013.
- [Boariu and Ziemer, 2001] A. Boariu and R.E. Ziemer. Multiuser detection in multipath environments for variable spreading-factor CDMA systems. *IEEE Trans. Commun.*, 49(9):1520–1524, September 2001.

BIBLIOGRAPHY

- [Boumal and Absil, 2015] Nicolas Boumal and P-A Absil. Low-rank matrix completion via preconditioned optimization on the grassmann manifold. *Linear Algebra and its Applications*, 475:200–239, 2015.
- [Boyd *et al.*, 2011] Stephen Boyd, Neal Parikh, Eric Chu, Borja Peleato, and Jonathan Eckstein. Distributed optimization and statistical learning via the alternating direction method of multipliers. *Foundations and Trends® in Machine Learning*, 3(1):1–122, 2011.
- [Brandwood, 1983] D. H. Brandwood. A complex gradient operator and its application in adaptive array theory. *IEE Proc., Parts F and H*, 130(1):11–16, February 1983.
- [Brillinger, 1981] D.R. Brillinger. *Time Series: Data Analysis and Theory*. San Francisco, CA, Holden-Day, 1981.
- [Cai and Wang, 2011] T. T. Cai and L. Wang. Orthogonal matching pursuit for sparse signal recovery with noise. *IEEE Trans. Inform. Theory*, 57(7):4680–4688, July 2011.
- [Cai *et al.*, 2004] X. Cai, S. Zhou, and G. B. Giannakis. Group-orthogonal multicarrier CDMA systems. *IEEE Trans. Commun.*, 52(1):90–99, January 2004.
- [Candès and Fernandez-Granda, 2014] Emmanuel J Candès and Carlos Fernandez-Granda. Towards a mathematical theory of super-resolution. *Communications on Pure and Applied Mathematics*, 67(6):906–956, 2014.
- [Cheng *et al.*, 2014] X. Cheng, B. Yu, L. Yang, J. Zhang, G. Liu, Y. Wu, and L. Wan. Communicating in the real world: 3d mimo. *IEEE Wireless Communications*, 21(4):136–144, August 2014.

BIBLIOGRAPHY

- [Chi and Chen, 2013] Y. Chi and Y. Chen. Compressive recovery of 2-d off-grid frequencies. In *2013 Asilomar Conference on Signals, Systems and Computers*, pages 687–691, Nov 2013.
- [Chi and Chen, 2015] Yuejie Chi and Yuxin Chen. Compressive two-dimensional harmonic retrieval via atomic norm minimization. *IEEE Trans. Sig. Proc.*, 63(4):1030–1042, 2015.
- [Choi *et al.*, 2015] J. Choi, K. Lee, D. J. Love, T. Kim, and R. W. Heath. Advanced limited feedback designs for fd-mimo using uniform planar arrays. In *2015 IEEE Global Communications Conference (GLOBECOM)*, pages 1–6, Dec 2015.
- [Chu, 1972] David C Chu. Polyphase codes with good periodic correlation properties. *IEEE Trans. Inform. Theory*, 18(4):531–532, July 1972.
- [Conolly and Good, 1977] B. Conolly and I. J. Good. A table of discrete fourier transform pairs. *SIAM Journal on Applied Mathematics*, 32:810–822, June 1977.
- [Dahlman *et al.*, 2011] E. Dahlman, S. Parkvall, and J. Skold. *4G: LTE/LTE-Advanced for Mobile Broadband*. Academic Press, USA, 2011.
- [Dandawate and B.Giannakis, 1994] A. V. Dandawate and G. B.Giannakis. Nonparametric polyspectral estimators for kth-order (almost) cyclostationary processes. *IEEE Trans. Inform. Theory*, 40(1):67–84, January 1994.
- [Donoho, 2006a] D. Donoho. Compressed sensing. *IEEE Trans. Inform. Theory*, 52(4):1289–1306, 2006.
- [Donoho, 2006b] D. L. Donoho. Compressed sensing. *IEEE Trans. Inform. Theory*, 52(4):1289–1306, April 2006.
- [Farhang-Boroujeny, 2008] B. Farhang-Boroujeny. Filter bank spectrum sensing for cognitive radios. *IEEE Trans. Sig. Proc.*, 56(5):1801–1811, May 2008.

BIBLIOGRAPHY

- [Feng and Bresler, 2006] P. Feng and Y. Bresler. Spectrum-blind minimum-rate sampling and reconstruction of multiband signals. In *Proc. IEEE Int. Conf. ASSP*, pages 1950–1962, 2006.
- [Frank and Zadoff, 1962] Robert L Frank and S. A. Zadoff. Phase shift pulse codes with good periodic correlation properties. *IRE Transactions on Information Theory*, 8(6):381–382, October 1962.
- [Gardner *et al.*, 2006] W. A. Gardner, A. Napolitano, and L. Paura. Cyclostationarity: half a century of research. *Signal Processing, EURASIP*, 86:639–697, 2006.
- [Gardner, 1988] W. A. Gardner. *Statistical Spectral Analysis: A Non-Probabilistic Theory*. Prentice Hall, 1988.
- [Gershman and Sidiropoulos, 2005] A. B. Gershman and N. D. Sidiropoulos. *Space-Time Processing for MIMO Communications*. Wiley, 2005.
- [Grant and Boyd, 2014] Michael Grant and Stephen Boyd. CVX: Matlab software for disciplined convex programming, version 2.1. <http://cvxr.com/cvx>, March 2014.
- [Guo *et al.*, 2017] Z. Guo, X. Wang, and W. Heng. Millimeter-wave channel estimation based on two-dimensional beamspace music method. *IEEE Transactions on Wireless Communications*, PP(99), 2017.
- [Gupta and Kar, 2015] P. Gupta and S. P. Kar. Music and improved music algorithm to estimate direction of arrival. In *2015 International Conference on Communications and Signal Processing (ICCSP)*, pages 0757–0761, April 2015.
- [H. Torii and Suehiro, 2004] M. Nakamura H. Torii and N. Suehiro. A new class of zero correlation zone sequences. *IEEE Trans. Inform. Theory*, 50(3):559–565, March 2004.

BIBLIOGRAPHY

- [Han and Lee, 2005] Seung Hee Han and Jae Hong Lee. An overview of peak-to-average power ratio reduction techniques for multicarrier transmission. *IEEE Trans. Wireless Commun.*, 12(2):56–65, April 2005.
- [Han *et al.*, 2014] Yu Han, Shi Jin, Xiao Li, Yongming Huang, Lei Jiang, and Gang Wang. Design of double codebook based on 3d dual-polarized channel for multiuser mimo system. *EURASIP Journal on Advances in Signal Processing*, 2014(1):111, 2014.
- [Hara and Prasad, 1997] S. Hara and R. Prasad. Overview of multicarrier CDMA. *IEEE Wireless Commun. Mag.*, pages 126–133, 1997.
- [Haykin, 1996] S. Haykin. *Adaptive Filter Theory*. Prentice Hall, 1996.
- [Haykin, 2005] S. Haykin. Cognitive radio: brain empowered wireless communications. *IEEE Trans. Commun.*, 23(2):201–220, February 2005.
- [Hoeher, 1992] P. Hoeher. A statistical discrete-time model for the WSSUS multipath channel. *IEEE Trans. Vehi. Tech.*, 41(4):461 – 468, November 1992.
- [Højrungnes and Gesbert, 2007] Are Højrungnes and David Gesbert. Complex-valued matrix differentiation: Techniques and key results. *IEEE Trans. Sig. Proc.*, 55(6):2740–2746, June 2007.
- [Hur *et al.*, 2013] S. Hur, T. Kim, D. J. Love, J. V. Krogmeier, T. A. Thomas, and A. Ghosh. Millimeter wave beamforming for wireless backhaul and access in small cell networks. *IEEE Trans. Commun.*, 61(10):4391–4403, October 2013.
- [Jakes, 1974] W. C. Jakes. *Microwave Mobile Communications*. Wiley, 1974.
- [Jindal, 2006] N. Jindal. Mimo broadcast channels with finite-rate feedback. *IEEE Transactions on Information Theory*, 52(11):5045–5060, Nov 2006.

BIBLIOGRAPHY

- [Kiss and Prodanov, 2004] Péter Kiss and Vladimir Prodanov. One-tap wideband I/Q compensation for zero-IF filters. *IEEE Trans. Circuits Syst. I*, 51:1062–1074, June 2004.
- [Kutty and Sen, 2016] S. Kutty and D. Sen. Beamforming for millimeter wave communications: An inclusive survey. *IEEE Communications Surveys Tutorials*, 18(2):949–973, Secondquarter 2016.
- [Laska and et al., 2006] J. Laska and et al. Random sampling for analog-to-information conversion of wideband signals. In *IEEE Dallas Circuits and Systems Workshop (DCAS)*, Dallas, October 2006.
- [Lee et al., 2014] J. Lee, G. T. Gil, and Y. H. Lee. Exploiting spatial sparsity for estimating channels of hybrid mimo systems in millimeter wave communications. In *2014 IEEE Global Communications Conference*, pages 3326–3331, Dec 2014.
- [Leech, 1956] J. Leech. On the representation of $1, 2, \dots, n$ by differences. *Journal of the London Mathematical Society*, 31:160–169, April 1956.
- [Leus and Ariananda, 2011] G. Leus and D. D. Ariananda. Power spectrum blind sampling. *IEEE Signal Process. Lett.*, 18(8):443–446, August 2011.
- [Lexa et al., 2011] M. A. Lexa, M. E. Davies, J. S. Thompson, and J. Nikolic. Compressive power spectral density estimation. In *Proc. IEEE Int. Conf. on Acoustics, Speech and Signal Processing (ICASSP)*, Prague, Czech Republic, May 2011.
- [Li and Tang, 2016] Qiuwei Li and Gongguo Tang. Approximate support recovery of atomic line spectral estimation: A tale of resolution and precision. In *Signal and Information Processing (GlobalSIP), 2016 IEEE Global Conference on*, pages 153–156. IEEE, 2016.

BIBLIOGRAPHY

- [Liu *et al.*, 2017] W. Liu, Z. Wang, C. Sun, S. Chen, and L. Hanzo. Structured non-uniformly spaced rectangular antenna array design for fd-mimo systems. *IEEE Trans. Wireless Commun.*, 16(5):3252–3266, May 2017.
- [Ma *et al.*, 2009] W. L. Ma, T. H. Hsieh, and C. Y. Chi. DOA estimation of quasi-stationary signals via Khatri-Rao subspace. In *Proc. Int. Conf. Acoust., Speech and Signal Processing (ICASSP)*, April 2009.
- [Mishali and Eldar, 2009] M. Mishali and Y. C. Eldar. Blind multiband signal reconstruction: compressed sensing for analog signals. *IEEE Trans. Sig. Proc.*, 57(3):993–1009, March 2009.
- [Mishali and Eldar, 2010] M. Mishali and Y. C. Eldar. From theory to practice: Sub-nyquist sampling of sparse wideband analog signals. *IEEE Journal of Selected topics in Signal Processing*, 4(2):375–391, April 2010.
- [Mitola and Maguire, 1999] J. Mitola and G. Q. Maguire. Cognitive radio: making software radios more personal. 6(4):13–18, 1999.
- [Nai *et al.*, 2010] Siew Eng Nai, Wee Ser, Zhu Liang Yu, and Huawei Chen. Beam-pattern synthesis for linear and planar arrays with antenna selection by convex optimization. *IEEE Transactions on Antennas and Propagation*, 58(12):3923–3930, 2010.
- [Nam *et al.*, 2013] Y. H. Nam, B. L. Ng, K. Sayana, Y. Li, J. Zhang, Y. Kim, and J. Lee. Full-dimension mimo (fd-mimo) for next generation cellular technology. *IEEE Communications Magazine*, 51(6):172–179, June 2013.
- [Narasimhan *et al.*, 2008] B. Narasimhan, Sili Lu, N. Al-Dhahir, and Hlaing Minn. Digital baseband compensation of I/Q imbalance in mobile OFDM. In *Proc. IEEE Int. Wireless Commun. & Networking Conf. (WCNC’08)*, pages 646–651, 2008.

BIBLIOGRAPHY

- [Neeser and Massey, 1993a] F. D. Neeser and J. L. Massey. Proper complex random processes with applications to information theory. *IEEE Trans. Inform. Theory*, 39(4):1293–1302, November 1993.
- [Neeser and Massey, 1993b] F. D. Neeser and J. L. Massey. Proper complex random processes with applications to information theory. *IEEE Trans. Inform. Theory*, 39(4):1293–1302, November 1993.
- [Negi and Cioffi, 2002] Rohit Negi and John M. Cioffi. Blind OFDM symbol synchronization in ISI channels. *IEEE Trans. Commun.*, 50(9):1525 – 1534, September 2002.
- [Pal and Vaidyanathan, 2010] P. Pal and P. P. Vaidyanathan. Nested arrays: a novel approach to array processing with enhanced degrees of freedom. *IEEE Trans. Sig. Proc.*, 58(8):4167–4181, August 2010.
- [Pal and Vaidyanathan, 2011] P. Pal and P. P. Vaidyanathan. Coprime sampling and the music algorithm. In *Proc. IEEE Digital Signal Processing and Signal Processing Education Workshop*, Arizona, AZ, January 2011.
- [Pal and Vaidyanathan, 2012] P. Pal and P.P. Vaidyanathan. Correlation-aware techniques for sparse support recovery. In *Proc. of IEEE Statistical Signal Processing (SSP) Workshop*, August 2012.
- [Popović, 1992] Branislav M. Popović. Generalized chirp-like polyphase sequences with optimum correlation properties. *IEEE Trans. Inform. Theory*, 38(4):1406–1409, July 1992.
- [Popović, 1994a] Branislav M. Popović. Efficient matched filter for the generalized chirp-like polyphase sequences. *IEEE Trans. Aerosp. Electron. Syst.*, 30(3):769–777, July 1994.

BIBLIOGRAPHY

- [Popović, 1994b] Branislav M. Popović. Gcl polyphase sequences with minimum alphabets. *IEEE Electronics Letters*, 30(2):106–107, January 1994.
- [Popović, 1998] Branislav M. Popović. Spreading waveforms for multi-carrier CDMA systems. *Spread Spectrum Techniques and Applications, 1998. Proceedings.*, 1:205–209, September 1998.
- [Press *et al.*, 1992] William H. Press, Saul A. Teukolsky, William T. Vetterling, and Brian P. Flannery. *Numerical Recipes in C: The Art of Scientific Computing*. Cambridge University, 1992.
- [Proakis, 1996a] J. G. Proakis. *Digital Signal Processing - Principles, Algorithms, and Applications*. Prentice Hall, 1996.
- [Proakis, 1996b] J. G. Proakis. *Digital Signal Processing - Principles, Algorithms, and Applications*. Prentice Hall, 1996.
- [Proakis, 1996c] J. G. Proakis. *Digital Signal Processing - Principles, Algorithms, and Applications*. Prentice Hall, 1996.
- [Rappaport *et al.*, 2013] T. S. Rappaport, S. Sun, R. Mayzus, H. Zhao, Y. Azar, K. Wang, G. N. Wong, J. K. Schulz, M. Samimi, and F. Gutierrez. Millimeter wave mobile communications for 5g cellular: It will work! *IEEE Access*, 1:335–349, 2013.
- [Rappaport *et al.*, 2014] T. S. Rappaport, R. W. Heath, R. C. Daniels, and J. N. Murdock. *Millimeter Wave Wireless Communication*. Prentice-Hall, 2014.
- [Sadler and Dandawate, 1997] B. M. Sadler and A. V. Dandawate. Nonparametric estimation of the cyclic cross spectrum. *IEEE Trans. Inform. Theory*, 44(1):351–358, January 1997.
- [Sahai and Cabric, 2005] A. Sahai and D. Cabric. A tutorial on spectrum sensing: fundamental limits and practical challenges. In *Proc. IEEE Symposium on*

BIBLIOGRAPHY

- New Frontiers in Dynamic Spectrum Access Networks (DySpan)*, Baltimore, MD, November 2005.
- [Samimi and Rappaport, 2016] M. K. Samimi and T. S. Rappaport. 3-d millimeter-wave statistical channel model for 5g wireless system design. *IEEE Transactions on Microwave Theory and Techniques*, 64(7):2207–2225, July 2016.
- [Sarate, 1979] D. V. Sarate. Bounds on crosscorrelation and autocorrelation of sequences. *IEEE Trans. Inform. Theory*, 25(6):720–724, November 1979.
- [Schuchert *et al.*, 2001] A. Schuchert, R. Hasholzner, and P. Antoine. A novel IQ imbalance compensation scheme for the reception of OFDM signals. *IEEE Trans. Consum. Electron.*, 47(3):313–318, August 2001.
- [Shah *et al.*, 2012] P. Shah, B. N. Bhaskar, G. Tang, and B. Recht. Linear system identification via atomic norm regularization. In *2012 IEEE 51st IEEE Conference on Decision and Control (CDC)*, pages 6265–6270, Dec 2012.
- [Shakeri *et al.*, 2012] S. Shakeri, D. D. Ariananda, and G. Leus. Direction of arrival estimation using sparse ruler array design. In *Proc. of The 13th IEEE International Workshop on Signal Processing*, Cesme, Turkey, 2012.
- [Sidiropoulos and Liu, 2001] N. D. Sidiropoulos and X. Liu. Identifiability results for blind beamforming in incoherent multipath with small delay spread. *IEEE Trans. Sig. Proc.*, 49(1):228–236, January 2001.
- [Steinwandt *et al.*, 2016] J. Steinwandt, F. Roemer, C. Steffens, M. Haardt, and M. Pesavento. Gridless super-resolution direction finding for strictly non-circular sources based on atomic norm minimization. In *2016 50th Asilomar Conference on Signals, Systems and Computers*, pages 1518–1522, Nov 2016.
- [Sturm, 1999] Jos F Sturm. Using sedumi 1.02, a matlab toolbox for optimization over symmetric cones. *Optimization methods and software*, 11(1-4):625–653, 1999.

BIBLIOGRAPHY

- [Sun and Rappaport, 2017] S. Sun and T. S. Rappaport. Millimeter wave mimo channel estimation based on adaptive compressed sensing. In *2017 IEEE International Conference on Communications Workshops (ICC Workshops)*, pages 47–53, May 2017.
- [Tan and Stüber, 2005] J. Tan and G. L Stüber. Multicarrier spread spectrum with constant envelope: Anti-jamming, jamming estimation, multi-user access. *IEEE Trans. Wireless Commun.*, 4(4):1527–1538, July 2005.
- [Tang *et al.*, 2013] G. Tang, B. N. Bhaskar, P. Shah, and B. Recht. Compressed sensing off the grid. *IEEE Trans. Inform. Theory*, 59(11):7465–7490, Nov 2013.
- [Tarighat *et al.*, 2005] A. Tarighat, R. Bagheri, and A. H. Sayed. Compensation schemes and performance analysis of I/Q imbalances in OFDM receivers. *IEEE Trans. Sig. Proc.*, 53(8):3257–3268, August 2005.
- [Tarokh and Jafarkhani, 2000] V. Tarokh and H. Jafarkhani. On the computation and reduction of the peak-to-average power ratio in multicarrier communications. *IEEE Trans. Commun.*, 48(1):37–44, January 2000.
- [Thomas *et al.*, 2014] T. A. Thomas, H. C. Nguyen, G. R. MacCartney, and T. S. Rappaport. 3d mmwave channel model proposal. In *2014 IEEE 80th Vehicular Technology Conference (VTC2014-Fall)*, pages 1–6, Sept 2014.
- [Thr, 2003] Ue radio transmission and reception, June 2003.
- [Thr, 2008] Evolved universal terrestrial radio access (e-utra); physical channels and modulation, March 2008.
- [Tian and Giannakis, 2007] Z. Tian and G. B. Giannakis. Compressed sensing for wideband cognitive radio. In *Proc. of the International Conference on Acoustics, Speech, and Signal Processing (ICASSP)*, April 2007.

BIBLIOGRAPHY

- [Tian *et al.*, 2017] Z. Tian, Z. Zhang, and Y. Wang. Low-complexity optimization for two-dimensional direction-of-arrival estimation via decoupled atomic norm minimization. In *2017 IEEE International Conference on Acoustics, Speech and Signal Processing (ICASSP)*, pages 3071–3075, March 2017.
- [Toh *et al.*, 1999] Kim-Chuan Toh, Michael J Todd, and Reha H Tutuncu. Sdpt3-a matlab software package for semidefinite programming, version 1.3. *Optimization methods and software*, 11(1-4):545–581, 1999.
- [Torkildson *et al.*, 2009] E. Torkildson, C. Sheldon, U. Madhow, and M. Rodwell. Nonuniform array design for robust millimeter-wave mimo links. In *GLOBECOM 2009 - 2009 IEEE Global Telecommunications Conference*, pages 1–7, Nov 2009.
- [Urkowitz, 1967] H. Urkowitz. Energy detection of unknown deterministic signals. *Proc. of the IEEE*, 55(4):523–531, 1967.
- [Valkama *et al.*, 2001] M. Valkama, Markku Renfors, and Visa Koivunen. Compensation of frequency-selective I/Q imbalances in wideband receivers: Models and algorithms. In *Proc. IEEE Int. Workshop on Signal Processing Advances for Wireless Commun. (SPAWC'01)*, pages 42–45, 2001.
- [Vaughan *et al.*, 1991] R. G. Vaughan, N. L. Scott, and P. R. White. The theory of bandpass sampling. *IEEE Trans. Sig. Proc.*, 39(9):1973–1984, September 1991.
- [Venkataramani and Bresler, 2000] Raman Venkataramani and Yoram Bresler. Perfect reconstruction formulas and bounds on aliasing error in sub-nyquist nonuniform sampling of multiband signals. *IEEE Trans. Inform. Theory*, 46(6):2173–2183, September 2000.
- [Verde, 2004] F. Verde. Subspace-based blind multiuser detection for quasi-synchronous MC-CDMA systems. *IEEE Signal Process. Lett.*, 11(7):621–624, July 2004.

BIBLIOGRAPHY

- [Verdu, 1998] S. Verdu. *Multiuser Detection*. Cambridge University Press, Cambridge, U.K., 1998.
- [Wang *et al.*, 2016] P. Wang, Y. Li, Y. Peng, S. C. Liew, and B. Vucetic. Non-uniform linear antenna array design and optimization for millimeter-wave communications. *IEEE Transactions on Wireless Communications*, 15(11):7343–7356, Nov 2016.
- [Wang, 2009] J. Wang. Beam codebook based beamforming protocol for multi-gbps millimeter-wave wpan systems. *IEEE Journal on Selected Areas in Communications*, 27(8):1390–1399, October 2009.
- [Welch, 1974] L. R. Welch. Lower bounds on the maximum cross correlation of signals. *IEEE Trans. Inform. Theory*, 20:397–399, May 1974.
- [Xing *et al.*, 2005] Guanbin Xing, Manyuan Shen, and Hui Liu. Frequency offset and I/Q imbalance compensation for direct-conversion receivers. *IEEE Trans. Wireless Commun.*, 4(2):673 – 680, March 2005.
- [Yang and Xie, 2016] Z. Yang and L. Xie. Exact joint sparse frequency recovery via optimization methods. *IEEE Trans. Sig. Proc.*, 64(19):5145–5157, Oct 2016.
- [Yang *et al.*, 2010] D. Yang, L. L. Yang, and L. Hanzo. Dft-based beamforming weight-vector codebook design for spatially correlated channels in the unitary precoding aided multiuser downlink. In *2010 IEEE International Conference on Communications*, pages 1–5, May 2010.
- [Yang *et al.*, 2016] Z. Yang, L. Xie, and P. Stoica. Vandermonde decomposition of multilevel toeplitz matrices with application to multidimensional super-resolution. *IEEE Trans. Inform. Theory*, 62(6):3685–3701, June 2016.
- [Yee *et al.*, 1993] N. Yee, J.P. Linnartz, and G. Fettweis. Multi-carrier cdma in indoor wireless radio networks. In *IEEE PIMRC*, pages 109–113, September 1993.

BIBLIOGRAPHY

- [Yucek and Arslan, 2009] T. Yucek and H. Arslan. A survey of spectrum sensing algorithms for cognitive radio applications. *IEEE Communications Surveys Tutorials*, 11(1):116–130, First 2009.
- [Zhang *et al.*, 2014] W. Zhang, W. Liu, J. Wang, and S. Wu. Joint transmission and reception diversity smoothing for direction finding of coherent targets in mimo radar. *IEEE Journal of Selected Topics in Signal Processing*, 8(1):115–124, Feb 2014.
- [Zhang *et al.*, 2015] P. Zhang, L. Gan, S. Sun, and C. Ling. Atomic norm denoising-based channel estimation for massive multiuser mimo systems. In *2015 IEEE International Conference on Communications (ICC)*, pages 4564–4569, June 2015.
- [Zhang *et al.*, 2017] Y. Zhang, G. Zhang, and X. Wang. Array covariance matrix-based atomic norm minimization for off-grid coherent direction-of-arrival estimation. In *2017 IEEE International Conference on Acoustics, Speech and Signal Processing (ICASSP)*, pages 3196–3200, March 2017.
- [Zheng and Wang, 2017] L. Zheng and X. Wang. Super-resolution delay-doppler estimation for ofdm passive radar. *IEEE Trans. Sig. Proc.*, 65(9):2197–2210, May 2017.